ADVERTIMENT. La consulta d'aquesta tesi queda condicionada a l'acceptació de les següents condicions d'ús: La difusió d'aquesta tesi per mitjà del servei TDX (www.tesisenxarxa.net) ha estat autoritzada pels titulars dels drets de propietat intel·lectual únicament per a usos privats emmarcats en activitats d'investigació i docència. No s'autoritza la seva reproducció amb finalitats de lucre ni la seva difusió i posada a disposició des d'un lloc aliè al servei TDX. No s'autoritza la presentació del seu contingut en una finestra o marc aliè a TDX (framing). Aquesta reserva de drets afecta tant al resum de presentació de la tesi com als seus continguts. En la utilització o cita de parts de la tesi és obligat indicar el nom de la persona autora.

ADVERTENCIA. La consulta de esta tesis queda condicionada a la aceptación de las siguientes condiciones de uso: La difusión de esta tesis por medio del servicio TDR (www.tesisenred.net) ha sido autorizada por los titulares de los derechos de propiedad intelectual únicamente para usos privados enmarcados en actividades de investigación y docencia. No se autoriza su reproducción con finalidades de lucro ni su difusión y puesta a disposición desde un sitio ajeno al servicio TDR. No se autoriza la presentación de su contenido en una ventana o marco ajeno a TDR (framing). Esta reserva de derechos afecta tanto al resumen de presentación de la tesis como a sus contenidos. En la utilización o cita de partes de la tesis es obligado indicar el nombre de la persona autora.

WARNING. On having consulted this thesis you're accepting the following use conditions: Spreading this thesis by the TDX (www.tesisenxarxa.net) service has been authorized by the titular of the intellectual property rights only for private uses placed in investigation and teaching activities. Reproduction with lucrative aims is not authorized neither its spreading and availability from a site foreign to the TDX service. Introducing its content in a window or frame foreign to the TDX service is not authorized (framing). This rights affect to the presentation summary of the thesis as well as to its contents. In the using or citation of parts of the thesis it's obliged to indicate the name of the author

TECHNICAL UNIVERSITY OF CATALONIA

Doctorate Program:
ADVANCED AUTOMATION AND ROBOTICS

PhD Thesis

SLIDING MODE CONTROL OF THE STAND ALONE WOUND ROTOR SYNCHRONOUS GENERATOR

Raúl Santiago Muñoz Aguilar

Advisers:
Enric Fossas Colet
Arnau Dòria Cerezo

Institute of Industrial and Control Engineering
May 26, 2010

To my family

Acknowledgments

Unas cuantas líneas es poco para agradecer la compañía, apoyo, formación y guía de tantas personas que me han ayudado a alcanzar esta meta.

Primero quiero dar gracias a Dios, Señor y dador de vida por todos los regalos y bendiciones recibidas. A mi familia por su formación, apoyo y preocupación en cada momento. A mi esposa por estar siempre a mi lado y soportar todas las restricciones que imponen la dedicación a una tesis; por la compañía y el apoyo en todo sentido.

Pasando al ámbito profesional, diversas personas han marcado mi vida y me han hecho enamorar de la ciencia. Inicialmente, en la Universidad Nacional de Colombia varios profesores me han mostrado la belleza de las máquinas eléctricas (Jorge Fernando Gutiérrez), la electrónica de potencia (Eduardo Antonio Cano) y el Control (Fabiola Angulo), gracias por mostrarme éste lindo camino, creer en mí y proyectarme hacia un futuro. Durante la Maestría, Fabiola me dió la oportunidad de hacer una estancia en España, en el grupo de investigación ACES, ahí conocí a Enric Fossas que me apoyó para seguir el doctorado y me ayudó a conseguir la beca. Gracias por la oportunidad.

Más adelante, Enric Fossas y Arnau Dòria me enseñaron la importancia de argumentar matemáticamente el comportamineto de los sistemas, el por qué se presentan diferentes fenómenos y el cómo analizarlo. Pero no solo eso, también cosas básicas como escribir adecuadamente, que no es nada fácil para un ingeniero. Además, me apoyaron en los momentos difíciles y se preocuparon por mi. Muchas gracias por todo, por soportarme, confiar en mí, darme esta oportunidad y valorar mi trabajo. Gracias por aceptar mis errores y corregirme.

En el IOC y en Barcelona han habido profesores, compañeros, amigos, personas que me han dado una palabra, un consejo, o simplemente la compañía en el momento oportuno. Son tantas que si las quisiera mencionar a todas seguro olvido a alguien. Así, que

solo mencionaré algunos, gracias a: Robert, Domingo, Rafel, Enric, Henry, Alex, Nacho, Guille,....

Quiero agradecer a Rafel Cardoner y Enric Miró por su gran ayuda en el montaje de la parte experimental de la tesis.

También quiero darle muchas gracias a Kasia, por su ayuda con las n correcciones del Inglés.

En el Departamento de Ingeniería Eléctrica me dieron la oportunidad de entrar como profesor ayudante y de pertenecer a SEER, en especial gracias a Pedro por dejarme pertenecer al grupo. A los consejos de Iñaki, y la compañia de Alvaro, Joan, Gerardo, Daniel y Juan Ramón.

I would like to express my gratitude to Prof. Vadim I. Utkin for its comments during the controller design and experimental steps.

Abstract

The control of the stand-alone the wound rotor synchronous generator has been analyzed in this dissertation. For this islanded configuration, the mechanical speed determines the frequency, and the rotor voltage is used to set the stator voltage amplitude. Due to the electrical time constant is so fast compared with the mechanical time constants, the mechanical speed was considered constant and externally regulated and the research was focused on the stator voltage amplitude regulation.

Four different controllers based on sliding mode control techniques were designed in the dq reference frame. The obtained control laws regulate the stator voltage amplitude irrespectively of the load value. Furthermore, only voltage and rotor position measures (to compute the dq transformation), are required. The stability of the obtained equilibrium points was proved at least using small-signal analysis.

Simulation and experimental validation of each controller containing several scenarios were carried out. The obtained results validate the designs and show the main advantages and disadvantages of each closed loop system.

Contents

List of Figures

List of Tables

Acronyms

AC: Alternating Current.
CSMC: Classical sliding mode based controller designed in Chapter 4.
DC: Direct Current.
DSMC: Direct sliding mode based controller designed in Chapter 5.
DSP: Digital signal processor.
ESMC: Extended system sliding mode based controller designed in Chapter 6.
HEV: Hybrid Electric Vehicle.
ICE: Internal Combustion Engine.
IM: (Squirrel Cage) Induction Machine.
ISD: Ideal Sliding Dynamics.
NSMC: Nested sliding mode based controller designed in Chapter 5.
PI: Proportional Integral controller.
PMSM: Permanent magnet synchronous machine.
SMC: Sliding Mode Control.
VSS: Variable Structure System.
WRSG: Wound Rotor Synchronous Generator.

Glossary of symbols

B: mechanical damping.

e: error.

F: amplitude of the sinusoidal waves.

$G(s)$: transfer function.

$\mathcal{I}_s$: amplitude of the stator currents.

i_s, i_F: stator and field currents, respectively.

i: current.

I_n: $n \times n$ identity matrix.

J: inertia of the rotating parts.

$\mathcal{L}(\theta), \hat{L}$: inductance matrix.

L: inductance.

$\mathcal{L}_s$, $\mathcal{L}_m$ and $\mathcal{L}_F$: stator, magnetization and field inductances, respectively.

L_s, L_F, L_m: stator, field and magnetization inductances, respectively.

L_L: inductive load.

n_p: number of pole pairs.

$O_{*\times*}$: zero matrix.

P: active power.

Q: reactive power.

R_L: resistive load.

R_s, R_F: stator and field resistances, respectively.

R: machine dissipative matrix.

$s(x)$: switching function or sliding surface.

u: fictitious control action.

u_{eq}: equivalent control.

$\mathcal{V}_s$: amplitude of the stator voltage.

v_s, v_F: stator and field voltage, respectively.
v: voltage.
δ_s: Stator selected rotating reference.
δ: arbitrary function of time
λ: flux.
λ_s, λ_F: stator and field flux.
$\mathbf{\Lambda}_s$: amplitude of the stator flux.
ω_m: mechanical speed.
ω: frequency of the sinusoidal waves or electrical speed..
ϕ_v: phase of the stator voltage respect to the rotor position.
ϕ_i: phase of the stator current respect to the rotor position.
ϕ_λ: phase of the stator flux respect to the rotor position.
τ: external torque provided to the machine.
τ_e: electromechanical torque generated by the machine.
θ: rotor position.

Subscripts

abc: phases a,b,c (natural reference frame).
α, β, γ: direct, quadrature and homopolar axes in the stationary reference frame.
$d, q, 0$: direct, quadrature and homopolar axes in the arbitrary reference frame.
s, F: stator and field, respectively.
W: WRSG

Mathematical Symbols

$\frac{\mathrm{d}}{\mathrm{d}t}$: differential operator.
∂: gradient of a function.
$\mathbb{R}$: Real Part.
$\tilde{(\cdot)}$: estimated values.

Chapter 1

Introduction

1.1 Motivation and antecedents

The electrical energy is widely studied around the world due to the advantages of transmission possibilities, flexibility and control capacity among others. Electrical energy is mainly generated interconnecting electric generators driven by prime-movers which are basically wind, hydro, steam turbines or internal combustion engines.

The standard power systems are composed mainly by Wound Rotor Synchronous Generators (WRSG) connected in parallel setting up a theoretical infinite bus. Hence, this kind of machine uses to be studied connected to an infinite bus called “power grid” [2], [7]. Thus, the own grid determines the stator voltage and frequency, while the rotor voltage helps to improve the power factor and to compensate the reactive power at the connection point. Usually, the stator transients can be neglected [39].

The power grid is stabilized by the rotational inertia of WRSG, but nowadays renewable energy generation is replacing the synchronous power generation capacity, decreasing the total rotational inertia in the system and causing frequency variations on the grid. This problem can be avoided using virtual inertias as a energy storage in the power converters. This is called a “Virtual Synchronous Generator” that contribute to the grid frequency stabilization [18], [30].

The synchronous machine is controlled by several techniques, in industry the most common are linear techniques [45], [70], [73], or hysteresis regulators [34]. However, decoupling methods [31], [9], which are widely employed for asynchronous machines, are also extended to the synchronous case. Modern control techniques such as passivity-based control [4], fuzzy control [42], or predictive control [60], [56] are also used for a WRSG regulation.

This machine can be employed in wind energy systems controlled by field oriented control [10] or classical PI controllers [27]. The synchronous machine can also be found in automotive applications [23], [68], controlled by rotor flux oriented control [74], Lyapunov-based designs [48], Robust LPV control [29] or sliding mode control [25]. In ship and aircraft applications, stator voltage regulation has been governed through model inversion principles [63] or H_∞ control [51], [50], [26].

The implementation of control algorithms for the synchronous machines using FPGA, DSP and PC-based controllers were studied using linear and nonlinear techniques as hysteresis control, P-PI control [58], torque control, [57], sliding mode control [59], [43], adaptive fuzzy control [41], predictive control among others [34], [60], [63].

The control of the machine connected to an infinite bus using H_∞ techniques [12], advanced linear control techniques [44], feedback linearization [3], passivity based control [62] and variable structure model reference adaptive control [22] were also studied.

A significantly different scenario is when the WRSG is isolated from the grid. This dissertation is focused in the stand-alone case of the wound rotor synchronous generator where neither the stator amplitude, nor frequency are fixed. For this insulated configuration, the mechanical speed determines the frequency, and the rotor voltage is used to set the stator amplitude. Normally, industry applications use linear controllers which cannot ensure stability. Additionally, in literature examples for the stand-alone case are not so extensive, the control of the synchronous generator supplying an active dc load was studied with classical controllers in [38].

Another difference in the analysis is that, in the grid-connected operation the stator transients of the machine can be neglected while in the stand-alone case it is not possible. Therefore, in the last case it is necessary to design a different controller depending of the load characteristics.

In this dissertation the WRSG is regulated in the Sliding Mode Control framework. This approach is particularly attractive for its robustness and easy implementation [33]. In general, sliding mode technique is appropriate for variable structure systems (VSS) as power converters [5], [79]. Even though electrical machines are not VSS, Sliding Mode Control has been suggested as appropriate for their control [75], [76] mainly because to the use of power converters when applying the electrical machine control voltages and the discrete values taken by control voltage. The sliding mode control techniques can also be used in the pulse width modulation design for the power converters control [79].

Sliding mode controllers combined with singular perturbation theory [69], [72], [71] and the block control approach [46], [7] has been proposed for a synchronous machine connected to the power grid. Other examples of sliding techniques can be found in multi-machine systems [32] and in motor applications as well [59] [43].

The main contribution of this dissertation is the design and implementation of sliding mode control algorithms for a stand alone wound rotor synchronous generator feeding isolated loads. In this Thesis two different scenarios are studied: a pure resistive load and an inductive load. The controllers we obtained are robust in front of machine and load parameter variations and they also provide a good performance and a fast response. The control laws (which only require voltage measurements and are easily implementable) are experimentally tested in a real plant. Local stability of the closed loop dynamics are proved using small-signal models.

1.2 Sliding mode control

In this Section a brief introduction to the Sliding Mode Control and Variable Structure Systems is presented. Firstly, a short historical background based on Utkin's review [77] is explained. Then, the math basis, equivalent control and stability analysis are shown.

The term “Variable Structure Systems” (VSS) was introduced by Emel'yanov in the sixties, although some previous works in the fifties had show the basic idea. The VSS study began with the analysis of second order linear and non-linear systems. Emel'yanov and his colleagues showed that the feedback gains could take several values depending on the system state. Each system consist of a set of linear structures supplied with a switching logic altering the structure of the resulting scheme with behavior not inherent in any of the structures [77].

The resulting state trajectories are oriented to the switching line (or surface) $s = h(x, \dot{x}) = 0$, called sliding surface. It means that the switching logic is in charge of approaching trajectories to the sliding surface and, when it is reached, trajectories remain on the sliding surface. This motion, called Sliding Mode, plays the dominant role in VSS [77].

Some characteristics of Sliding Mode Control are [77],

- the order of the motion equation is reduced,
- the dynamics in sliding mode is selected by the designer; in particular it can be linear,
- the parameters of the linear sliding dynamics are defined by the designer as well,
- the sliding modes are insensitive to the plant dynamics.

The ideal sliding dynamics exists while the system states satisfies $s = 0$ presumed infinitely fast switching. In actual plants the latter cannot be assumed and trajectories oscillates around the sliding surface. This oscillation is called “chattering” [11].

1.2.1 Mathematical remarks

The system under study is defined by,

$$\begin{aligned} \dot{x} &= f(x,t,u) \\ u &= \begin{cases} u^{+}(x,t) & \text{if} \quad s(x) > 0 \\ u^{-}(x,t) & \text{if} \quad s(x) < 0 \end{cases}, \end{aligned}$$

where f, u^{+}, u^{-} and s are continuous functions of their arguments and $u^{-}(x,t) \neq u^{+}(x,t)$. Since the control action is discontinuous, the closed loop system differential equation is discontinuous respect to the states, and the conventional theorems on existence and uniqueness of solutions are not applicable since Lipschitz constant does not exist for discontinuous vector fields [19].

Filippov proposed a solution for equations with discontinuous right hand sides which constructs a solution tangential to the sliding surface. A parallel approach developed by V. Utkin is called “Equivalent Control Method”. It makes $s = 0$ an invariant manifold [19]. Considering a linear system

$$\dot{x} = f(x,t) + g(x,t)u.$$

The equivalent control u_{eq} is such that the vector field $f + gu_{eq}$ is tangent to s. This results in

$$\frac{\partial s}{\partial x}\left(f + gu_{eq}\right) = 0,$$

hence

$$u_{eq} = -\left(\frac{\partial s}{\partial x} g\right)^{-1} \frac{\partial s}{\partial x} f. \tag{1.1}$$

The ideal sliding dynamics is obtained replacing the equivalent control in the system equation and assuming trajectories are in the sliding surface. That results in,

$$\begin{aligned} \dot{x} = f - g \left(\frac{\partial s}{\partial x} g\right)^{-1} \frac{\partial s}{\partial x} f, \\ s = 0. \end{aligned}$$

The stability of the switching surface can be shown using the second method of Lyapunov. Considering a Lyapunov function, $V(x,t)$, which is positive definite and has a negative time derivative in the region of attraction. This is known as the existence condition of the sliding modes [11].

A necessary and sufficient condition for the existence of control functions u^+ and u^- that makes s be a sliding surface is

$$< \nabla s, g > \neq 0,$$

which is known as the transversality condition. Otherwise, sliding mode exists on the submanifold of $s = 0$ defined by $\min\{u^-, u^+\} < u_{eq} < \max\{u^-, u^+\}$.

1.3 Thesis objectives

The main objectives of this dissertation are,

- To model the wound rotor synchronous generator feeding a resistive and an inductive load and the linear approximations of the whole systems.

- To design several controllers based on the sliding mode control approach for regulating the stator voltage amplitude of the stand-alone wound rotor synchronous generator feeding static and dynamic loads.

- To analyze the stability of the closed-loop systems obtained with the different designed controllers.

- To bear out the controllers behavior in a simulator platform and in an actual experimental plant containing several scenarios, with reference change and load variations evaluated for each controller.

1.4 Main contributions of the Thesis

The main contributions of this Thesis are summarized as follows,

- The WRSG has been analyzed in the stand-alone case where neither frequency nor stator voltage amplitude are fixed externally. Due to the mechanical speed is normally regulated by an external prime-mover, and the electrical time constant is so fast compared with the mechanical time constants, the mechanical speed is considered externally regulated and the research was focused on the stator voltage amplitude regulation. Normally, in the literature the main research results are pointed on the grid connected generation which simplifies the problem from the machine side due to its dynamical equations are reduced.

- Four different controllers based on sliding mode control techniques were designed in the dq reference frame. The obtained control laws regulate the stator voltage amplitude irrespectively of the load value. Furthermore, only voltage and rotor position measures (to compute the dq transformation), are required.

- The error of the square voltage amplitude ($V_{ref}^2 - V_s^2$) against the voltage amplitude difference discussed along the text shows the advantage of avoiding the root computation at the voltage calculus which is a hard task for digital control implementations and uses a lot of hardware resources. When a quadratic function is used as a switching function, an undesirable sliding motion may arise. A simpler alternative consists in a nested control with an inner SMC loop regulating the d-component of the stator voltage and a PI outer loop regulating its reference.

- This selection introduces the use of the d-voltage component sign in the control switching policy, which allows to stabilize the system in the two possible equilibrium points. This, cannot be achieved with a simple PI controller where one of the two equilibrium points becomes unstable.

- The implementation of the designed control schemes is quite simple, and some of them do not require any gain tunning.

- The stability of the closed-loop system were proved at least using a small-signal analysis. In some cases a local asymptotic stability was discussed.
- The problem of a zero relative degree output when dynamical loads are used was overcome introducing a dynamic extension of the system. This implies a fictitious control action which is integrated to obtain the real field voltage to be applied to the generator.
- Simulation and experimental validation of each controller was carried out. The obtained results validate the designs and show the main advantages and disadvantages of each one.

1.5 Publications

The publications related to the thesis are,

Conferences

1. A. Dòria-Cerezo, E. Fossas, R.S.Muñoz-Aguilar, and V.I. Utkin.
   Sliding mode control of an isolated wound rotor synchronous generator.
   In Proc. of the European Control Conference, Budapest, 2009.
2. A. Dòria-Cerezo, V.I. Utkin, R.S. Muñoz-Aguilar and E. Fossas.
   Two sliding mode control approaches of the stator voltage amplitude regulation of a stand-alone WRSG.
   In Proc. of the International Workshop on Variable Structure Systems, Mexico City, 2010.
3. R.S. Muñoz-Aguilar, A. Dòria-Cerezo and E. Fossas.
   A sliding mode control for a wound rotor synchronous generator with an isolated RL load.
   In Proc. of the American Control Conference, Baltimore, 2010.
4. A. Dòria-Cerezo, E. Fossas and R.S.Muñoz-Aguilar.
   Analysis of the closed loop dynamics of a sliding mode controlled stand alone synchronous generator.
   Submitted to Conference on Decision and Control, 2010.

Journals

1. R.S. Muñoz-Aguilar, A. Dòria-Cerezo, E. Fossas and R. Cardoner.
   Sliding mode control for a stand alone wound rotor synchronous generator.
   Submitted to IEEE Transactions on Industrial Electronics.

2. R.S. Muñoz-Aguilar, A. Dòria-Cerezo and E. Fossas.
   Stator voltage regulation of a stand-alone wound-rotor synchronous generator using sliding mode control techniques.
   Submitted to IEEE Transactions on Power Electronics.

3. A. Dòria-Cerezo, V.I. Utkin, R.S. Muñoz-Aguilar and E. Fossas.
   Control of a stand-alone wound rotor synchronous generator: sliding mode control via regulation the d-voltage component.
   Submitted to IEEE Transactions on Control Systems Technology.

4. E. Fossas, A. Dòria-Cerezo and R.S.Muñoz-Aguilar.
   Stability analysis of the closed loop dynamics of a sliding mode controlled stand-alone wound rotor synchronous generator.
   Submitted to International Journal of Control.

Book Chapters

1. E. Fossas, D. Biel, A. Dòria-Cerezo, R.S. Muñoz-Aguilar and R. Ramos-Lara.
   Two applications of Sliding Mode Control in Energy Generation and Power Electronics.
   Submitted to Lecture Notes in Control and Information Sciences.

Other publications not directly related with the thesis are,

- Raúl S. Muñoz-Aguilar, Arnau Dòria-Cerezo, and Paul F. Puleston.
  Energy-based modelling and simulation of a series hybrid electric vehicle propulsion system.
  In Proc. of the European Conference on Power Electronics and Application, Barcelona, 2009.

- D. Biel, E. Fossas, C. Meza and R.S Muñoz-Aguilar.
  Robust Exact Differentiation via Sliding Mode Technique applied to a Fixed-Frequency

Quasi-Sliding Control Algorithm.
Institute of Industrial and Control Engineering. Technical University of Catalonia.
Report. 2008

1.6 Thesis organization

Chapter 2 covers the modeling issues of the wound rotor synchronous machine. From the general three-phase dynamical equations, and using the Park transformation, the dq-model of the stand-alone wound rotor synchronous generator feeding both a resistive and an inductive load are obtained. Equilibrium points of the obtained systems are analyzed and, after defining the control objective, the desired equilibrium points are computed. Finally, linear approximated models are obtained and their transfer functions are also presented..

PI controllers are the most used in the industry because they offers good performance and are easily implementables. In Chapter 3 we obtain the tuning rule for the PI controller, and we analyze these results in order to propose new controllers which improve the classic PI approach.

The sliding mode control scheme for the WRSG connected to a resistive load is designed in Chapter 4. It also includes a complete stability analysis of the closed loop system. The main results of this Chapter are contained in [15], [55], [14], [13].

Chapter 5 presents two sliding mode designs to regulate the stator voltage amplitude for a stand alone wound rotor synchronous generator. Both use the stator voltage d-component error in the switching function. The first case is a nested controller, where an outer PI loop is added to provide the proper d-voltage component reference. In the second approach an integral term is added to the switching function. The main results of this chapter are contained in [17], [16].

The case of feeding an inductive load is studied in Chapter 6. The controller introduces a dynamic extension because the stator voltage amplitude is a zero relative degree output. As result, a robust controller, which neither depends on the machine parameters nor on the load values, is obtained. The main results of this Chapter are contained in [54], [53].

In Chapter 7 the simulation and the experimental results of the designed controllers for the stand-alone wound rotor synchronous generator are presented. Firstly, a complete description of the bench is provided. It also includes details of the data acquisition stage and the used DSP card. Secondly, the description of the simulation procedure is commented. Then, the simulation and experiments which contains several scenarios, with reference change and load variations evaluated for each controller are presented. The main results of this chapter are contained in [55], [16], [53].

Chapter 2

Modeling of a stand-alone wound rotor synchronous generator

Resume

In this Chapter the dynamical equations of the stand-alone wound rotor synchronous machine feeding both a resistive and an inductive load are obtained. From the well known three-phase equations, and by using the dq-transformation, the reduced system is interconnected to the load. Equilibrium points of the closed loop systems are computed. Finally, linear approximated models are obtained and their transfer functions are also presented.

2.1 Generalized model of an electrical machine

Electrical machines are highly non linear electromechanical systems. In general the electrical part is an n-phase system which depends on the rotor position, and its dynamics is given by the Kirchhoff laws [40],

$$v(t) = Ri(t) + \frac{\mathrm{d}\lambda(t)}{\mathrm{d}t}, \tag{2.1}$$

where $v(t) \in \mathbb{R}^n$, $i(t) \in \mathbb{R}^n$ and $\lambda(t) \in \mathbb{R}^n$ are the voltages, currents and fluxes; $R \in \mathbb{R}^{n\times n}$ is the machine dissipative matrix. Neglecting saturation effects, the fluxes, λ, are related to the currents, i, through the inductances matrix, $\mathcal{L}(\theta) \in \mathbb{R}^{n\times n}$,

$$\lambda = \mathcal{L}(\theta)i,$$

where θ is the rotor position. The inductance matrix form depends on the machine physical structure.

Mechanical dynamics is described by the Newton's second law,

$$J\frac{\mathrm{d}\omega_m}{\mathrm{d}t} = -B\omega_m + \tau_e + \tau, \tag{2.2}$$

where J is the rotor inertia, B is the damping coefficient, ω_m is the mechanical speed, τ is the external torque provided to the machine and τ_e is the electromechanical torque generated by the machine, which can be written as,

$$\tau_e = \frac{1}{2}i^T\frac{\partial\mathcal{L}(\theta)}{\partial\theta}i. \tag{2.3}$$

Along this Thesis the following assumptions are considered:

- Symmetrical phases with uniform air-gap and sinusoidally distributed phase windings.
- Infinite permeability of the fully laminated cores.
- Saturation iron losses, end winding and slot effects are neglected.
- Only linear magnetic materials are considered.
- The three-phase variables are balanced and equilibrated.

2.2 Three-phase model of a wound rotor synchronous machine

A three-phase wound rotor synchronous machine[1] is composed by a set of three-phase stator and a field windings feed with a DC voltage at the rotor side (Figure 2.1). In this Figure, and along the dissertation, convention of positive incoming current is adopted for both stator and field currents. In synchronous machines, the stator frequency, ω, is

---

[1] A cylindrical rotor type, without damping windings is considered.

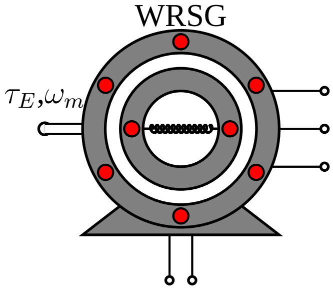

Figure 2.1: Three-phase synchronous machine scheme.

directly given by the mechanical speed, ω_m ($\omega_m = n_p\omega$, where n_p is the number of the pole pairs). At the stator side, the voltages, currents and fluxes are three-phase variables, while the rotor variables, indicated with the F subindex, are one dimensional [40].

$$\begin{aligned} v(t)^T &= \left(\begin{array}{c} v_{sa}, v_{sb}, v_{sc}, v_F \end{array} \right) = [v_s^T, v_F] \in \mathbb{R}^4, \\ i(t)^T &= \left(\begin{array}{c} i_{sa}, i_{sb}, i_{sc}, i_F \end{array} \right) = [i_s^T, i_F] \in \mathbb{R}^4, \\ \lambda(t)^T &= \left(\begin{array}{c} \lambda_{sa}, \lambda_{sb}, \lambda_{sc}, \lambda_F \end{array} \right) = [\lambda_s^T, \lambda_F] \in \mathbb{R}^4. \end{aligned}$$

Considering that the three-phase variables are balanced and equilibrated,

$$\begin{aligned} v_s(t)^T &= [v_{sa}, v_{sb}, v_{sc}] = \mathcal{V}_s \left(\cos(\theta+\phi_v), \cos\left(\theta+\phi_v-\frac{2\pi}{3}\right), \cos\left(\theta+\phi_v+\frac{2\pi}{3}\right) \right), \\ i_s(t)^T &= [i_{sa}, i_{sb}, i_{sc}] = \mathcal{I}_s \left(\cos(\theta+\phi_i), \cos\left(\theta+\phi_i-\frac{2\pi}{3}\right), \cos\left(\theta+\phi_i+\frac{2\pi}{3}\right) \right), \\ \lambda_s(t)^T &= [\lambda_{sa}, \lambda_{sb}, \lambda_{sc}] = \mathbf{\Lambda}_s \left(\cos(\theta+\phi_\lambda), \cos\left(\theta+\phi_\lambda-\frac{2\pi}{3}\right), \cos\left(\theta+\phi_\lambda+\frac{2\pi}{3}\right) \right), \end{aligned}$$

where $\mathcal{V}_s$, $\mathcal{I}_s$ and $\mathbf{\Lambda}_s$ are the amplitudes of the stator voltages, currents and fluxes, respectively, and ϕ_v, ϕ_i and ϕ_λ are their phases respect to the rotor position. The electric dissipation is represented by

$$R = \begin{pmatrix} R_s & 0 & 0 & 0 \\ 0 & R_s & 0 & 0 \\ 0 & 0 & R_s & 0 \\ 0 & 0 & 0 & R_F \end{pmatrix},$$

where R_s and R_F are the stator and field resistances, respectively. The inductance matrix, $\mathcal{L}(\theta)$, is defined as,

$$\mathcal{L}(\theta) = \begin{pmatrix} \mathcal{L}_s & \mathcal{L}_{ls} & \mathcal{L}_{ls} & \mathcal{L}_m \cos\theta \\ \mathcal{L}_{ls} & \mathcal{L}_s & \mathcal{L}_{ls} & \mathcal{L}_m \cos\left(\theta - \frac{2\pi}{3}\right) \\ \mathcal{L}_{ls} & \mathcal{L}_{ls} & \mathcal{L}_s & \mathcal{L}_m \cos\left(\theta + \frac{2\pi}{3}\right) \\ \mathcal{L}_m \cos\theta & \mathcal{L}_m \cos\left(\theta - \frac{2\pi}{3}\right) & \mathcal{L}_m \cos\left(\theta + \frac{2\pi}{3}\right) & L_F \end{pmatrix},$$

where $\mathcal{L}_s$, $\mathcal{L}_m$ and $\mathcal{L}_F$ are the stator, magnetization and field inductances, respectively.

Using the inductance matrix, the electrical torque (2.3) yields,

$$\tau_e = -\mathcal{L}_m i_F \left(i_a \sin\theta + i_b \sin\left(\theta - \frac{2\pi}{3}\right) + i_c \sin\left(\theta + \frac{2\pi}{3}\right)\right). \tag{2.4}$$

2.3 The dq-transformation

The dq-transformation, also known as a Park or Clare-Park transformation, allows to simplify the study of power systems [40] [78]. Under the standard assumptions listed previously, this transformation eliminates the θ-dependent coefficients of the inductance matrix and reduces the three-phase system into a two-phase system. This transformation is also used for control purposes to describe a tracking problem as a regulation one.

In this subsection, the dq-transformation is shortly presented. Let us define a three-phase variables vector as

$$f_{abc}^T = F\left(\cos(\omega t), \cos\left(\omega t - \frac{2\pi}{3}\right), \cos\left(\omega t + \frac{2\pi}{3}\right)\right),$$

where F is the amplitude of the sinusoidal waves and ω is its frequency.

The dq-transformation can be split in two parts. First, the three-phase system is transformed into the α, β, γ framework by means of

$$f_{\alpha\beta\gamma} = T f_{abc} \tag{2.5}$$

where

$$T = \begin{pmatrix} \frac{\sqrt{2}}{\sqrt{3}} & -\frac{1}{\sqrt{6}} & -\frac{1}{\sqrt{6}} \\ 0 & \frac{1}{\sqrt{2}} & -\frac{1}{\sqrt{2}} \\ \frac{1}{\sqrt{3}} & \frac{1}{\sqrt{3}} & \frac{1}{\sqrt{3}} \end{pmatrix}.$$

This transformation, for balanced systems, equals zero for the homopolar term (f_γ). This fact allows to reduce the original system to a two-phase one, $f_{\alpha\beta} = [f_\alpha, f_\beta]$.

The second part consists of a rotating reference framework, which in some cases reduces the sinusoidal functions into constants values. The new variables $f_{dq} = [f_d, f_q]^T \in \mathbb{R}^2$ are given by

$$f_{dq} = K^{-1} f_{\alpha\beta}, \tag{2.6}$$

where

$$K = e^{J\delta} = \begin{pmatrix} \cos(\delta) & -\sin(\delta) \\ \sin(\delta) & \cos(\delta) \end{pmatrix},$$

δ is an arbitrary function of time.

2.4 Model of a wound rotor synchronous machine in $\alpha\beta$-coordinates

Using the first part of the transformation presented in the previous Section, and assuming that the system is balanced, the dynamics of the wound rotor synchronous machine is reduced to only the $\alpha\beta$ coordinates in the stator part. Starting from the original system 2.1, the stator dynamics can be rewritten in $\alpha\beta\gamma$ coordinates, together with the rotor variable, as

$$v_{\alpha\beta\gamma F} = \frac{\mathrm{d}\lambda_{\alpha\beta\gamma F}}{\mathrm{d}t} + R_{\alpha\beta\gamma F} i_{\alpha\beta\gamma F},$$

where

$$R_{\alpha\beta\gamma F} = \mathcal{T} R \mathcal{T}^{-1} = R$$

and $\mathcal{T}$ contains the transformation introduced in 2.5

$$\mathcal{T} = \begin{pmatrix} T & O_{1\times 3} \\ O_{3\times 1} & 1 \end{pmatrix} \in \mathbb{R}^4.$$

Fluxes and currents are now related by

$$\lambda_{\alpha\beta\gamma F} = L_{\alpha\beta\gamma F} i_{\alpha\beta\gamma F},$$

where $L_{\alpha\beta\gamma F} = \mathcal{T}\mathcal{L}\mathcal{T}^{-1}$.

Assuming a three-phase equilibrated system ($f_a + f_b + f_c = 0$), the three-phase variables in the $\alpha\beta\gamma F$ coordinates yield,

$$v_{\alpha\beta\gamma F}^T = [v_\alpha, v_\beta, v_\gamma, v_F] = (V\cos(\theta + \phi_v), V\sin(\theta + \phi_v), 0, v_F)\,,$$

$$i_{\alpha\beta\gamma F}^T = [i_\alpha, i_\beta, i_\gamma, i_F] = (I\cos(\theta + \phi_i), I\sin(\theta + \phi_i), 0, i_F)\,,$$

$$\lambda_{\alpha\beta\gamma F}^T = [\lambda_\alpha, \lambda_\beta, \lambda_\gamma, \lambda_F] = (\Lambda\cos(\theta + \phi_\lambda), \Lambda\sin(\theta + \phi_\lambda), 0, \lambda_F)\,,$$

where $V = \frac{\sqrt{3}}{\sqrt{2}}\mathcal{V}$, $I = \frac{\sqrt{3}}{\sqrt{2}}\mathcal{I}$ and $\Lambda = \frac{\sqrt{3}}{\sqrt{2}}\mathbf{\Lambda}$. Note that the third component, γ, is zero and, under the equilibrated three-phase variables assumption, the electrical part of the system dimension is reduced and can be written as,

$$v_{\alpha\beta F} = \frac{\mathrm{d}\lambda_{\alpha\beta F}}{\mathrm{d}t} + R_{\alpha\beta F} i_{\alpha\beta F} \tag{2.7}$$

where fluxes and currents are related by

$$\lambda_{\alpha\beta F} = L_{\alpha\beta F} i_{\alpha\beta F}. \tag{2.8}$$

For the WRSG, the dissipation and inductance matrices in $\alpha\beta$-coordinates, are

$$R_{\alpha\beta F} = \begin{pmatrix} R_s & 0 & 0 \\ 0 & R_s & 0 \\ 0 & 0 & R_F \end{pmatrix},$$

$$L_{\alpha\beta F} = \begin{pmatrix} L_s & 0 & L_m\cos\theta \\ 0 & L_s & L_m\sin\theta \\ L_m\cos\theta & L_m\sin\theta & L_F \end{pmatrix}.$$

Finally, the electrical torque, τ_e, expressed in the $\alpha\beta$ coordinates,

$$\tau_e \;=\; L_m i_F (i_\alpha \sin\theta - i_\beta \cos\theta)\ .$$

2.5 The dq model

In this section the dq model of the wound rotor synchronous machine is presented. This model will be used in the next Chapters for control design. This is obtained rotating the $\alpha\beta$ reduced model by means of the transformation presented in (2.6). Then, the relationship between fluxes and currents can be rewritten by replacing (2.6) in (2.7) and (2.8)

$$v_{dq} = e^{-J\theta} R_{\alpha\beta} e^{J\theta} i_{dq} + e^{-J\theta} \frac{\mathrm{d}}{\mathrm{d}t} e^{J\theta} \lambda_{dq} + \frac{\mathrm{d}\lambda_{dq}}{\mathrm{d}t},$$

$$\lambda_{dq} = e^{-J\theta} L_{\alpha\beta} e^{J\theta} i_{dq} = L_{dq} i_{dq}.$$

Finally $\frac{\mathrm{d}\theta}{\mathrm{d}t} = \omega$,

$$e^{-J\theta} \frac{\mathrm{d}}{\mathrm{d}t}(e^{J\theta}) = e^{-J\theta}\omega \begin{pmatrix} -\sin\theta & -\cos\theta \\ \cos\theta & -\sin\theta \end{pmatrix} = \omega \begin{pmatrix} 0 & -1 \\ 1 & 0 \end{pmatrix} = \omega J_2,$$

and

$$e^{-J\theta} R_{\alpha\beta} e^{J\theta} = R_{\alpha\beta} = R_{dq}.$$

The dq-model is described by

$$v_{dq} = R_{dq} i_{dq} + J_\omega \lambda_{dq} + \dot{\lambda}_{dq}.$$

The mechanical dynamics also follows (2.2), and the electromechanical torque is derived from (2.3), and it depends on the topology of the electrical machine.

Notice that, assuming an equilibrated system, the three-phase variables are in the dq coordinates,

$$v_{dqF}^T = [v_d, v_q, v_F] = (V\cos\phi_v, V\sin\phi_v, v_F),$$

$$i_{dqF}^T = [i_d, i_q, i_F] = (I\cos\phi_i, I\sin\phi_i, i_F),$$

$$\lambda_{dqF}^T = [\lambda_d, \lambda_q, \lambda_F] = (\Lambda\cos\phi_\lambda, \Lambda\sin\phi_\lambda, \lambda_F).$$

For the WRSG, the L and J_ω matrices are,

$$L = \begin{pmatrix} L_s & 0 & L_m \\ 0 & L_s & 0 \\ L_m & 0 & L_F \end{pmatrix},$$

$$J_\omega = \begin{pmatrix} 0 & -\omega & 0 \\ \omega & 0 & 0 \\ 0 & 0 & 0 \end{pmatrix}.$$

Note that the inductance matrix, L does not depend on θ.

The mechanical dynamics is kept as in (2.4) where now the electrical torque is

$$\tau_e \;=\; -L_m i_F i_q.$$

2.6 Dynamical model of the WRSG with a resistive load

In this Section the dynamical model of the stand-alone WRSG interconnected with a resistive load is obtained. From the well-known dq-dynamical equations of the WRSG obtained in previous Section, and taking into account the physical interconnection rules with a pure resistor load, the dynamical equations of the whole system are found. The system, considering an externally regulated mechanical speed, becomes a linear system. However, the system output, i.e. the stator voltage amplitude, is a nonlinear function.

The equilibrium points of the system are obtained and the control objective is pointed out. The desired equilibrium points are computed replacing the equilibrium point of the system into the subspace defined by the control objective. The whole system dynamics, allows to determine the equilibrium points that can be parametrized in terms of the rotor voltage v_F, which will be used as a control input.

Also, the transfer function of the WRSG with resistive load is calculated. At the end of this Section, a linear approximation of the output function is computed and it is used to obtain a transfer function which relates v_F to V_s.

Figure 2.2 shows the proposed scenario: a primary mover drags, at a constant speed, a WRSG which acts as a generator to fed an isolated resistive load.

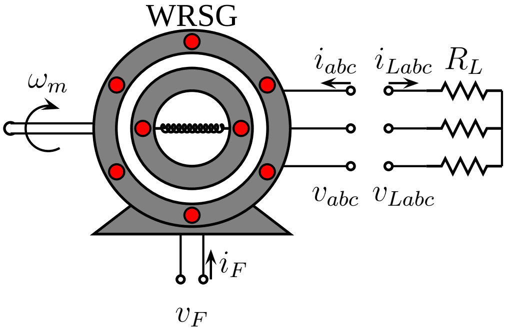

Figure 2.2: Scheme of a stand alone WRSG connection with a resistive load.

As explained in the previous Section, this system differs from the typical grid connection, where the frequency and the voltage amplitude are fixed by the electrical network. For a stand-alone connection the frequency is given by the mechanical speed, ω_m, (provided by a primary source, for instance an internal combustion engine), while the voltage amplitude must be assured by the rotor field voltage.

From the dq model obtained in Section 2.5, the electrical part of a wound rotor synchronous machine can be described using the state space form as

$$L\frac{\mathrm{d}x}{\mathrm{d}t} = \begin{pmatrix} -R_s & \omega L_s & 0 \\ -\omega L_s & -R_s & -\omega L_m \\ 0 & 0 & -R_F \end{pmatrix} x + \begin{pmatrix} v_d \\ v_q \\ v_F \end{pmatrix} \tag{2.9}$$

where $x^T = (i_d, i_q, i_F) \in \mathbb{R}^3$ are the dq-stator and field currents, respectively.

Let us obtain the complete model of a WRSG connected to a resistive load R_L. The interconnection scheme is depicted in Figure 2.2 where, $v_L^T = (v_{Ld}, v_{Lq}) \in \mathbb{R}^2$ and $i_L^T = (i_{Ld}, i_{Lq}) \in \mathbb{R}^2$ are the load voltages and currents in dq coordinates, which are related by

$$\begin{pmatrix} v_{Ld} \\ v_{Lq} \end{pmatrix} = R_L \begin{pmatrix} i_{Ld} \\ i_{Lq} \end{pmatrix}, \tag{2.10}$$

where R_L is the resistance value. The interconnection rules, according to Figure 2.2 are

$$\begin{aligned} v_s &= v_L \\ i_L &= -i_s \end{aligned}$$

where, $v_s^T = (v_d, v_q) \in \mathbb{R}^2$ and $i_s^T = (i_d, i_q) \in \mathbb{R}^2$, are the stator voltages and currents in the dq-framework. Now, putting together (2.9) and (2.10), the system can be written in an affine form as

$$L\frac{\mathrm{d}x}{\mathrm{d}t} = Ax + Bv_F, \tag{2.11}$$

where L is the inductance matrix defined before,

$$A = \begin{pmatrix} -(R_s+R_L) & \omega L_s & 0 \\ -\omega L_s & -(R_s+R_L) & -\omega L_m \\ 0 & 0 & -R_F \end{pmatrix},$$

and

$$B = \begin{pmatrix} 0 \\ 0 \\ 1 \end{pmatrix}.$$

2.6.1 Equilibrium points

The equilibrium points can be parametrized by the control input v_F, this results in

$$x^* = -A^{-1}Bv_F,$$

which yields a straight line defined by

$$x^{*T}(v_F) = \left(-\frac{\omega^2 L_s L_m}{R_F|Z_s|^2}, -\frac{\omega L_m(R_s+R_L)}{R_F|Z_s|^2}, \frac{1}{R_F}\right) v_F \tag{2.12}$$

where $|Z_s|^2 = \omega^2 L_s^2 + (R_s+R_L)^2$.

2.6.2 Control objective

As mentioned before, this machine must ensure stator voltage amplitude and frequency. For a synchronous generator, the stator frequency is directly given by the mechanical speed, which, in this dissertation is assumed to be constant and externally regulated. Then, the system output is the stator voltage amplitude V_s, which can be easily obtained, in a dq-framework as

$$V_s = \sqrt{v_d^2 + v_q^2}. \tag{2.13}$$

Last equation can be expressed in current terms using (2.10), which yields

$$V_s = R_L \sqrt{i_d^2 + i_q^2}, \tag{2.14}$$

and the control input is the field voltage v_F.

Note that, a fix value of V_s in (2.14), namely $V_s = V_{ref}$,

$$V_{ref}^{\ 2} = R_L^2 (i_d^2 + i_q^2), \tag{2.15}$$

defines a cylinder in the state space, x, see Figure 2.3.

Then, the desired equilibrium are in the intersection of the straight line (2.12) and the cylinder (2.15). Using cylindrical coordinates (I_s, δ, i_F)

$$\begin{aligned} i_d &= I_s \cos\delta \\ i_q &= I_s \sin\delta \end{aligned}$$

where, $I_s = \frac{V_s}{R_L}$, is easy to obtain

$$\begin{aligned} i_d^* &= \frac{V_{ref}}{R_L} \cos\delta^* && (2.16) \\ i_q^* &= \frac{V_{ref}}{R_L} \sin\delta^* && (2.17) \\ i_F^* &= -\frac{V_{ref}}{R_L} \frac{L_s}{L_m \cos\delta^*} && (2.18) \end{aligned}$$

where

$$\delta^* = \arctan\left(\frac{R_s + R_L}{\omega L_s}\right).$$

Note that the δ^* value[2] does not depend on the stator voltage amplitude. It only contains the load value and the stator parameters of the machine. In fact, two possible solutions exist, as it is shown in Figure 2.3 where the intersection of the cylinder defined by (2.15) and the equilibrium point distribution (2.12) is depicted.

---

[2] This δ^* angle, as the field magnetomotive force is in the q axis, can be seen as the load angle, which is largely studied for a grid connection to ensure remaining in synchronism. However, in this case of isolated generation with only one generator, the synchronism issue is not present.

Furthermore, the value of the field voltage in equilibria is

$$v_F^* = -\frac{R_F L_s}{R_L L_m \cos\delta^*} V_{ref}.$$

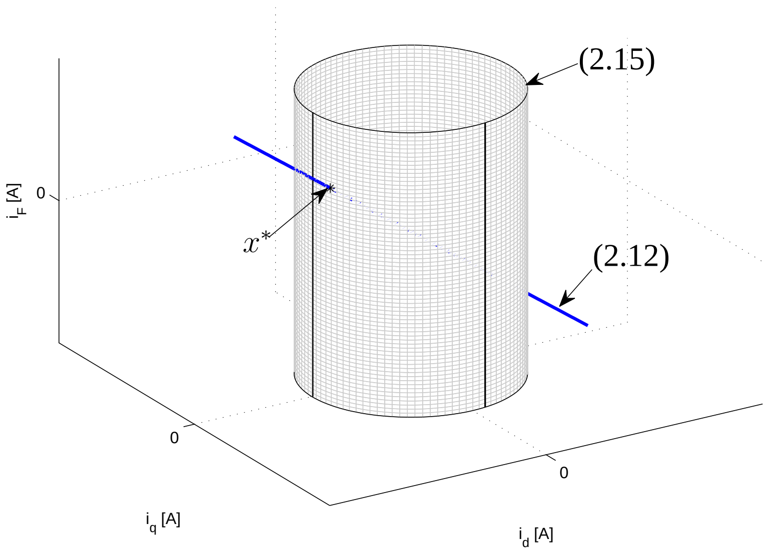

Figure 2.3: Intersection of the control goals and the equilibrium points distribution of the system.

2.6.3 Linear approximation

The system composed by the stand-alone WRSG and connected to resistive load is linear. A nonlinearity is introduced in the desired output, setting the amplitude of the stator voltage as a desired variable to be regulated. For a linear analysis and synthesis, the transfer function relating the control input (rotor voltage, v_F) to the desired output, the stator voltage amplitude, V_s is needed. From the linear state space description of each subsystem (2.11), a set of transfer functions which relate v_F to the currents, i_d, i_q and i_F can be computed. Namely,

$$G_i(s) = (sI_3 - L^{-1}A)^{-1}L^{-1}B$$

where I_3 is a 3×3 identity matrix, and $G_i(s)$ results in

$$G_d(s) = -\frac{a_2 s^2 + a_1 s + a_0}{d_3 s^3 + d_2 s^2 + d_1 s + d_0} \tag{2.19}$$

$$G_q(s) = -\frac{b_0}{d_3 s^3 + d_2 s^2 + d_1 s + d_0} \tag{2.20}$$

$$G_F(s) = \frac{c_2 s^2 + c_1 s + c_0}{d_3 s^3 + d_2 s^2 + d_1 s + d_0} \tag{2.21}$$

where $G_d(s) = \frac{I_d(s)}{V_F(s)}$, $G_q(s) = \frac{I_q(s)}{V_F(s)}$, $G_F(s) = \frac{I_F(s)}{V_F(s)}$, and

$$\begin{aligned}
a_2 &= L_m L_s \\
a_1 &= L_m(R_s + R_L) \\
a_0 &= \omega^2 L_m L_s \\
b_0 &= \omega L_m(R_s + R_L) \\
c_2 &= L_s^2 \\
c_1 &= 2L_s(R_s + R_L) \\
c_0 &= \omega^2 L_s^2 + (R_s + R_L)^2 \\
d_3 &= \mu L_s \\
d_2 &= (\mu + L_s L_F)(R_s + R_L) + L_s^2 R_F \\
d_1 &= \mu\omega^2 L_s + L_F(R_s + R_L)^2 + 2L_s(R_s + R_L)R_F \\
d_0 &= R_F(\omega^2 L_s^2 + (R_s + R_L)^2) \\
\mu &= = L_F L_s - L_m^2
\end{aligned}$$

Let us to consider, V_s as the output variable. Then, from (2.14), and linearizing around a desired point (i_d^*, i_q^*), which corresponds to V_s^*

$$V_s \simeq V_s^* + \frac{R_L i_d^*}{\sqrt{i_d^{*2} + i_q^{*2}}}(i_d - i_d^*) + \frac{R_L i_q^*}{\sqrt{i_d^{*2} + i_q^{*2}}}(i_q - i_q^*)$$

and using (2.14) around the operation point, $V_s^* = R_L\sqrt{i_d^{*2} + i_q^{*2}}$, yields

$$V_s \simeq \frac{R_L^2}{V_s^*}(i_d^* i_d + i_q^* i_q). \tag{2.22}$$

Replacing the dynamics of i_d and i_q (Equations (2.19) and(2.20)), in (2.22),

$$V_s(s) = -\frac{R_L^2}{V_s^*}\frac{i_d^*(a_2s^2 + a_1s + a_0) + i_q^*b_0}{d_3s^3 + d_2s^2 + d_1s + d_0}V_F(s) \tag{2.23}$$

Finally, taking into account (2.16) and (2.17), the transfer function $G(s) = \frac{V_s(s)}{V_F(s)}$ is

$$G(s) = R_L\frac{\cos\delta^*(a_2s^2 + a_1s + a_0) + \sin\delta^*b_0}{d_3s^3 + d_2s^2 + d_1s + d_0}.$$

where we used that we are only interested in the absolute value of the stator voltage amplitude. Note that, since

$$\delta^* = \arctan\left(\frac{R_s + R_L}{\omega L_s}\right).$$

(2.23) is approximated for any operation point, V_s^*.

2.7 Dynamical model of the WRSG with an inductive load

In this Section the dynamical model of the stand-alone WRSG connected to a inductive load is obtained. Using a similar procedure to the one presented in previous Section, the whole dynamical system is obtained. Also, the equilibrium points and the transfer function of the WRSG with inductive load are calculated.

Figure 2.4 shows the proposed scenario that is quite similar to the presented in the previous Section: a primary mover drags, with a constant speed, a WRSG which acts as a generator to feed an isolated inductive load. In the similar way that it was presented in the previous Section, the WRSG, is connected, in this case, to an inductive load.

Assuming that the mechanical speed is externally regulated by the primary mover, the electrical part of the wound rotor synchronous generator is the same described in the previous Section, represented by equation (2.9).

Let us obtain the complete model of a WRSG connected to an inductive load, which is modeled with a pure resistive element, R_L, in series with a pure inductive element, L_L. The interconnection scheme is depicted in Figure 2.4, where $v_L^T = (v_{Ld}, v_{Lq}) \in \mathbb{R}^2$ and

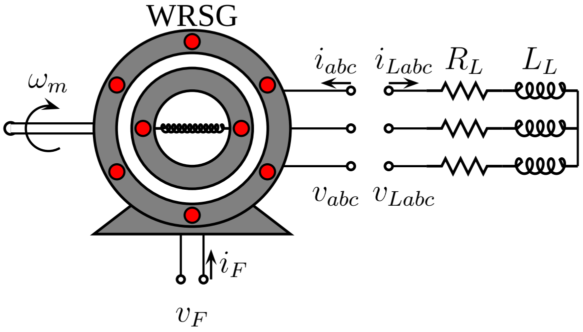

Figure 2.4: Scheme of a stand alone WRSG connection with an inductive load.

$i_L^T = (i_{Ld}, i_{Lq}) \in \mathbb{R}^2$ are the dq load voltages and currents, which are related by

$$v_L = (R_L I_2 + \omega L_L J_2) i_L + L_L \frac{\mathrm{d}}{\mathrm{d}t} i_L, \tag{2.24}$$

where

$$I_2 = \begin{pmatrix} 1 & 0 \\ 0 & 1 \end{pmatrix} \quad J_2 = \begin{pmatrix} 0 & -1 \\ 1 & 0 \end{pmatrix}.$$

According to Figure 2.4, the interconnection rules are the same that in the resistive case,

$$\begin{aligned} v_s &= v_L \\ i_L &= -i_s. \end{aligned} \tag{2.25}$$

Now, putting together (2.9), (2.24) and (2.25), the system can be written in an affine form as

$$\hat{L} \frac{\mathrm{d}x}{\mathrm{d}t} = \hat{A} x + B v_F, \tag{2.26}$$

where $\hat{L}$ is a new inductance matrix,

$$\hat{L} = \begin{pmatrix} L_s + L_L & 0 & L_m \\ 0 & L_s + L_L & 0 \\ L_m & 0 & L_F \end{pmatrix}$$

and the homogeneous dynamics $\hat{A}$ and the input vector B are given by

$$\hat{A} = \begin{pmatrix} -(R_s+R_L) & \omega(L_s+L_L) & 0 \\ -\omega(L_s+L_L) & -(R_s+R_L) & -\omega L_m \\ 0 & 0 & -R_F \end{pmatrix}$$

and

$$B = \begin{pmatrix} 0 \\ 0 \\ 1 \end{pmatrix},$$

respectively.

2.7.1 Equilibrium points

As proceeded for the load resistive case, the equilibrium points can be parametrized by the control input v_F, this resulting in

$$x^* = -\hat{A}^{-1} B v_F,$$

which again yields a straight line, in this case, defined by

$$x^{*T} = \left(-\frac{\omega^2 (L_s+L_L) L_m}{R_F |\hat{Z}_s|^2}, -\frac{\omega (R_s+R_L) L_m}{R_F |\hat{Z}_s|^2}, \frac{1}{R_F} \right) v_F \tag{2.27}$$

where $|\hat{Z}_s|^2 = \omega^2 (L_s+L_L)^2 + (R_s+R_L)^2$.

The desired equilibrium point is defined by $V_s = V_{ref}$.

2.7.2 Control objective

As mentioned before, the system output is the stator voltage amplitude, V_s, which in this case can be written as

$$V_s = \sqrt{v_d^2 + v_q^2}. \tag{2.28}$$

Using (2.24), in (2.28), the stator voltage amplitude yields

$$V_s^2 = \left(-R_L i_d + \omega L_L i_q - L_L \frac{\mathrm{d}i_d}{\mathrm{d}t} \right)^2 + \left(-R_L i_q - \omega L_L i_d - L_L \frac{\mathrm{d}i_q}{\mathrm{d}t} \right)^2 \tag{2.29}$$

where, from (2.26), the i_d and i_q current derivatives result in

$$\begin{aligned} \mu_d \frac{\mathrm{d}i_d}{\mathrm{d}t} &= L_F(-(R_s+R_L)i_d+\omega(L_s+L_L)i_q) - L_m(-R_F i_F + v_F) \quad (2.30)\\ \mu_q \frac{\mathrm{d}i_q}{\mathrm{d}t} &= -\omega(L_s+L_L)i_d - (R_s+R_L)i_q - \omega L_m i_F. \quad (2.31)\end{aligned}$$

where $\mu_d = L_F(L_s+L_L) - L_m^2$ and $\mu_q = L_s + L_L$.

Notice that, while the system dynamics is linear, as equation (2.26) indicates, V_s, is a tedious highly nonlinear function, which can be obtained replacing (2.30) and (2.31) in (2.29).

From (2.29), with (2.30) and (2.31), and taking into account that two solutions are possible, the value of v_F at the desired regulation point is

$$v_F^* = \pm \frac{|\hat{Z}_s|}{|Z_L|}\frac{R_F}{\omega L_m} V_{ref}, \quad (2.32)$$

where $|Z_L|^2 = \omega^2 L_L^2 + R_L^2$. Finally replacing $v_F = v_F^*$ from (2.32) in (2.27), i_d^*, i_q^* and i_F^* can be obtained.

At this point, as in the previous Section, using the cylindrical coordinates $i_d = I_s \cos\delta$, $i_q = I_s \sin\delta$, where now the stator current amplitude in steady state is $I_s^* = \frac{V_{ref}}{|Z_L|}$, it is easy to obtain

$$\begin{aligned} i_d^* &= \frac{V_{ref}}{|Z_L|}\cos\delta^* \quad (2.33)\\ i_q^* &= \frac{V_{ref}}{|Z_L|}\sin\delta^* \quad (2.34)\\ i_F^* &= -\frac{V_{ref}}{|Z_L|}\frac{L_s+L_L}{L_m\cos\delta^*} \quad (2.35)\end{aligned}$$

where

$$\delta^* = \arctan\left(\frac{R_s+R_L}{\omega(L_s+L_L)}\right).$$

Furthermore, the value of the field voltage in equilibria is

$$v_F^* = \pm\frac{R_F(L_s+L_L)}{|Z_L| L_m \cos\delta^*} V_{ref}.$$

2.7.3 Linear approximation

A transfer function, resulting from the linear approximation of the output, can also be obtained for the inductive load case. Using the standard procedure to obtain a set of transfer functions from a linear system

$$\hat{G}_i(s) = (sI_3 - \hat{L}^{-1}\hat{A})^{-1}\hat{L}^{-1}B$$

which results in a transfer function for each current i_d, i_q and i_F,

$$\hat{G}_d(s) = -\frac{\hat{a}_2 s^2 + \hat{a}_1 s + \hat{a}_0}{\hat{d}_3 s^3 + \hat{d}_2 s^2 + \hat{d}_1 s + \hat{d}_0} \tag{2.36}$$

$$\hat{G}_q(s) = -\frac{\hat{b}_0}{\hat{d}_3 s^3 + \hat{d}_2 s^2 + \hat{d}_1 s + \hat{d}_0} \tag{2.37}$$

$$\hat{G}_F(s) = \frac{\hat{c}_2 s^2 + \hat{c}_1 s + \hat{c}_0}{\hat{d}_3 s^3 + \hat{d}_2 s^2 + \hat{d}_1 s + \hat{d}_0} \tag{2.38}$$

where

$$\begin{aligned}
\hat{a}_2 &= L_m(L_s + L_L) \\
\hat{a}_1 &= L_m(R_s + R_L) \\
\hat{a}_0 &= \omega^2 L_m(L_s + L_L) \\
\hat{b}_0 &= \omega L_m(R_s + R_L) \\
\hat{c}_2 &= (L_s + L_L)^2 \\
\hat{c}_1 &= 2(L_s + L_L)(R_s + R_L) \\
\hat{c}_0 &= \omega^2(L_s + L_L)^2 + (R_s + R_L)^2 \\
\hat{d}_3 &= \mu_d(L_s + L_L) \\
\hat{d}_2 &= (\mu_d + (L_s + L_L)L_F)(R_s + R_L) + (L_s + L_L)^2 R_F \\
\hat{d}_1 &= \mu_d\omega^2(L_s + L_L) + L_F(R_L + R_s)^2 + 2(L_s + L_L)(R_s + R_L)R_F \\
\hat{d}_0 &= R_F(\omega^2(L_s + L_L)^2 + (R_s + R_L)^2)
\end{aligned}$$

Let us consider V_s as the output variable. From (2.29), and linearizing around a desired operating point V_s^*, V_s can be approximated by

$$V_s \simeq \frac{Z_L^2}{V_s^*}(i_d^* i_d + i_q^* i_q) \tag{2.39}$$

Replacing the dynamics of i_d and i_q (Equations (2.36) and(2.37)), in (2.39),

$$V_s(s) = -\frac{Z_L^2}{V_s^*}\frac{i_d^*(\hat{a}_2 s^2 + \hat{a}_1 s + \hat{a}_0) + i_q^* \hat{b}_0}{\hat{d}_3 s^3 + \hat{d}_2 s^2 + \hat{d}_1 s + \hat{d}_0} V_F(s).$$

Finally, taking into account (2.33) and (2.34), the transfer function $\hat{G}(s) = \frac{V_s(s)}{V_F(s)}$ results in

$$\hat{G}(s) = Z_L \frac{\cos\delta^*(\hat{a}_2 s^2 + \hat{a}_1 s + \hat{a}_0) + \sin\delta^* \hat{b}_0}{\hat{d}_3 s^3 + \hat{d}_2 s^2 + \hat{d}_1 s + \hat{d}_0}$$

where, as proceeded for the pure resistive case, only the absolute value of the amplitude is considered. Note that in the particular case, $L_L = 0$, the transfer function is the same as in the resistive load case.

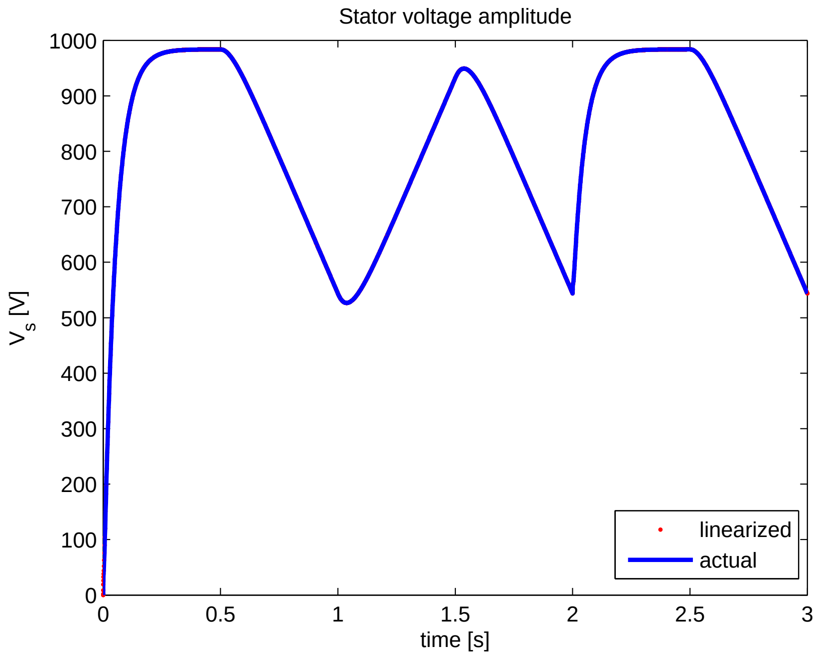

Figure 2.5: Stator voltage amplitude of the actual and the linearized model.

In order to validate the linearized model Figure 2.5 shows the stator voltage amplitude of the actual and linearized model using the parameters of the machine presented in Chapter 7 and the load values $R_L = 128\Omega$ and $L_L = 20$mH.

Chapter 3

Linear analysis of the stand-alone WRSG

Resume

PI controllers are the most used in the industry because they offer good performance and are easily implementables. In this chapter we obtain the tuning rule for the PI controller, and we analyze these results in order to propose new controllers which improve the classic PI approach.

3.1 Obtained linear model

The linear approximation of the stand alone wound rotor synchronous generator, presented in Section 2.7 shows that the resistive load case is a particular case of the resistive-inductive one, setting $L_L = 0$. In this Chapter, the general resistive-inductive load case will be analyzed. The transfer function that approximates the behavior of a stand-alone WRSG with an inductive load (see Chapter 2 for more details) is

$$\hat{G}(s) = Z_L \frac{\cos\delta^*(\hat{a}_2 s^2 + \hat{a}_1 s + \hat{a}_0) + \sin\delta^* \hat{b}_0}{\hat{d}_3 s^3 + \hat{d}_2 s^2 + \hat{d}_1 s + \hat{d}_0}$$

where,

$$\begin{aligned}
\hat{a}_2 &= L_m(L_s + L_L) \\
\hat{a}_1 &= L_m(R_s + R_L) \\
\hat{a}_0 &= \omega^2 L_m(L_s + L_L) \\
\hat{b}_0 &= \omega L_m(R_s + R_L) \\
\hat{d}_3 &= \mu_d(L_s + L_L) \\
\hat{d}_2 &= (\mu_d + (L_s + L_L)L_F)(R_s + R_L) + (L_s + L_L)^2 R_F \\
\hat{d}_1 &= \mu_d \omega^2 (L_s + L_L) + L_F(R_L + R_s)^2 + 2(L_s + L_L)(R_s + R_L)R_F \\
\hat{d}_0 &= R_F(\omega^2(L_s + L_L)^2 + (R_s + R_L)^2) \\
\mu_d &= L_F(L_s + L_L) - L_m^2 \\
\hat{Z}_L &= \sqrt{\omega^2 L_L^2 + R_L^2}
\end{aligned}$$

The stator voltage amplitude is defined as (2.13). This implies that there exist two possible equilibrium points. From a practical point of view, due to there is no constraint in the phase of the three phase stator voltages, both solutions satisfy the control goal. In the following, our choice corresponds to a positive gain for $\hat{G}(s)$ in order to obtain directly the amplitude value of V_s, as a positive value.

Figure 3.1 shows the bode plot of $\hat{G}(s)$. In this case, the load values are varying from $R_{L\text{min}} = 64\Omega$ to $R_{L\text{max}} = 10k\Omega$, and $L_{L\text{min}} = 0$H to $L_{L\text{max}} = 600$mH. The numerical computations obtained in this Chapter use the parameters of the machine presented in Chapter 7. In Figure 3.1 only the extreme cases are plotted. These diagrams do not necessarily correspond to the minimal/maximal values of the parameters, ***i.e.***, the bode diagrams for any considered load lie between these curves. Note that the cut-off frequency oscillates from 100 Hz to 400 Hz approximately, that means that for implementation purposes a switching frequency of two orders of magnitude the cut-off frequency is more than enough. This yields a switching frequency of 10kHz for the implementation purposes.

3.2 Stability analysis, K_p and K_i ranges

In this Section, the stability of the PI controller is presented. Figure 3.2 shows the proposed control scheme.

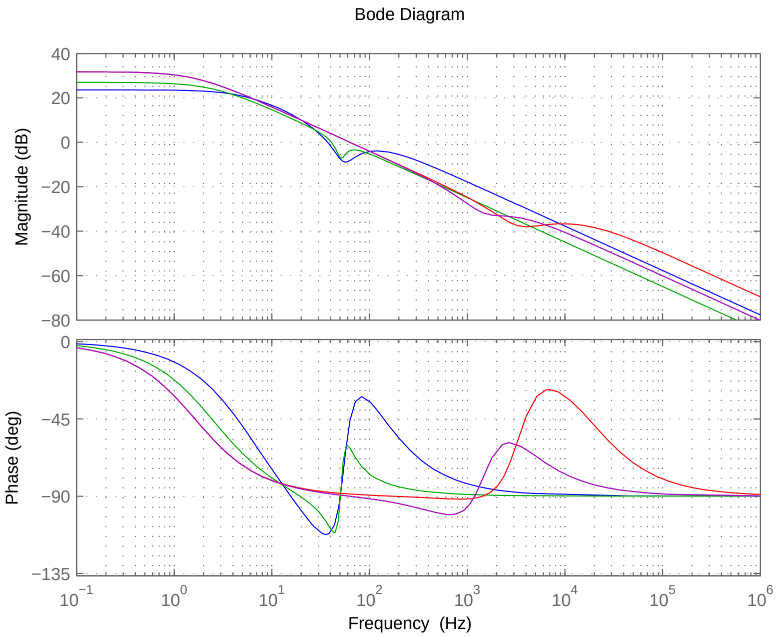

Figure 3.1: Bode diagram of the WRSG with resistive-inductive load.

The resulting open loop system transfer function adding a proportional-integral controller is

$$\widetilde{G}(s) = \frac{K_p s + K_i}{s} Z_L \frac{\cos\delta^*(\hat{a}_2 s^2 + \hat{a}_1 s + \hat{a}_0) + \sin\delta^* \hat{b}_0}{\hat{d}_3 s^3 + \hat{d}_2 s^2 + \hat{d}_1 s + \hat{d}_0}$$

which does not have poles in the right-half plane because $\hat{d}_i > 0 \; \forall i \in \{0, 1, 2, 3\}$ and $d_2 d_1 > d_3 d_0$. Then, using Nyquist stability criterion, the system is stable if there is not encirclement around point -1 [61]. Figures 3.3 and 3.4 shows the Nyquist diagram using a Proportional and a Proportional-Integral Control, respectively. Both figures, cut the negative real axis at the origin, then the system is stable for each K_p and K_i positive [1].

There are several well recognized phenomena in electrical drive systems that the control designer does not uses to account for. Among them are: parameter variations caused by winding temperature variation, switching effects and saturation. Additionally, the linear control methodology for inherent nonlinear high-order multivariable plants such as AC machines is insufficient. The use of pulse width modulation involves working with

---

[1] The singularity at $\omega = 0$ caused by the integral term has been considered when counting the index of the Nyquist curve around -1.

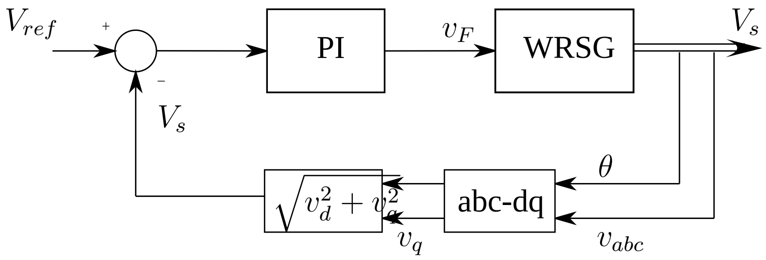

Figure 3.2: Proportional-Integral control scheme for a wound rotor synchronous generator.

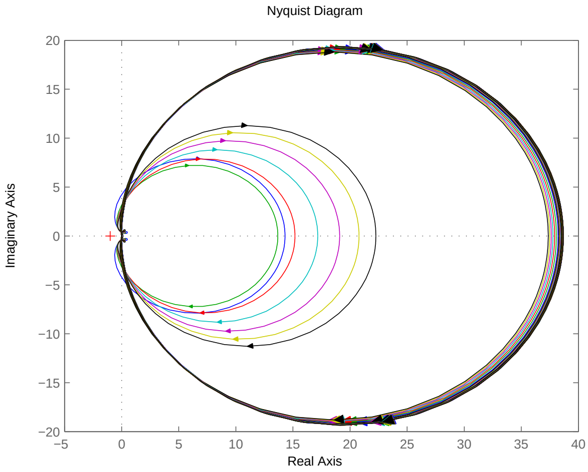

Figure 3.3: Nyquist diagram using a proportional controller.

averaged models that are smooth. It has been found interesting turning to algorithms with discontinuous control actions, more appropriated to power converters because of its own discontinuous nature. Actually, sliding mode control approach has taken a great interest of researchers because its features of order reduction, disturbance rejection, and strong robustness with a minimum of implementation complexity by means of power converters [75].

Moreover, using a PI controller one of the two equilibrium points becomes unstable, while the use of the d-voltage component sign in the control switching policy in sliding control mode will allow to stabilize the system at the two possible equilibrium points, as it will be shown in the next Chapters.

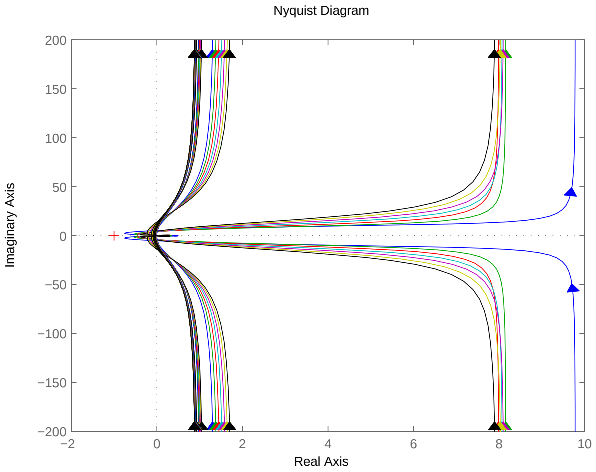

Figure 3.4: Nyquist diagram using a proportional-integral controller

---

3.3 Simulations

This Section shows the PI simulation results. The numerical experiment is done by varying the load resistance from $R_L = 120\Omega$ to $R_L = 64\Omega$ at $t = 0.05$s. The K_p and K_i values were calculated in order to guarantee the stability at the experiment and the V_{DC} value where saturated at $V_{DC} = 35V$.

Figure 3.5 shows the stator voltage amplitude regulation. Even if the R_L value is suddenly modified, the steady state value of the output is the desired one, and also the time convergence is small.

Figures 3.7 and 3.6 show the field voltage, v_F, which acts as a control action, and the error.

The dq stator voltages and the currents (the stator and the field ones) are displayed in Figures 3.8 and 3.9, respectively.

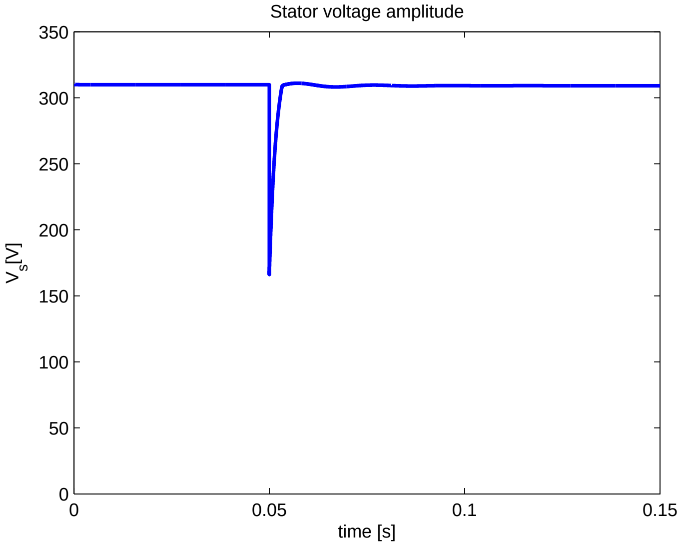

Figure 3.5: Simulation results, PI: Stator voltage amplitude.

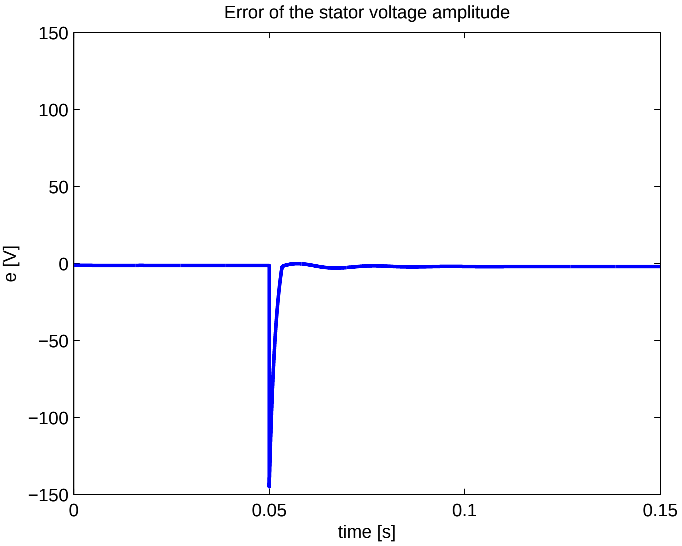

Figure 3.6: Simulation results, PI: Error of the stator voltage amplitude.

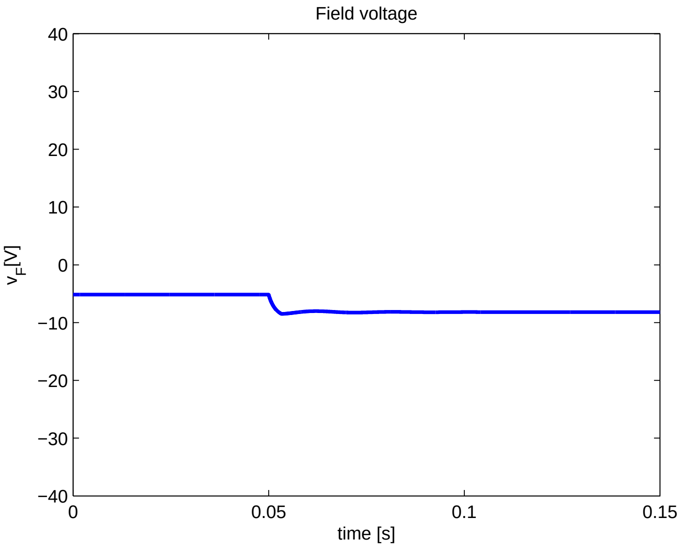

Figure 3.7: Simulation results, PI: Field voltage.

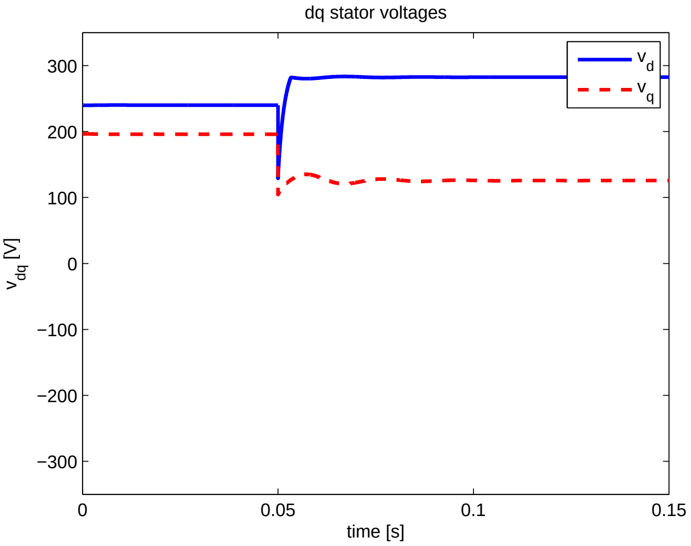

Figure 3.8: Simulation results, PI: dq stator voltages.

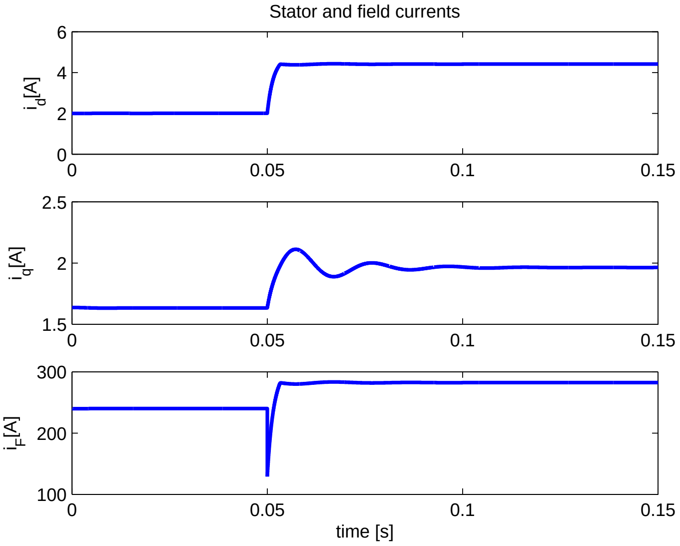

Figure 3.9: Simulation results, PI: Stator and field currents.

Chapter 4

Control of a stand-alone wound rotor synchronous generator with a resistive load

Resume

This chapter presents a sliding mode controller for a wound rotor synchronous machine acting as a generator for an isolated resistive load. A switching function is defined in order to fulfill control objectives, and the Ideal Sliding Dynamics is proved to be stable. From the desired surface, the standard sliding methodology is applied, and a robust controller is obtained. The presence of sliding modes in a second (and non-desired) surface motivates a deeper analysis of the ideal sliding and the full dynamics. Both are complex. Saturation effects in the actuator are also considered. Numerical simulations illustrate the complexity of the encountered behavior.

4.1 System description

Figure 4.1 shows the proposed scenario: a primary mover drags, at a constant speed, a WRSG which acts as a generator to fed an isolated load.

For an isolated configuration the frequency is determined by the mechanical speed, ω_m, (provided by the primary source), while the voltage amplitude must be assured by the

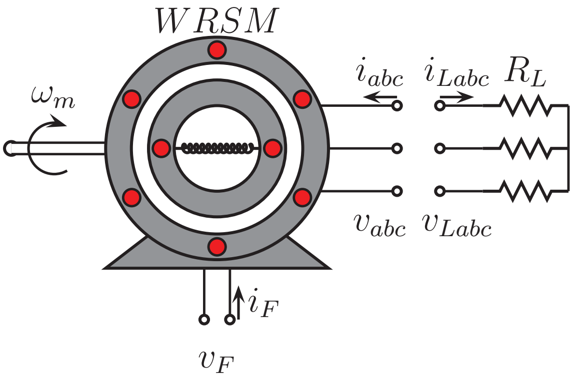

Figure 4.1: Scheme of a stand alone WRSG with resistive load.

---

rotor field voltage.

4.1.1 Dynamic model

The dynamic model of the the WRSG interconnected with a pure resistor load, was found in Section 2.6. The whole system dynamics can be written in an affine form as

$$L\frac{\mathrm{d}x}{\mathrm{d}t} = Ax + Bv_F, \tag{4.1}$$

where,

$$L = \begin{pmatrix} L_s & 0 & L_m \\ 0 & L_s & 0 \\ L_m & 0 & L_F \end{pmatrix},$$

$$A = \begin{pmatrix} -(R_s + R_L) & \omega L_s & 0 \\ -\omega L_s & -(R_s + R_L) & -\omega L_m \\ 0 & 0 & -R_F \end{pmatrix},$$

and

$$B = \begin{pmatrix} 0 \\ 0 \\ 1 \end{pmatrix}.$$

The load equation is,

$$\begin{pmatrix} v_{Ld} \\ v_{Lq} \end{pmatrix} = R_L \begin{pmatrix} i_{Ld} \\ i_{Lq} \end{pmatrix}. \tag{4.2}$$

4.2 Control design

In this Section the Sliding Mode Control technique is applied to regulate an isolated wound rotor synchronous generator. The switching surface is directly derived from the stator voltage amplitude and, assuming a bang-bang control action, the switching policy is defined in order to guarantee sliding modes. Then, the equivalent control is used to prove local stability of the Ideal Sliding Dynamics. Finally, the controller is obtained.

4.2.1 Switching function and equivalent control

According to the control goals we define switching function $s(x)$ as follows,

$$s(x) = V_s^2 - V_{ref}^2.$$

Note that the switching function contains the error of the square of the voltage amplitude, V_s^2, instead of the classical error difference. As it is shown below, this choice implies that both equilibrium points are achievable. Using (2.14) the switching function can be written in state variables as

$$s(x) = R_L^2(i_d^2 + i_q^2) - V_{ref}^2. \tag{4.3}$$

The equivalent control is defined so that $\dot{s} = 0$, (*i.e.* the fictitious control that makes the sliding surface flow invariant). Hence,

$$\frac{\partial s}{\partial x}\frac{\mathrm{d}x}{\mathrm{d}t} = 0.$$

Then, from (4.1)

$$\frac{\partial s}{\partial x} L^{-1}\left(Ax + Bu_{eq}\right) = 0,$$

now, solving for u_{eq} we obtain

$$u_{eq} = -\left(\frac{\partial s}{\partial x} L^{-1} B\right)^{-1} \frac{\partial s}{\partial x} L^{-1} A x. \tag{4.4}$$

Replacing the matrices and the switching function in (4.4) gets,

$$u_{eq} = R_F i_F - \frac{L_F}{L_m}(R_s + R_L) i_d + \omega L_m i_q - \frac{\mu}{L_s}\left(\frac{(R_s + R_L)}{L_m} i_q + \omega i_F\right)\frac{i_q}{i_d}, \quad (4.5)$$

where $\mu = L_s L_F - L_m^2$, which is always positive.

In the three dimensional space (i_d, i_q, i_F), the sliding surface is a cylinder. Sliding motion can be expected only in the cylinder subset defined by $i_d \neq 0$ where transversality condition holds. The closer to zero i_d, the higher the equivalent control; hence a closed subset of the sliding domain must be taken in order to get a bounded control effort u_{eq}.

4.2.2 Sliding mode controller

The Sliding Mode Controller must ensure trajectories go to the sliding surface and, when they reach the surface, it remain there. In this case, the desired sliding surface was defined in (2.14).

Consider the following Lyapunov function

$$V = \frac{1}{2} s^2, \quad (4.6)$$

it is positive. To stabilize the closed loop system, the derivative of (4.6) must be negative, $\dot{V} < 0$, which is equivalent to,

$$s \frac{\partial s}{\partial x} L^{-1}\left(Ax + Bv_F\right) < 0.$$

Adding and subtracting Bu_{eq} the latter equation yields

$$s \frac{\partial s}{\partial x} L^{-1}\left(Ax + Bv_F - Bu_{eq} + Bu_{eq}\right) < 0.$$

Now, taking into account (4.4),

$$s \frac{\partial s}{\partial x} L^{-1} B\left(v_F - u_{eq}\right) < 0. \quad (4.7)$$

Therefore, from (4.7), the control action defined by

$$v_F = u_{eq} - k \text{ sign}\left(s\frac{\partial s}{\partial x}L^{-1}B\right), \tag{4.8}$$

holds the stability condition , $|\dot{V} \leq 0$

$$\dot{V} = -k\left|s\frac{\partial s}{\partial x}L^{-1}B\right| \leq 0.$$

Evaluating $\left(s\frac{\partial s}{\partial x}L^{-1}B\right)$ in (4.8), the control law yields

$$v_F = u_{eq} - k \text{ sign}\left(-s\frac{2R_L^2L_m}{L_sL_F - L_m^2}i_d\right),$$

and taking into account that $\frac{2R_L^2L_m}{L_sL_F-L_m^2} > 0$ the sign term can be simplified to

$$-\,k \text{ sign}\left(-si_d\right). \tag{4.9}$$

4.2.3 Switching control policy

In this system, the control action v_F is implemented using a DC-DC power converter which commutes between two discrete signal values, $-V_{DC}$ and V_{DC}. Thus, the latter control law should be modified as follows.

From (4.9) the stability condition is simplified to

$$si_d(v_F - u_{eq}) < 0. \tag{4.10}$$

Since, the actual controller is a bang-bang actuator and taking into account equation (4.10), the control law defined by

$$v_F = \begin{cases} u^- & \text{if} \quad s\frac{\partial s}{\partial x}L^{-1}B > 0 \\ u^+ & \text{if} \quad s\frac{\partial s}{\partial x}L^{-1}B \leq 0 \end{cases},$$

assures $\dot{V} \leq 0$ presumed that $u^- < u_{eq} < u^+$.

Hence the field voltage

$$v_F = \begin{cases} V_{DC} & \text{if} \quad si_d < 0 \\ -V_{DC} & \text{if} \quad si_d > 0 \end{cases} \tag{4.11}$$

provides sliding modes in the subset of $s = 0$ defined by $-V_{DC} < u_{eq} < V_{DC}$.

For robustness purposes, since voltages are accessible variables and they are used to compute the switching function, the switching policy is given in voltage terms. Using (4.2) in (4.11) one gets,

$$v_F = \begin{cases} V_{DC} & \text{if} \quad sv_d < 0 \\ -V_{DC} & \text{if} \quad sv_d > 0 \end{cases} .$$

The proposed control scheme, that in the sequel we will refer as CSMC (Classical Sliding Mode Control), is depicted in Figure 4.2. θ is the rotor position (required to compute the dq-transformation) and v_{abc} is the three-phase stator voltages. An hysteresis block is added to limit the switching frequency. It is worth noticing that this control action depends on the voltages measurements and the rotor position only. Therefore, since the switching function, written as a function of the voltages, is parameter independent, the closed loop system is robust presumed that $-V_{DC} \leq u_{eq} \leq V_{DC}$.

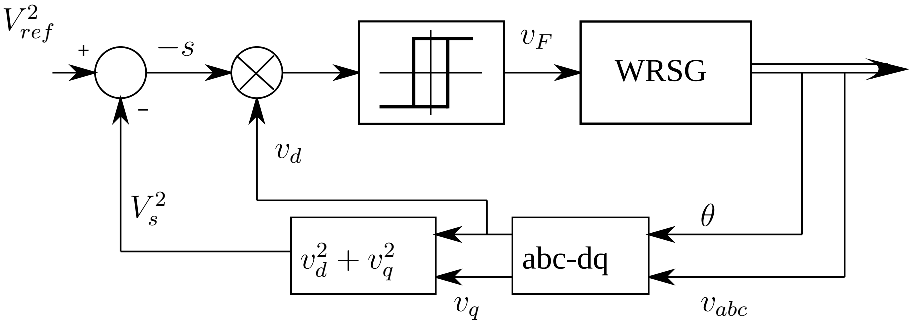

Figure 4.2: Control scheme implementation of a sliding mode controller for a stand-alone WRSG with a resistive load.

4.3 Analysis of the closed loop dynamics

This section deals with the closed loop dynamics for a sufficiently large value of V_{DC}, ***i.e.*** there are no constrains on the control action v_F. The ISD is analyzed and local stability of the equilibrium points is proved thanks to the Poincaré-Bendixon and Bendixon theorems. Additionally, the basin of attraction is computed. Then, we point out that, because of the use of a quadratic switching surface, the control algorithm designed in the previous Section involves two sliding surfaces: the cylinder defined by $s = 0$, and also the plane $i_d = 0$ for $s > 0$. This second surface implies that the system can slide on $s = 0$ and $i_d = 0$ alternatively.

The Ideal Sliding Dynamics (ISD), or zero dynamics, is the dynamics defined when sliding motion occurs ($s(x) = 0$) and, is given by the dynamical system (4.1) when the equivalent control, u_{eq}, (4.5) is used as control input. The ISD is given in local variables that parametrize the cylinder. Namely, i_q and i_F. Notice that this dynamics is well defined in the subset of $s(x) = 0$ where transversality condition holds.

Taking cylindrical coordinates in $\mathbb{R}^3$, (I, δ, i_F) where $i_d = I\,\cos\,\delta$, $i_q = I\,\sin\,\delta$, and replacing v_F by the equivalent control (4.5) in (4.1), the invariant dynamics on $s = 0$ results in

$$\begin{aligned}\frac{\mathrm{d}\delta}{\mathrm{d}t} &= -\frac{1}{\cos\delta}\left(\frac{\omega L_m R_L}{V_{ref} L_s} i_F + \frac{R_s + R_L}{L_s}\sin\delta\right) - \omega \\ \frac{\mathrm{d}i_F}{\mathrm{d}t} &= -\frac{1}{\cos\delta}\left(\omega i_F \sin\delta + \frac{R_s + R_L}{L_m R_L} V_{ref}\right).\end{aligned}$$

For ease reading, let us define the positive parameters $\hat{a} = \frac{\omega L_m R_L}{V_{ref} L_s}$, $\hat{b} = \frac{R_s + R_L}{L_s}$ and $\hat{c} = \frac{R_s + R_L}{L_m R_L} V_{ref}$. Then previous dynamics can be rewritten as

$$\cos\,\delta\frac{\mathrm{d}\delta}{\mathrm{d}t} = -\hat{a} i_F - \hat{b}\sin\,\delta - \omega\cos\,\delta \tag{4.12}$$

$$\cos\,\delta\frac{\mathrm{d}i_F}{\mathrm{d}t} = -\omega i_F \sin\,\delta - \hat{c}. \tag{4.13}$$

Remarks

- The dynamics is not defined in $\delta = \pm\frac{\pi}{2}$ (which corresponds to $i_d = 0$), where the transversally condition fails.

- There is a symmetry in the system. The sliding domain, ***i.e.*** the complementary of the planes $i_d = \pm\frac{\pi}{2}$ in the cylinder, has two connected components. The diffeomorphism $\phi(\delta, i_F) = (\delta + \pi, -i_F)$ transforms the dynamics on the subset of the cylinder defined by $\delta \in (-\frac{\pi}{2}, \frac{\pi}{2})$ into the dynamics on the subset of the cylinder defined by $\delta \in (\frac{\pi}{2}, \frac{3\pi}{2})$. Hence, from now on, only the dynamics on the subset of the sliding surface defined by $(-\frac{\pi}{2}, \frac{\pi}{2})$ will be analyzed.

Solving (4.13) for i_F, replacing the solution in (4.12) and using some algebra yields

$$\hat{b}\cos\delta^* - \omega\sin\delta^* = 0.$$

Thus,

$$\delta^* = \arctan\left(\frac{\hat{b}}{\omega}\right) = \arctan\left(\frac{R_s + R_L}{\omega L_s}\right) \tag{4.14}$$

which has a unique solution δ^* in $(-\frac{\pi}{2}, \frac{\pi}{2})$. Then, the field current equilibrium values are

$$i_F^* = -\frac{V_{ref}}{\omega L_m R_L}(\omega L_s\cos\delta^* + (R_s + R_L)\sin\delta^*), \tag{4.15}$$

The phase-portrait of the ISD on the cylinder is shown in Figure 4.3. The cylinder is obtained by identifying the straight lines of the border of the strip $-\frac{\pi}{2} < \delta < \frac{3\pi}{4}$. The sliding domain has two connected components, namely $-\frac{\pi}{2} < \delta < \frac{\pi}{2}$ and $\frac{\pi}{2} < \delta < \frac{3\pi}{4}$. The normalized vector field, two trajectories, each one reaching the corresponding equilibrium point and the basin of attraction of the dynamical system defined by (4.14) and (4.15) are depicted. Parameters used in numerical simulations are: $R_s = 3.06\Omega$, $L_s = 0.48$H, $L_m = 0.31$H, $R_F = 2.48\Omega$, $L_F = 0.24$H, $\omega = 2\pi 50\frac{\text{rad}}{\text{s}}$. The initial conditions of trajectory are $(\delta(0), i_F(0)) = (1\text{rad}, 5\text{A})$, and $(\delta(0), i_F(0)) = (4\text{rad}, -5\text{A})$. The equilibrium points coordinates are $(\delta^*, i_F^*) = (0.13\pi\text{rad}, -8.24\text{A})$ and $(\delta^*, i_F^*) = (1.13\pi\text{rad}, 8.24\text{A})$. Clearly, each initial condition reaches one of these stable, equilibrium points. Note that the symmetry already reported. Also, the vector field shows that there exist a subspace of the sliding domain where trajectories do not converge to the equilibrium points (these two areas are delimited by gray lines).

$$\begin{aligned} i_d\frac{\mathrm{d}i_d}{\mathrm{dt}} &= i_d\frac{1}{\mu}\left(-L_F(R_s + R_L)i_d + \omega L_s L_F i_q + L_m R_F i_F - L_m V_{DC}\text{sign}(i_d s)\right) < \\ &\leq i_d\frac{1}{\mu}L_m\left[\left|-\frac{L_F(R_s + R_L)}{L_m}i_d + \frac{\omega L_s L_F}{L_m}i_q + R_F i_F\right| - V_{DC}\right] < 0. \end{aligned} \tag{4.16}$$

$$\Omega_d = \left\{(i_d, i_q, i_F) \text{ s.t. } i_d^2 + i_q^2 > 0 \text{ and } \left|\frac{\omega L_s L_F}{L_m}i_q + R_F i_F\right| < V_{DC}\right\} \tag{4.17}$$

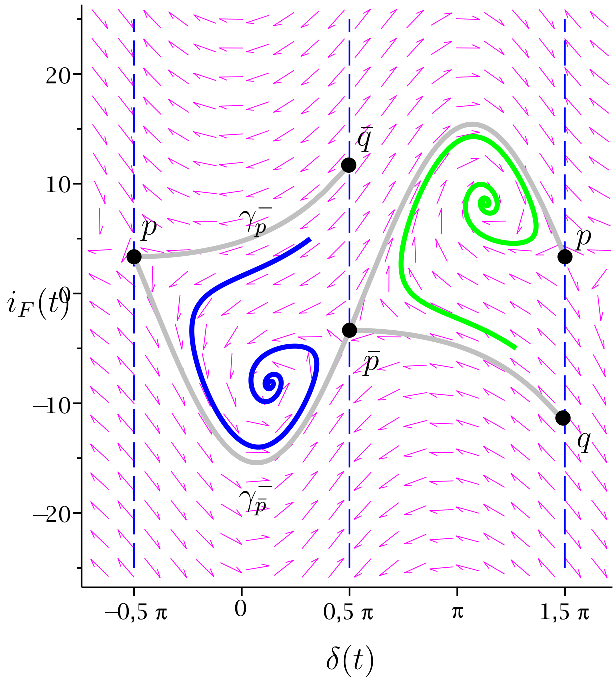

Figure 4.3: State space: vector field and two trajectories for a given initial conditions: $\delta(0) = 1\text{rad}, i_F(0) = 5\text{A}$, and $\delta(0) = 4\text{rad}, i_F(0) = -5\text{A}$.

Basin of attraction

Small signal analysis shows that the equilibrium points are locally stable. The basin of attraction is discussed in this subsection.

Let p and $\bar{p}$ the points on the cylinder defined in (δ, i_F) coordinates by

$$p = \left(\frac{-\pi}{2}, \frac{V_{ref}(R_s + R_L)}{\omega L_m R_L} \right)$$

and

$$\bar{p} = \left(\frac{\pi}{2}, -\frac{V_{ref}(R_s + R_L)}{\omega L_m R_L} \right),$$

which are also marked in Figure 4.3.

At these points, the right-hand side of equations (4.12)-(4.13) cancels. They will be key points in obtaining the basin of attraction. When δ converges to $\frac{-\pi}{2}$ from right (see Figure 4.3), the normalized ISD points towards the second quadrant above p while, below p, it points towards the fourth quadrant. Respectively, when δ converges to $\frac{\pi}{2}$ from left, the ISD points towards the third quadrant above $\bar{p}$ and to first quadrant below.

Let γ_p^- and $\gamma_{\bar{p}}^-$ the curves in the sliding domain defined in $\delta \in \left[-\frac{\pi}{2}, \frac{\pi}{2}\right]$ that reach p and $\bar{p}$ respectively. Simulation results show that $\gamma_{\bar{p}}^-$ starts at p.

Finally, let Ω_s be the subset of the sliding domain limited by γ_p^-, $\gamma_{\bar{p}}^-$ and $\delta = \frac{\pi}{2}$, Ω_s is an invariant set with respect to the ideal sliding dynamics. Moreover,

$$\cos(\delta) \cdot \left(\frac{\mathrm{d}\delta}{\mathrm{d}t}, \frac{\mathrm{d}i_F}{\mathrm{d}t}\right) \neq 0$$

in the interior of the sliding domain limited by γ_p^-, $\gamma_{\bar{p}}^-$ and $\delta = \frac{\pi}{2}$. Hence, using Dulac's criterium [64] it can be stated that there are no periodic orbits in Ω_s. Finally, the Poincaré-Bendixon theorem proves that this domain is the basin of attraction of the equilibrium point.

Remarks

- Let γ_ϕ be the trajectory in the $(\frac{\pi}{2}, \frac{3\pi}{2})$ domain given by $\phi \cdot \gamma_{\bar{p}}^-$, where ϕ is the diffeomorphism defined in section 4.3. Note that trajectory $\gamma_{\bar{p}}^-$, which starts at p, finish at $\bar{p}$, where trajectory γ_ϕ starts. The path obtained joining both trajectories seems to be a limit cycle, but it is broken at $\delta = \pm\frac{\pi}{2}$ because the transversality condition does not hold at it.

- This behavior in not possible in a real application due to the physical $V_{DC}-$limit, as it will be shown in the next Section.

- Unfortunately, due to the nonlinearity of the dynamical system, it is not possible to get analytical expressions of γ_p^- and $\gamma_{\bar{p}}^-$.

4.3.1 Dynamics on $i_d = 0$

In this subsection it is shown that, although the control law is designed to slide on $s = 0$, the switching control law defined in (4.11) gives rise to two discontinuity surfaces: $s = 0$ and $i_d = 0$.

To answer whether $i_d = 0$ is a sliding surface, let us check the reachability condition.

The calculation of $i_d \frac{\mathrm{d}i_d}{\mathrm{dt}}$ yields

$$\begin{aligned} i_d \frac{\mathrm{d}i_d}{\mathrm{dt}} &= i_d \frac{1}{\mu} \left(-L_F(R_s + R_L) i_d + \omega L_s L_F i_q \right) \\ &\quad + i_d \frac{1}{\mu} \left(L_m R_F i_F - L_m V_{DC} \mathrm{sign}(i_d s) \right). \end{aligned} \tag{4.18}$$

Let us first consider the outer of the cylinder, ***i.e.*** $\{i_d = 0\} \cap \{s > 0\}$. In the subset defined by

$$\left| -\frac{L_F(R_s + R_L)}{L_m} i_d + \frac{\omega L_s L_F}{L_m} i_q + R_F i_F \right| < V_{DC}, \tag{4.19}$$

the right-hand side of equation (4.18) is negative, as equation (4.16) shows.

Following the same argument, it can be found a repulsive subset of $\{i_d = 0\} \cap \{s < 0\}$. Hence, there are sliding motions on the subset Ω_d of $i_d = 0$ defined by (4.17), see Figure 4.4.

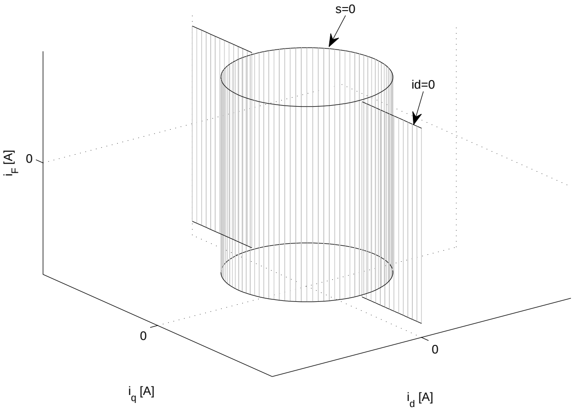

Figure 4.4: Sliding surfaces, $s = 0$ and $i_d = 0$, defined by the designed control law.

Finally, computing the equivalent control and replacing it on (4.1), the ISD on $i_d = 0$ is obtained. It results in the linear dynamics

$$\begin{aligned} L_s \frac{\mathrm{d}i_q}{\mathrm{d}t} &= -(R_s + R_L) i_q - \omega L_m i_F \\ L_m \frac{\mathrm{d}i_F}{\mathrm{d}t} &= \omega L_s i_q. \end{aligned}$$

which has a stable, virtual[1] equilibrium point at $(0,0,0)$. This implies that, if the sliding condition on $i_d = 0$, see (4.19), holds, ISD-trajectories go to the equilibrium point which lies inside the cylinder but they start sliding on the cylinder when they try to cross it. Actually, trajectories can switch between both sliding surfaces, as the numerical example in Figure 4.5 shows. Initial conditions are selected so that the corresponding trajectory goes to the cylinder, reaching it out of the attraction area defined in Subsection 4.3, (in the figure depicted with a red line). The trajectory goes on to the intersection of $s = 0$ and $i_d = 0$ and starts to slide on $i_d = 0$. This behavior is repeated closer and closer to the cylinder till it reaches the cylinder inside one of the basins of attractions. Then, it converges to the corresponding equilibrium point.

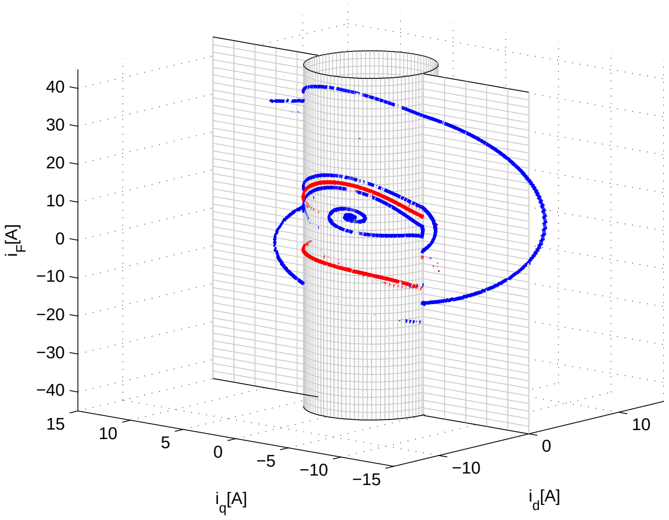

Figure 4.5: Sliding surfaces, $s = 0$ and $i_d = 0$, and one possible trajectory.

A picture of V_s and the states variables (i_d, i_q, i_F) as functions of time is shown in Figure 4.6. Note that V_s reaches the reference value and i_d is zero in alternative time periods (first and second sub-figures) till $t = 0.08$s. Then it remains on $V_s = V_{ref}$. Nevertheless, the required V_{DC} values to slide on $i_d = 0$ in an actual plant are over the applicable range. For instance, the required V_{DC} voltage to slide on $i_d = 0$ would be higher than 10^4V for the real WRSG used in the simulations of the previous Section, while the maximum value it can take is 35V.

---

[1] The equilibrium point is called virtual because it does not belong to the sliding domain.

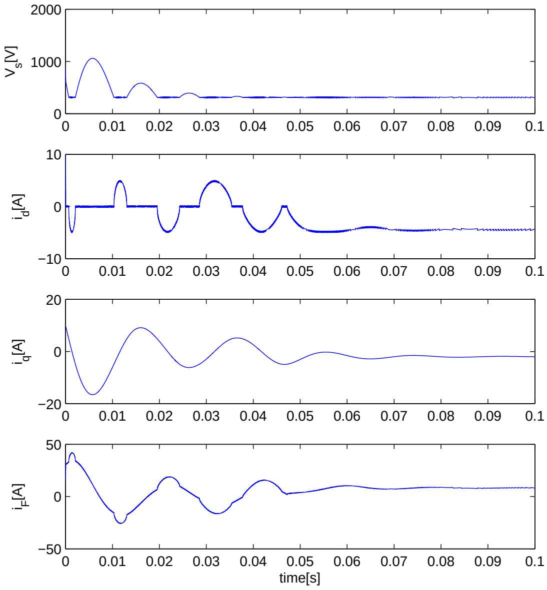

Figure 4.6: Simulation results taking a V_{DC} sufficiently large.

4.4 Analysis of an actual plant dynamics

In a real application, the V_{DC} values are restricted by a voltage source, the voltage grid, or the nominal values of the power converter. Usually electrical engineers take the V_{DC} value depending on the WRSG specifications and requirements.

The main consequence of saturated V_{DC} values is that the sliding condition is fulfilled in a strict subset of the switching surface $s(x) = 0$, actually a small subset.

When the control output values are in the set $\{-V_{DC}, V_{DC}\}$ $(V_{DC} > 0)$, the sliding domain is the strict subset of $s(x) = 0$ defined by

$$\left| \frac{\mu}{2L_m R_L^2} \frac{1}{i_d} \left(\frac{\partial s}{\partial x} L^{-1} A x \right) \right| < V_{DC}. \tag{4.20}$$

In this Section we numerically analyze the influence of saturation in the V_{DC} values. All computations and simulations are done using the same WRSG parameters of the previous Section.

Figures 4.7 and 4.8 show the sliding domains in the (δ, i_F) and 3D representation of the cylinder for a WRSG and two different values of V_{DC}. Note that the higher the V_{DC} value, the wider the sliding domain.

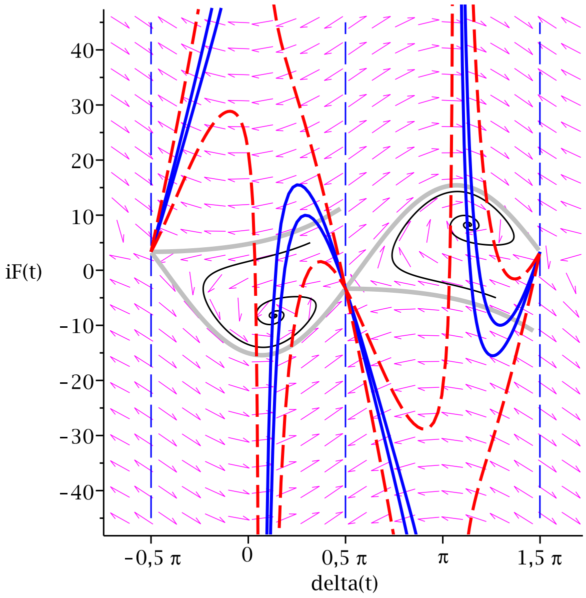

Figure 4.7: Sliding zones for $V_{DC} = 35$V (blue line) and $V_{DC} = 350$V (red dotted line).

Figure 4.9 shows, in a 3D plot, a trajectory simulated using a small V_{DC}-value. Control parameters are set to $V_{ref} = 220\sqrt{2}$V, $V_{DC} = 35$V, and initial conditions are $i_d(0) = -8$A, $i_q(0) = 7$A and $i_F(0) = 5$A. The sliding domain on the cylinder is also drawn, note how narrow it is.

Stator voltage amplitude, V_s, and the switching function $s(x)$ are displayed in Figure 4.10. State variables are depicted in Figure 4.11. In general, there is no sliding on $i_d = 0$ in a real case. This is due to the fact that condition (4.19) fails for WRSG realistic parameters and small V_{DC} values.

As previous simulations show, trajectories can lose the sliding surface. The question is how to prove that they finally will reach the desired equilibrium point. To obtain an analytical result became an impossible task. In order to verify that for any (reasonable) initial condition the system achieves the desired regulation value, a set of simulations are done in a box defined by the maximum values of the state variables (corresponding to the maximal admissible currents to the WRSG). Figures from 4.12 to 4.14, show trajectories

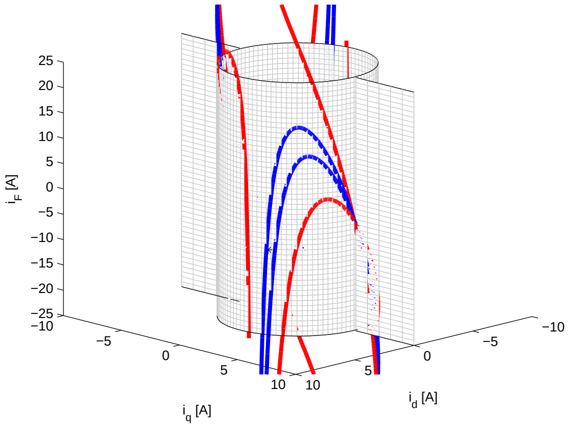

Figure 4.8: Sliding zones for $V_{DC} = 35$V (blue line) and $V_{DC} = 350$V (red line), on the cylinder $s = 0$.

---

for initial conditions in the range $i_d, i_q \in (-8\text{A}, 8\text{A})$ and $i_F \in (-20\text{A}, 20\text{A})$, which are twice their nominal values. For all initial conditions, the system reaches the desired equilibrium point.

4.5 Simulations

The CSMC simulation results are depicted in this Section. In order to implement the discrete time controller we add an hysteresis block at the (4.2.3) condition. The numerical experiment is done by varying the load resistance from $R_L = 120\Omega$ to $R_L = 64\Omega$ at $t = 0.05$s.

Figure 4.15 shows that the stator voltage amplitude is regulated. Even if the R_L value is suddenly modified, the steady state value of the output is the desired one, and also the time convergence is short.

Figures 4.17 and 4.16 show the field voltage, v_F, which acts as a control action, and the switching function, s, defined in (4.3). Note that v_F commutes between $\pm V_{DC}$, and that the the switching function oscillates around zero.

The dq stator voltages and the currents (the stator and field ones) are displayed in Figures 4.18 and 4.19, respectively.

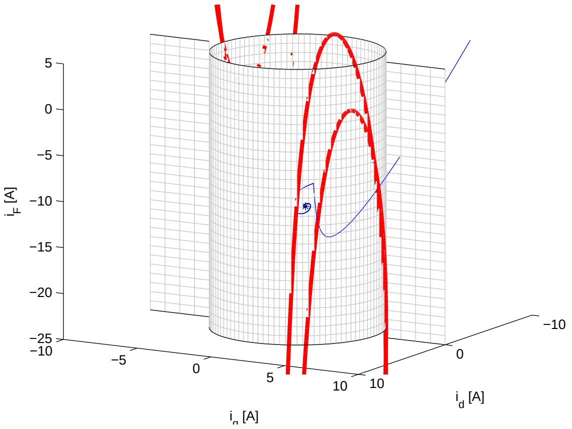

Figure 4.9: State evolution of a trajectory and sliding domains on $s = 0$.

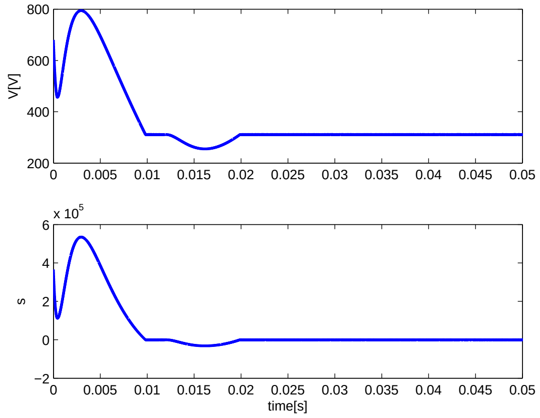

Figure 4.10: Stator voltage amplitude, V_s, and switching function, $s(x)$.

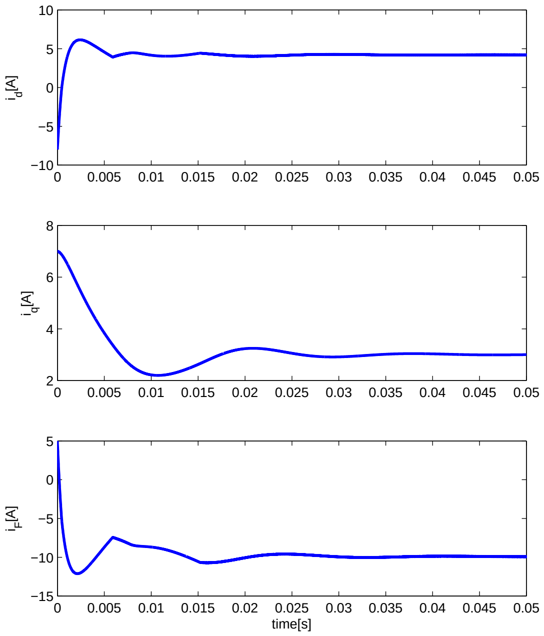

Figure 4.11: Stator and field currents, i_d, i_q and i_F.

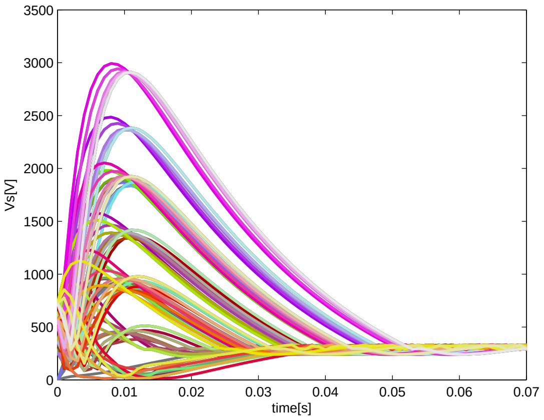

Figure 4.12: Set of trajectories of the stator voltage amplitude, for values in the box defined by the maximal currents.

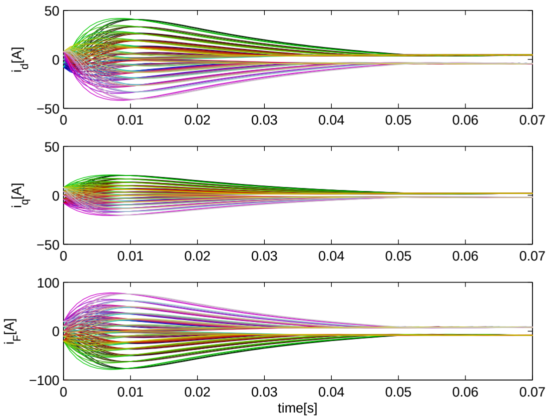

Figure 4.13: Set of trajectories of the state, for values in the box defined by the maximal currents.

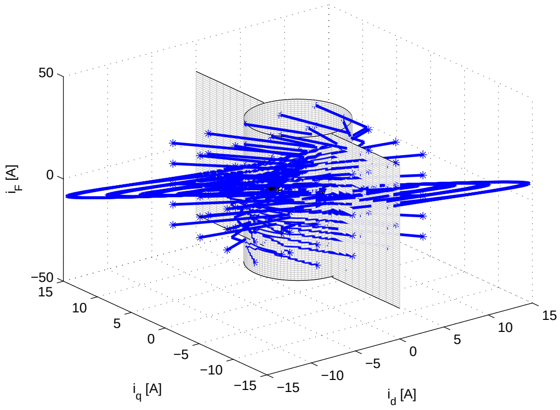

Figure 4.14: Set of trajectories in the 3D space state, for values in the box defined by the maximal currents.

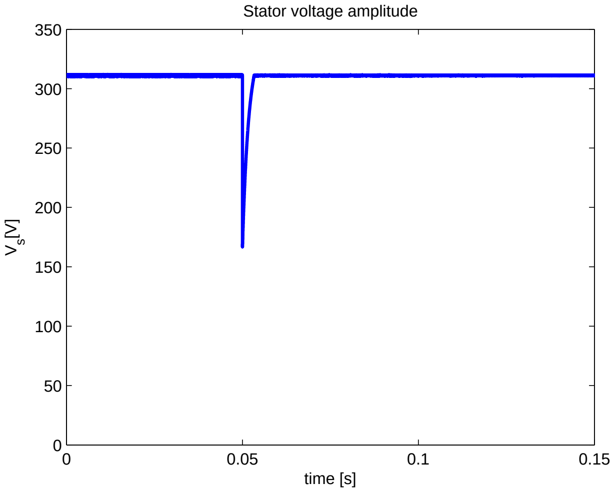

Figure 4.15: Simulation results, CSMC: Stator voltage amplitudes.

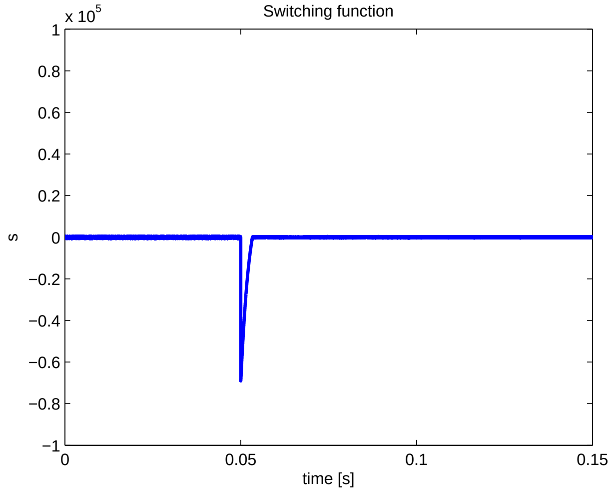

Figure 4.16: Simulation results, CSMC: Switching function.

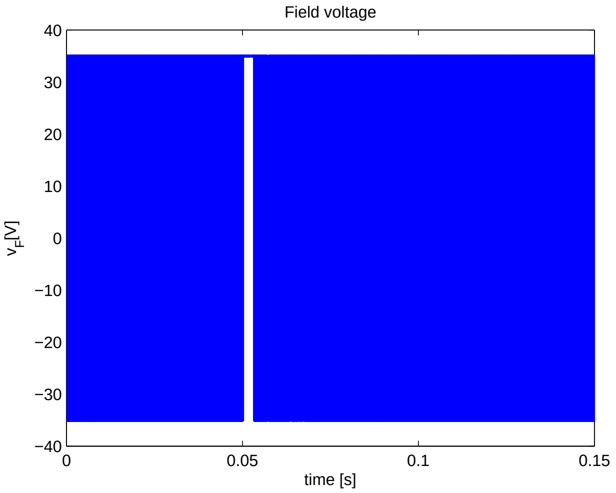

Figure 4.17: Simulation results, CSMC: Field voltage.

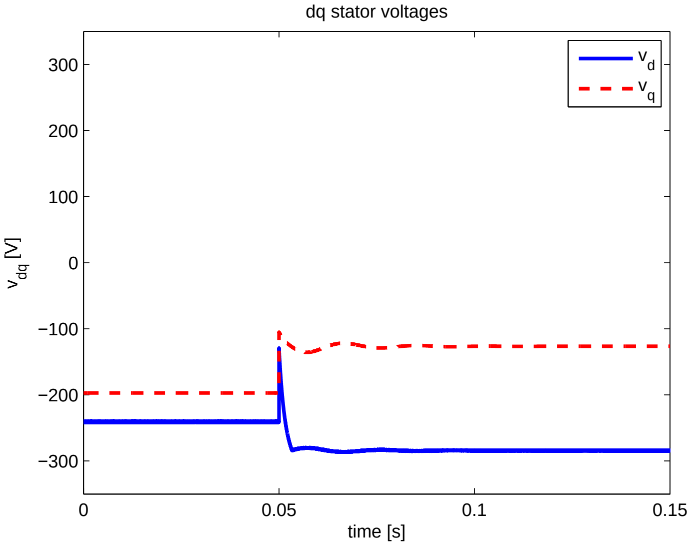

Figure 4.18: Simulation results, CSMC: dq stator voltages.

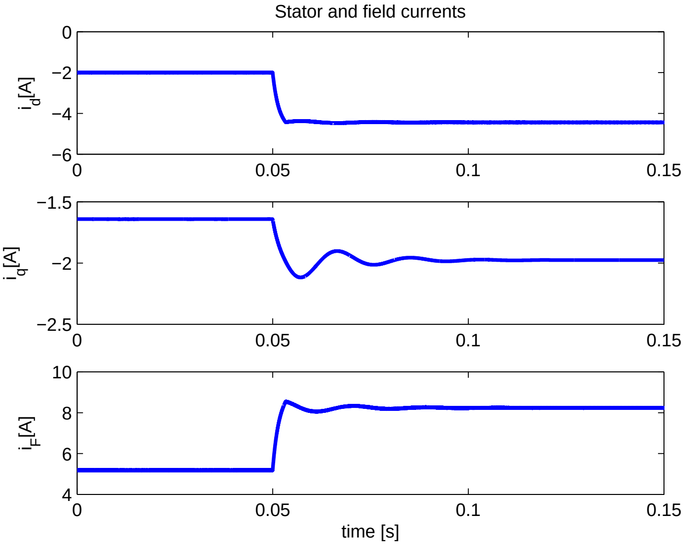

Figure 4.19: Simulation results, CSMC: Stator and field currents.

Chapter 5

Control of a stand-alone wound rotor synchronous generator via the v_d-component

Resume

This chapter presents two new sliding mode designs to regulate the stator voltage amplitude for a stand alone wound rotor synchronous generator. Both use the stator voltage d-component error in the switching function. The first case is a nested controller, where an outer PI loop is added to provide the proper d-voltage component reference. In the second approach an integral term is added to the switching function. Experimental results will show that the second algorithm is not suitable for a real application.

5.1 System description

The dynamical model of an isolated wound rotor synchronous generator with a resistive load was obtained in Section 2.6. The whole system dynamics can be written in an affine form as

$$L\frac{\mathrm{d}x}{\mathrm{d}t} = Ax + Bv_F, \tag{5.1}$$

where,

$$L = \begin{pmatrix} L_s & 0 & L_m \\ 0 & L_s & 0 \\ L_m & 0 & L_F \end{pmatrix},$$

$$A = \begin{pmatrix} -(R_s + R_L) & \omega L_s & 0 \\ -\omega L_s & -(R_s + R_L) & -\omega L_m \\ 0 & 0 & -R_F \end{pmatrix},$$

and

$$B = \begin{pmatrix} 0 \\ 0 \\ 1 \end{pmatrix}.$$

The load equation is,

$$\begin{pmatrix} v_{Ld} \\ v_{Lq} \end{pmatrix} = R_L \begin{pmatrix} i_{Ld} \\ i_{Lq} \end{pmatrix}. \tag{5.2}$$

5.2 Nested loop PI-sliding mode control

In this Section a nested loop control algorithm (NSMC) is proposed. The inner-loop based on the Sliding Mode Control approach (SMC) is in charge of stabilize the system and fix the $d-$component of the stator voltage, v_d. The outer loop provides the reference of the d-component value of the stator voltage, v_d^{ref}, to reach the stator voltage reference, V_{ref}. Roughly speaking, the PI loop moves the switching function and place it at the desired regulation point. Figure 5.1 shows the proposed control algorithm.

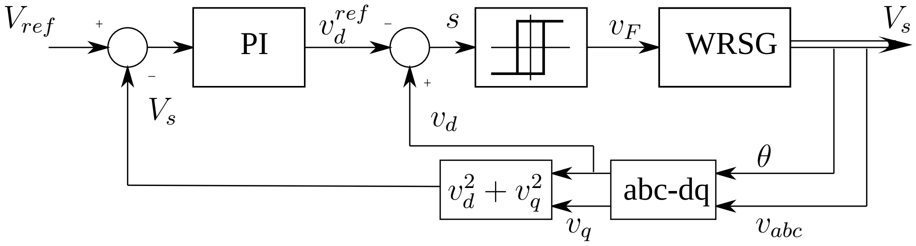

Figure 5.1: Nested loop PI-SMC scheme for a wound rotor synchronous generator.

The whole stability is based on the assumption of a fast inner-loop, with respect to the PI dynamics. This assumption is valid due to the high speed dynamics of the SMC.

5.2.1 Inner-loop: a sliding mode controller

The Sliding Mode Controller (SMC) enforces the system trajectories to reach and keep the switching function

$$s(x) = v_d(x) - v_d^{ref}$$

where v_d^{ref} is defined by the outer-loop PI controller. From (5.2),

$$s(x) = R_L i_d - v_d^{ref}.$$

Note that the surface, $s(x) = 0$, defines the plane $i_d = \frac{v_d^{ref}}{R_L}$. This case differs from the controller presented in Chapter 4, where the sliding surface was a cylinder. The equivalent control, u_{eq}, is the solution of

$$\frac{\partial s}{\partial x} L^{-1}(Ax + Bu_{eq}) = 0, \tag{5.3}$$

and, computing the last expression,

$$u_{eq} = \frac{1}{L_m}(-L_F(R_s + R_L)i_d + \omega L_s L_F i_q + L_m R_F i_F).$$

In order to guarantee sliding motion on $s(x) = 0$, the reachability condition, $s \cdot \frac{\mathrm{d}s}{\mathrm{d}t} < 0$, must be held. From (5.1)

$$s \cdot \frac{\mathrm{d}s}{\mathrm{d}t} = s\frac{\partial s}{\partial x} L^{-1}(Ax + Bv_F) < 0 \tag{5.4}$$

taking into account (5.3), (5.4) results in

$$s\frac{\partial s}{\partial x} L^{-1}B(v_F - u_{eq}) < 0,$$

and after some algebra

$$-s\frac{R_L L_m}{\mu}(v_F - u_{eq}) < 0,$$

finally, as $R_L, L_m, \mu > 0$, the reachability condition yields

$$s(u_{eq} - v_F) < 0.$$

In a real application the rotor voltage is applied trough a power converter using a bang-

bang controller ($v_F = \pm V_{DC}$). This action must bound the equivalent control action so that, $-V_{DC} < u_{eq} < V_{DC}$. Then, the control law becomes the following switching policy

$$v_F = \begin{cases} V_{DC} & \text{if} \quad s > 0 \\ -V_{DC} & \text{if} \quad s < 0 \end{cases}$$

which fulfills the stability condition given by $s \cdot \frac{\mathrm{d}s}{\mathrm{d}t} < 0$.

The Ideal Sliding Dynamics (ISD), is given by the dynamics of (i_q, i_F) in (5.1) where v_F is replaced by u_{eq} and $s = 0$ has been taken into account. It results in the following linear system

$$\frac{\mathrm{d}i_q}{\mathrm{d}t} = -\frac{R_s + R_L}{L_s} i_q - \frac{\omega L_m}{L_s} i_F - \frac{\omega}{R_L} v_d^{ref} \tag{5.5}$$

$$\frac{\mathrm{d}i_F}{\mathrm{d}t} = \frac{\omega L_s}{L_m} i_q - \frac{R_s + R_L}{L_m R_L} v_d^{ref}, \tag{5.6}$$

which is stable since its characteristic equation has positive coefficients due to the positive parameters of the actual machine.

5.2.2 Outer-loop: a PI controller

As said before, the outer-loop consists in a simple PI controller that tunes the d-component voltage reference of the SMC controller. Thanks to the SMC is faster than the outer dynamics, in the design of the PI we may assume the plant is given by the ISD (5.5) and (5.6). As for the output, the nonlinear function to be regulated

$$V_s = \sqrt{\left(v_d^{ref}\right)^2 + R_L^2 i_q^2} \tag{5.7}$$

can be linearized around (v_d^{ref}, i_q^*), which satisfies

$$V_{ref} = \sqrt{(v_d^{ref*})^2 + R_L^2 i_q^{*2}}, \tag{5.8}$$

The linearized output results in

$$V_s \simeq V_{ref} + \frac{v_d^{ref*}}{V_{ref}}(v_d^{ref} - v_d^{ref*}) + \frac{R_L^2 i_q^*}{V_{ref}}(i_q - i_q^*), \tag{5.9}$$

where,

$$v_d^{ref*} = V_{ref}\cos\delta^*. \tag{5.10}$$

Using (5.8), (2.17) and (5.10), equation (5.9) can be rewritten as

$$V_s = v_d^{ref}\cos\delta^* + R_L i_q \sin\delta^*. \tag{5.11}$$

Note that (5.11), which results from linearizing (5.7), is a function of v_d^{ref} and i_q, but it neither depends on v_d^{ref*} nor i_q^*.

Using (5.5), (5.6) and (5.11), the transfer function $G(s) = \frac{V_s(s)}{v_d^{ref}(s)}$[1] is obtained:

$$G(s) = \frac{\cos^2\delta^* s^2 + \omega^2}{\cos\delta^* s^2 + \omega\sin\delta^* s + \omega^2\cos\delta^*}.$$

and the closed loop transfer function results in

$$W(s) = \frac{c_3 s^3 + c_2 s^2 + c_1 s + c_0}{b_3 s^3 + b_2 s^2 + b_1 s + b_0}$$

where $c_3 = k_p\cos^2\delta^*$, $c_2 = k_i\cos^2\delta^*$, $c_1 = k_p\omega^2$, $c_0 = k_i\omega^2$ and

$$\begin{aligned} b_3 &= \cos\delta^*(k_p\cos\delta^* + 1) \\ b_2 &= (\omega\sin\delta^* + k_i\cos^2\delta^*) \\ b_1 &= \omega^2(k_p + \cos\delta^*) \\ b_0 &= k_i\omega^2. \end{aligned}$$

Following the Routh-Hurwitz criterium, this system is stable if b_3, b_2, b_0 and $b_2b_1 - b_3b_0$ have the same sign. Considering that v_d^{ref} only takes its positive value (***i.e.***, $\cos\delta^* > 0$), the stability condition yields

$$\begin{aligned} k_p &> -\frac{1}{\cos\delta^*} \\ k_i &> 0 \\ k_i &< \frac{\omega(k_p\sin\delta^* + \cos\delta^*)}{\cos\delta^*\sin\delta^*}. \end{aligned}$$

---

[1] This transfer function takes the form $G(s) = 1 + Q(s)$.

5.3 Direct sliding mode controller

In this Section, a direct sliding mode controller (DSMC) scheme is presented. The switching function is still based on the error of the d-component of the stator voltage, and an integral action is added in order to robustify the controller. Figure 5.2 shows the proposed control scheme. The main difference between this algorithm and the previous one is the absence of a proportional action in the controller.

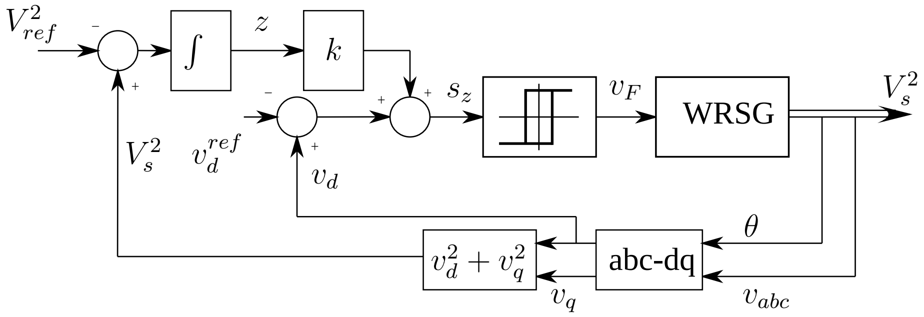

Figure 5.2: Direct sliding mode control scheme for a wound rotor synchronous generator.

5.3.1 Control design

The integral term implies that the system is extended with a new variable, z, which derivative is the error of the stator voltage amplitude,

$$\frac{\mathrm{d}z}{\mathrm{d}t} = V_s^2 - V_{ref}^2.$$

As it is proposed in Chapter 4, the error of the square of stator voltage amplitude is used, to avoid square root function. Then, the switching function, s_z, is

$$s_z = v_d - v_d^{ref} + kz$$

where v_d^{ref} is the nominal value of v_d given V_{ref}. Using the root locus of the equilibrium points (2.16), and (5.2) the reference of the d-component voltage is obtained [2]

$$v_d^{ref} = V_{ref} \cos \tilde{\delta}^*.$$

---

[2] The tilde denotes that this value depends on the estimated values of R_L, R_s and L_s.

Similarly to the previous controller design, the equivalent control is computed, which results in

$$u_{zeq} = u_{eq} + \frac{\mu}{L_m R_L} k \dot{z}.$$

Note that it contains the former equivalent control, u_{eq}, plus the term coming from the new integral variable.

Now, the control is designed with the extended system

$$L_z \frac{\mathrm{d}z_e}{\mathrm{d}t} = A_z(z_e) + B_z v_F \tag{5.12}$$

where $z_e^T = [i_d, i_q, i_F, z]$,

$$L_z = \begin{pmatrix} L_s & 0 & L_m & 0 \\ 0 & L_s & 0 & 0 \\ L_m & 0 & L_F & 0 \\ 0 & 0 & 0 & 1 \end{pmatrix},$$

$$A_z(z_e) = \begin{pmatrix} Ax \\ R_L^2(i_d^2 + i_q^2) - V_{ref}^2 \end{pmatrix}$$

and $B_z^T = (0, 0, 1, 0)$.

Proceeding as usual, using the equivalent control definition, the reachability condition can be obtained from,

$$\begin{aligned} s_z \cdot \frac{\mathrm{d}s_z}{\mathrm{d}t} &= s_z \frac{\partial s_z}{\partial z_e} L_z^{-1}(A_z + B_z v_F) \\ &= s_z \frac{\partial s_z}{\partial z_e} L_z^{-1} B_z (v_F - u_{zeq}) \\ &= -s_z \frac{R_L L_m}{\mu}(v_F - u_{zeq}) \end{aligned}$$

and finally, taking into account $R_L, L_m, \mu > 0$, the reachability condition yields

$$s_z(u_{zeq} - v_F) < 0.$$

Consequently, using again a bang-bang controller, the switching control policy is

$$v_F = \begin{cases} V_{dc} & \text{if} \quad s_z > 0 \\ -V_{dc} & \text{if} \quad s_z < 0 \end{cases} \tag{5.13}$$

presumed that the equivalent control is bounded by the bus voltage, $-V_{dc} < u_{zeq} < V_{dc}$.

Ideal sliding dynamics

The controller defined in (5.13) ensures sliding motion on the sliding surface, $s_z = 0$. The goal of the Ideal Sliding Dynamics is to analyze the remaining dynamics of the system. Using $s_z = 0$, replacing $v_F = u_{zeq}$ in (5.12) and defining a new variable $\xi = v_d^{ref} - kz$, the ideal sliding dynamics can be written as

$$\begin{aligned} \frac{\mathrm{d}i_q}{\mathrm{d}t} &= -\frac{R_s + R_L}{L_s} i_q - \frac{\omega L_m}{L_s} i_F - \frac{\omega}{R_L}\xi \qquad (5.14) \\ \frac{\mathrm{d}i_F}{\mathrm{d}t} &= \frac{kL_sR_L}{\mu L_m} i_q^2 + \frac{\omega L_s}{L_m} i_q + \frac{kL_s}{\mu L_m R_L}\xi^2 - \frac{R_s + R_L}{L_m R_L}\xi \\ &\quad - \frac{kL_s}{\mu L_m R_L R_L} V_{ref}^2 \qquad (5.15) \\ \frac{\mathrm{d}\xi}{\mathrm{d}t} &= -\frac{kR_L^2}{\mu} i_q^2 - \frac{k}{\mu}\xi^2 + \frac{k}{\mu} V_{ref}^2 . \qquad (5.16) \end{aligned}$$

Since this is a nonlinear system, the stability is analyzed using linear techniques. The equilibria is also given by (2.17) and (2.18), while for the new variable ξ,

$$\xi^* = V_{ref} \cos \delta^* .$$

The Jacobian of the ISD defined in (5.14)-(5.16), evaluated in the equilibria is

$$J_z = \begin{pmatrix} -\frac{R_s+R_L}{L_s} & -\frac{\omega L_m}{L_s} & -\frac{\omega}{R_L} \\ \frac{2kL_sR_L}{\mu L_m} i_q^* + \frac{\omega L_s}{L_m} & 0 & \frac{2kL_s}{\mu L_m R_L}\xi^* - \frac{R_s+R_L}{L_m R_L} \\ -\frac{2kR_L^2}{\mu} i_q^* & 0 & -\frac{2k}{\mu}\xi^* \end{pmatrix}$$

and the characteristic polynomial,

$$\lambda^3 + a_2\lambda^2 + a_1\lambda + a_0,$$

where

$$\begin{aligned} a_2 &= \frac{R_s + R_L}{L_s} + \frac{2k}{\mu} V_{ref} \cos \delta^* \\ a_1 &= \frac{2k(R_s + R_L)}{\mu L_s} V_{ref} \cos \delta^* + \omega^2 \\ a_0 &= \frac{2k(\omega^2 L_s^2 + (R_s + R_L)^2)}{\mu L_s^2} V_{ref} \cos \delta^*. \end{aligned}$$

Using the Routh-Hurwitz criteria, this system will be stable if $a_2 > 0$, $a_0 > 0$ and $a_2 a_1 - a_0 > 0$,

$$a_2 a_1 - a_0 = \frac{R_s + R_L}{L_s} \left(\left(\frac{2k\xi}{\mu} \right)^2 + \omega^2 \right).$$

Clearly, due to the fact that $\cos \delta^* > 0$ if $k > 0$[3] these conditions fulfill.

5.4 Simulations

In this Section some simulation results using the designed controller are presented. The used WRSG is a 2.4kW machine with the following parameters: $R_s = 3.06\Omega$, $L_s = 0.48$H, $L_m = 0.31$H, $R_F = 2.48\Omega$, $L_F = 0.24$H, $\omega = 2 \cdot \pi 50$, $V_{dc} = 35$V.

Initial conditions are set to $V_{ref} = 200\sqrt{2}$V with a resistive load $R_L = 120\Omega$. Simulation test shows the response of the closed loop system for a load change to $R_L = 64\Omega$ at $t = 0.05$s. The controller gains are: $k_p = 1000$, $k_i = 100$ (of the NSMC) and $k = 0.2$ (of the DSMC). Simulations have been performed using a variable step integration method, with a zero order hold with 20kHz of sample frequency. Figure 5.3 shows the stator voltage amplitudes. In both case, regulation of the stator voltage amplitude is achieved. The faster response of the first controller algorithm is thanks to the proportional action of the PI loop.

Figure 5.4 shows the switching functions. Note that for the secondth control law, the sliding motion is lost twice for a short time after the load change. The first time is due to the sudden load variation, while the second time is consequence of the equivalent control

---

[3] As it was pointed out in Chapter 4, two equilibria are possible. To reach the value corresponding to $\delta^* = \arctan\left(\frac{R_s + R_L}{\omega L_s}\right) + \pi$, the stability condition also is obtained when $k < 0$.

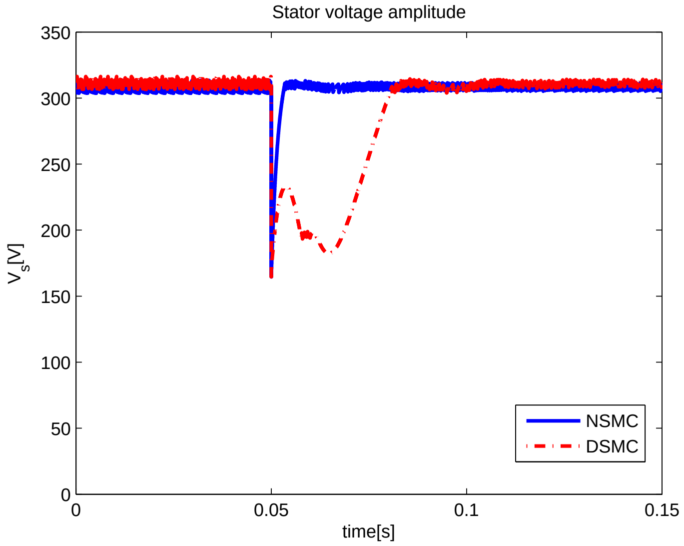

Figure 5.3: Simulation results, NSMC and DSMC: Stator voltage amplitudes.

(5.3) is out of range ($|u_{zeq}| > V_{dc}$), see also in Figure 5.5, where the field voltage, v_F is shown, the long time where it remains saturated compared with the NSMC control law.

Response velocity can be observed in Figures 5.6 and 5.7, where the dq stator voltages and the currents (the stator and field ones) are displayed, respectively. The faster response of the first controller is clear.

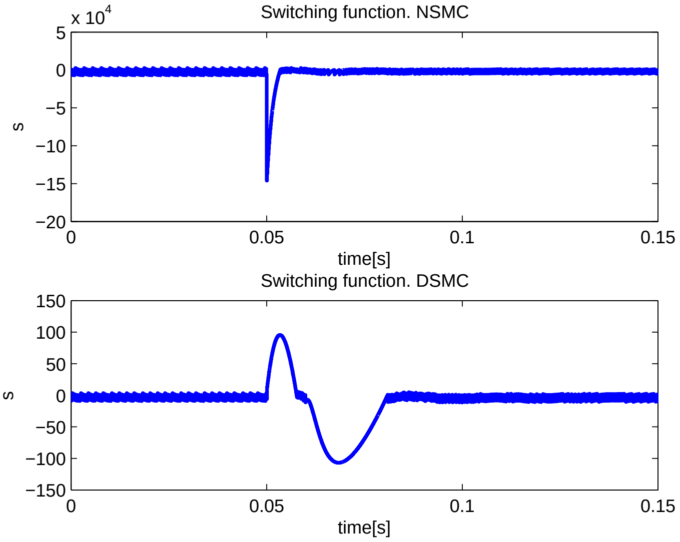

Figure 5.4: Simulation results, NSMC and DSMC: Switching functions.

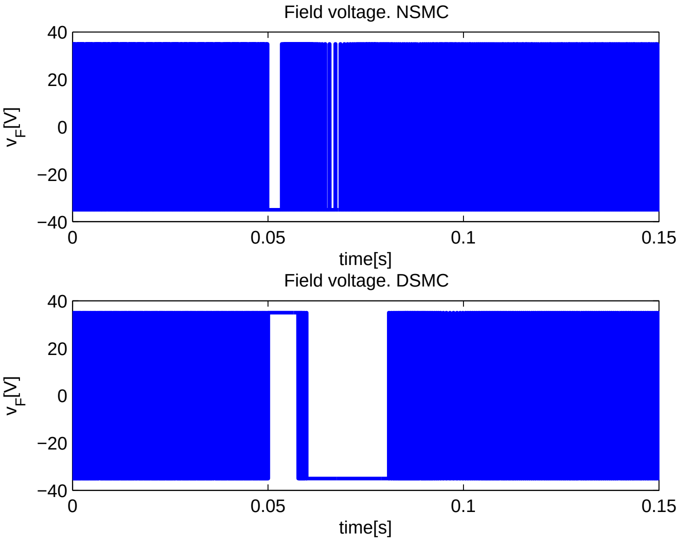

Figure 5.5: Simulation results, NSMC and DSMC: Field voltages.

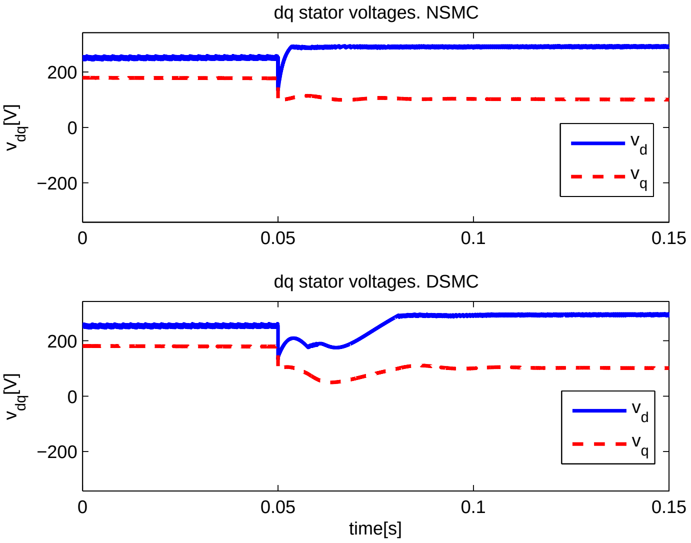

Figure 5.6: Simulation results, NSMC and DSMC: dq stator voltages.

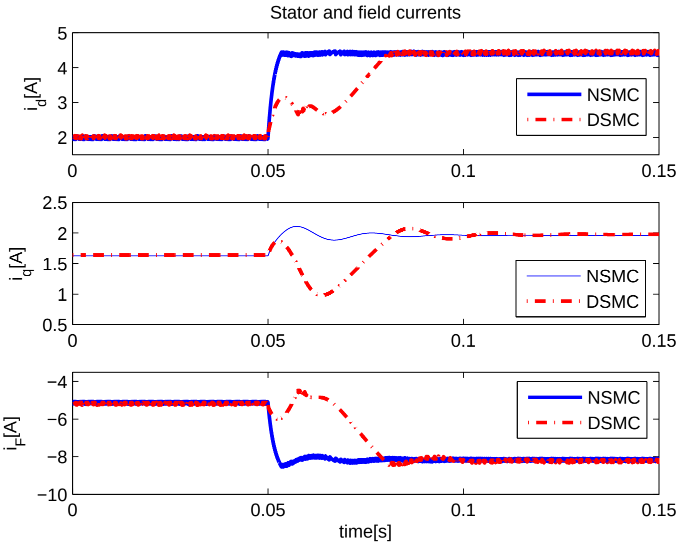

Figure 5.7: Simulation results, NSMC and DSMC: Stator and field currents.

Chapter 6

Control of a stand-alone wound rotor synchronous generator with an inductive load

Resume

In this chapter a sliding mode controller for the stator voltage amplitude of a stand-alone wound rotor synchronous generator with an inductive load is presented. The controller introduces a dynamic extension to prevent the stator amplitude is a zero relative degree output. As a result, a robust controller, which neither depends on the machine parameters nor on the load values, is obtained.

6.1 System description

6.1.1 Dynamical model

The interconnection of a stand-alone wound rotor synchronous generator with an inductive load was studied in Section 2.7. In this case, the electrical dynamics can be written as

$$\hat{L}\frac{\mathrm{d}x}{\mathrm{d}t} = \hat{A}x + Bv_F, \tag{6.1}$$

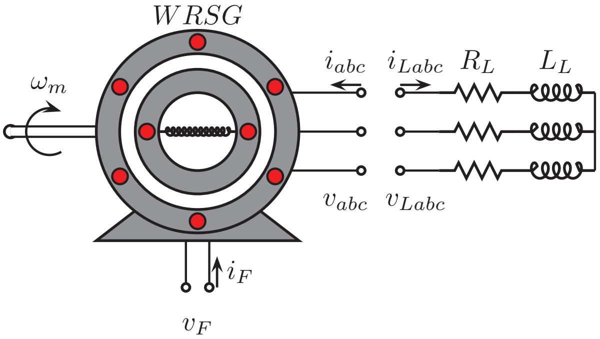

Figure 6.1: Scheme of an isolated WRSG with an isolated load.

---

where $\hat{L}$ is a new inductance matrix,

$$\hat{L} = \begin{pmatrix} L_s + L_L & 0 & L_m \\ 0 & L_s + L_L & 0 \\ L_m & 0 & L_F \end{pmatrix}$$

and the homogeneous dynamics A and the input vector B are given by

$$\hat{A} = \begin{pmatrix} -(R_s + R_L) & \omega(L_s + L_L) & 0 \\ -\omega(L_s + L_L) & -(R_s + R_L) & -\omega L_m \\ 0 & 0 & -R_F \end{pmatrix},$$

and

$$B = \begin{pmatrix} 0 \\ 0 \\ 1 \end{pmatrix}.$$

The load equation is,

$$v_L = (R_L I_2 + \omega L_L J_2) i_L + L_L \frac{\mathrm{d}}{\mathrm{d}t} i_L.$$

6.2 Control design

In this Section the Sliding Mode Control technique is applied to an isolated wound rotor synchronous generator feeding an inductive load. First, after defining the switching function, the equivalent control is computed and the controller is obtained. As mentioned before, the standard design is modified to avoid the zero relative degree output problem if v_F is used as control input. Finally, to complete the control design the Ideal Sliding Dynamics is analyzed to ensure stability.

6.2.1 Switching function and equivalent control

According to the control goals, and taking V_s^2 to avoid the square root function of stator voltage amplitude, the switching function $s(x)$ is defined as

$$s(x) = V_s^2 - V_{ref}^2. \tag{6.2}$$

where V_s^2, $\frac{\mathrm{d}i_d}{\mathrm{d}t}$ and $\frac{\mathrm{d}i_q}{\mathrm{d}t}$ are respectively given in (2.29), (2.30) and (2.31).

As $\frac{\mathrm{d}i_d}{\mathrm{d}t}$ depends on v_F, $s(x)$ is relative degree zero with respect to v_F. Therefore, system (6.1) is expanded by considering v_F as a state variable and taking its derivative as a fictitious input, ***i.e.*** it is defined a new input u by

$$\frac{\mathrm{d}v_F}{\mathrm{d}t} = ku, \tag{6.3}$$

where k is a positive constant.

Let us rewrite the extended system, with the new state vector $z^T = (i_d, i_q, i_F, v_F)$, as

$$\mathcal{L}\frac{\mathrm{d}z}{\mathrm{d}t} = \mathcal{A}z + \mathcal{B}u, \tag{6.4}$$

where

$$\mathcal{A} = \begin{pmatrix} -(R_s+R_L) & \omega(L_s+L_L) & 0 & 0 \\ -\omega(L_s+L_L) & -(R_s+R_L) & -\omega L_m & 0 \\ 0 & 0 & -R_F & 1 \\ 0 & 0 & 0 & 0 \end{pmatrix},$$

$$\mathcal{L} = \begin{pmatrix} \hat{L} & 0 \\ 0 & 1 \end{pmatrix}$$

and

$$\mathcal{B} = \begin{pmatrix} 0 \\ 0 \\ 0 \\ k \end{pmatrix}.$$

The equivalent control, u_{eq}, is defined so that $\dot{s} = 0$,

$$\frac{\mathrm{d}s}{\mathrm{d}t} = \frac{\partial s}{\partial z}\frac{\mathrm{d}z}{\mathrm{d}t} = 0.$$

Then, from (6.4),

$$\frac{\partial s}{\partial z}\mathcal{L}^{-1}\left(\mathcal{A}z + \mathcal{B}u_{eq}\right) = 0.$$

Hence

$$u_{eq} = -\left(\frac{\partial s}{\partial z}\mathcal{L}^{-1}\mathcal{B}\right)^{-1}\frac{\partial s}{\partial z}\mathcal{L}^{-1}\mathcal{A}z. \tag{6.5}$$

From (4.3) and (2.28),

$$\frac{\partial s}{\partial z} = \frac{\partial v_d^2}{\partial z} + \frac{\partial v_q^2}{\partial z} = 2\left(v_d\frac{\partial v_d}{\partial z} + v_q\frac{\partial v_q}{\partial z}\right)$$

and taking into account that $\mathcal{B}$ has zeros in the first, second and third row, $\mathcal{L}^{-1}$ contains only a non-zero term in the fourth row and v_q does not depend on v_F,

$$\begin{aligned}\frac{\partial s}{\partial z}\mathcal{L}^{-1}\mathcal{B} &= v_d\frac{\partial}{\partial v_F}\left(L_L\frac{\mathrm{d}i_d}{\mathrm{d}t}\right)k\\ &= 2k\frac{L_L L_m}{\mu_d}v_d,\end{aligned}$$

which implies

$$u_{eq} = -\frac{\mu_d}{2kL_L L_m}\frac{1}{v_d}\left(\frac{\partial s}{\partial z}\mathcal{L}^{-1}\mathcal{A}z\right). \tag{6.6}$$

Note that sliding motion can only be expected in the subspace defined by $v_d \neq 0$.

6.2.2 Ideal sliding dynamics

The Ideal Sliding Dynamics (ISD) is defined on the sliding surface presumed that it is invariant by the flow. Replacing $u = u_{eq}$ from (6.6) into (6.4) and solving $v_F(x)$ from $s(x) = 0$ (6.2), the remaining dynamics can be rewritten as

$$\dot{x} = \hat{L}^{-1}\left(\hat{A}x + Bv_F(x)\right), \tag{6.7}$$

Note also, that the extended system is symmetric with respect to the origin. This is straightforward for the linear part of the dynamics defined by matrix $\hat{A}$, while, for the nonlinear part of $v_F(x)$, $s(x, v_F) = s(-x, -v_F)$. Consequently, it is sufficient to analyze stability in one of the two equilibrium points given by (2.27) and (2.32).

Linearizing (6.7) around the equilibrium point one obtains

$$\hat{L}\dot{x} = \left(\frac{\partial}{\partial x} \left(\hat{A}x + Bv_F(x) \right) \Big|_{x=x^*} \right) (x - x^*).$$

And simplifying

$$\hat{L}\dot{x} = \hat{A}_{lin}(x - x^*),$$

where

$$\hat{A}_{lin} = \hat{A} + B \left. \frac{\partial v_F}{\partial x} \right|_{x=x^*}. \tag{6.8}$$

Stability depends on the eigenvalues of (6.8), which can be numerically computed. For the experimental case presented in Chapter 7 (with a squirrel cage induction machine and a resistive bank) the eigenvalues of matrix $\hat{A}_{lin}$ are $\lambda = -204.03$,and $-35.21 \pm 337.16\,j$, hence the ISD is locally stable.

In order to analyze the load range values where the stability of the ISD is guaranteed, let us compute the characteristic polynomial of $\hat{A}_{lin}$

$$\lambda^3 + a_2\lambda^2 + a_1\lambda + a_0,$$

where

$$\begin{aligned} a_2 &= 2(R_s + R_L) - d_3 \\ a_1 &= |Z_s|^2 + \omega L_m d_2 - 2(R_s + R_L)d_3 \\ a_0 &= \omega^2 L_m(L_s + L_L)d_1 + \omega L_m(R_s + R_L)d_2 - |Z_s|^2 d_3, \end{aligned}$$

and

$$\begin{aligned} d_1 &= \frac{L_F}{L_m L_L}\Phi - R_L\frac{L_m}{L_L} \\ d_2 &= \omega L_m + \frac{\mu_d(\omega^2 L_L(L_s + L_L) + R_L(R_s + R_L))}{\omega L_m L_L(L_s + L_L)} \\ d_3 &= -\frac{\mu_d(\omega^2 L_L(L_s + L_L) + R_L(R_s + R_L))}{\Phi(L_s + L_L)} \end{aligned}$$

where, in turn, $\Phi = R_L L_s - L_L R_s$. From the Routh-Hurwitz criterion, sufficient condi-

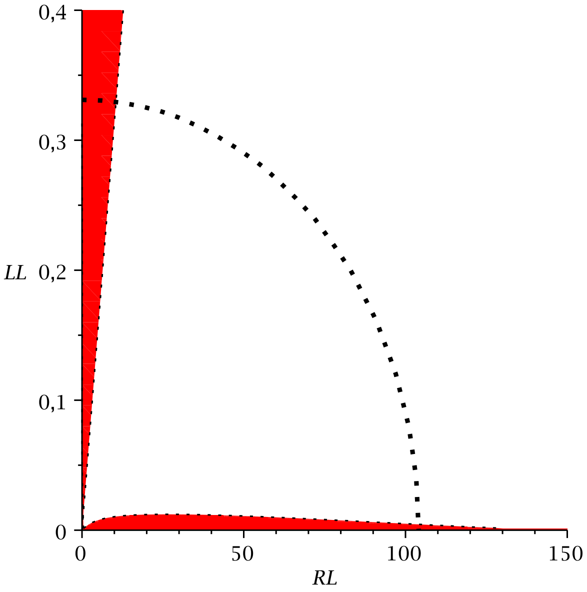

Figure 6.2: Stability margins of the ISD as a function of R_L and L_L.

tions for stability are

$$a_2, a_0 > 0 \tag{6.9}$$

together with

$$a_2 a_1 - a_0 > 0. \tag{6.10}$$

Notice that a sufficient condition for (6.9) is $\Phi > 0$, which implies

$$L_L < \frac{L_s}{R_s} R_L.$$

Condition (6.10) is a polynomial function which is strongly dependent on the load parameters. Replacing the WRSG parameters it is easy to obtain the ISD stable region.

The WRSG stability range is a function that depends on R_L and L_L as it is depicted in Figure 6.2. Machine parameters given in Chapter 7 have been used. The colored zone corresponds to the unstable region. Also, the dotted line represents the R_L and L_L values corresponding to the nominal power. Note that stability is guaranteed for a large range of load values.

6.2.3 Sliding mode controller

Sliding mode controller is in charge of approaching trajectories to the switching surface and, when it is reached, trajectories remain on the sliding surface. In order to define the control action for the extended system (6.4) and the switching function given in (6.2), the following condition must be ensured

$$s\frac{\mathrm{d}s}{\mathrm{d}t} < 0 \tag{6.11}$$

which, after some algebra, is equivalent to,

$$s\frac{\partial s}{\partial z}\mathcal{L}^{-1}\left(\mathcal{A}z + \mathcal{B}u\right) < 0.$$

Adding and subtracting $\mathcal{B}u_{eq}$ and taking into account (6.5), this equation is equivalent to

$$s\frac{\partial s}{\partial z}\mathcal{L}^{-1}\mathcal{B}\left(u - u_{eq}\right) < 0.$$

Evaluating $\frac{\partial s}{\partial z}\mathcal{L}^{-1}\mathcal{B}$, and taking into account $\frac{2kL_L L_m}{\mu_d} > 0$, the reachability condition becomes

$$-sv_d\left(u - u_{eq}\right) < 0.$$

Hence, the control action is defined as

$$u = u_{eq} + \text{ sign}\left(sv_d\right),$$

fulfills the reachability condition (6.11). Namely,

$$s\frac{\mathrm{d}s}{\mathrm{d}t} = -\left|sv_d\right| < 0.$$

If the control input u takes values in the discrete set $\{u_1, u_2\}$, where $u_1 < u_2$, the control law can be defined as

$$u = \begin{cases} u_1 & \text{if} \quad sv_d < 0 \\ u_2 & \text{if} \quad sv_d > 0 \end{cases}.$$

which also assures (6.11) in the subset of the sliding surface where $u_1 \leq u_{eq} \leq u_2$. Note that the (fictitious) control law, u, is a function that neither depends on the load values nor the machine parameters. In turn, the corresponding switching function only depends on v_d and v_q (that are measured), hence, this control is robust to parameter variations and load values.

A more complicated task is to determine the range of $[u_1, u_2]$ analytically to ensure sliding modes. This is not trivial because u_{eq} is a complex function and it depends on the state values, see equation (6.6). A simple analysis allows to show that in the equilibrium $u_{eq}^* = 0$. Namely, from (6.6),

$$u_{eq}^* = -\frac{\mu_d}{2kL_L L_m}\frac{1}{v_d^*}\left(\frac{\partial s}{\partial z}\mathcal{L}^{-1}\mathcal{A}z^*\right),$$

and taking into account the expressions of $\mathcal{A}$ and $\mathcal{B}$ in (6.4), the equilibrium point z^* must fulfill $\mathcal{A}z^* = 0$. There is only one condition to ensure sliding modes in a neighborhood of the ideal sliding dynamics equilibrium point. The condition is $u_1 < 0 < u_2$.

Finally, using (6.3), the rotor voltage can be obtained from

$$v_F = k\int u \,\mathrm{d}t.$$

In the actual application, the control input v_F is bounded by the power converter voltage. As for implementing this control action, it is just needed to measure the rotor position (to compute the dq transformation) and the stator voltage.

Figure 6.3 shows the proposed control scheme. Note that, as a result of the control design, the error of the square of the stator voltage amplitude is multiplied by the v_d voltage. The resulting control action, v_F is a continuous signal which in a real plant would be implemented using a pulse width modulation (PWM) applied trough a power converter.

6.3 Simulations

The ESMC simulation results are presented in this Section. The used WRSG is also a 2.4kW machine with the following parameters: $R_s = 3.06\Omega$, $L_s = 0.48$H, $L_m = 0.31$H, $R_F = 2.48\Omega$, $L_F = 0.24$H, $\omega = 2\cdot\pi 50$, $V_{dc} = 35$V.

Initial conditions are set in $V_{ref} = 200\sqrt{2}$V with a resistive-inductive load $R_L = 120\Omega$ and $L_L = 0.1$H. Simulation test shows the response of the closed loop system for a

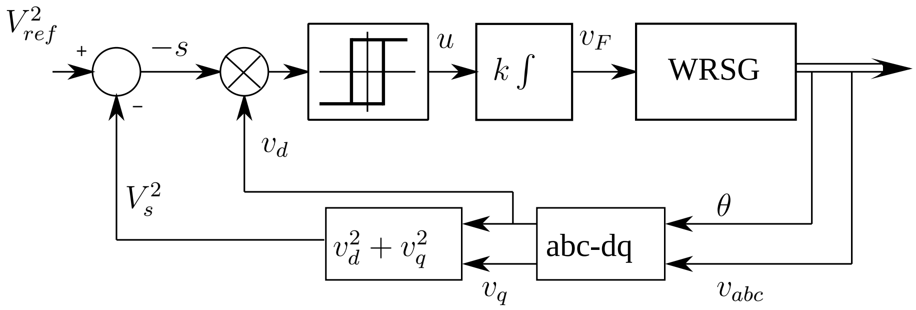

Figure 6.3: Block scheme of a Sliding Mode Controller for a stand-alone wound rotor synchronous generator with an inductive load.

load change to $R_L = 64\Omega$ and $L_L = 0.05$H at $t = 0.05$s. The control values are fixed to $k = 1$, $u_1 = -10^5$ and $u_2 = 10^5$, and it is implemented by an hysteresis function.

In Figure 6.4, the stator voltage amplitude, V_s, is depicted. Note that, even if the R_L and L_L values are suddenly modified, the steady state value of the output is the desired one, and also the convergence-time is small.

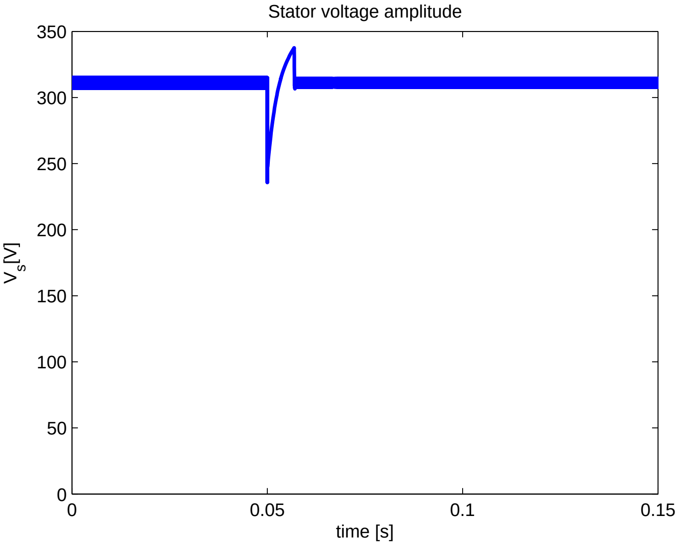

Figure 6.4: Simulation results, ESMC: Stator voltage amplitude.

The switching function, s, is shown in Figure 6.5. The selected values of u_1 and u_2 allow to keep the system on the sliding surface except in a small interval when the load change happens.

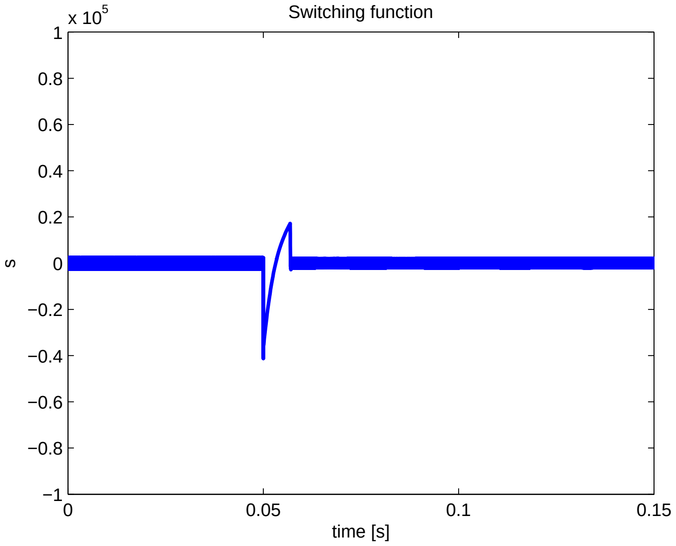

Figure 6.5: Simulation results, ESMC: Switching function.

Figure 6.6 shows the field voltage, v_F. This is the real voltage fed to the WRSG, and it remains in a real applicable values. Note additionally that the dynamics of the control action stabilizes the output response. This is due to the fact that the ISD, is slower than the output dynamics, see Figures 6.7 and 6.8, where the dq stator voltages and the currents (the stator and field ones) are displayed, respectively.

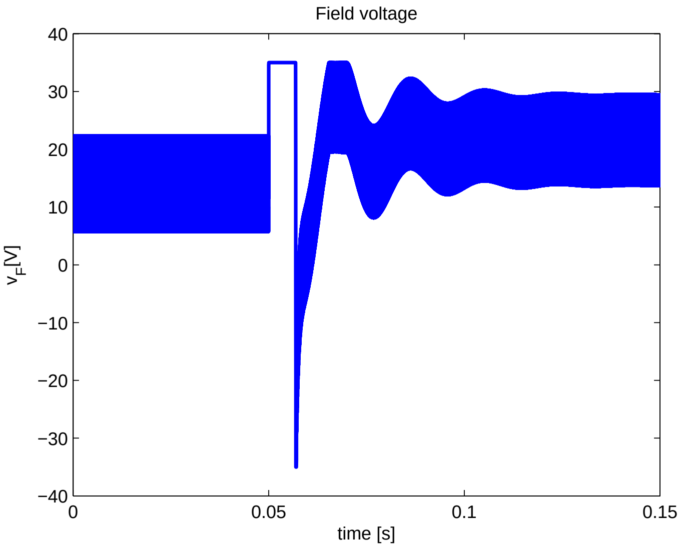

Figure 6.6: Simulation results, ESMC: Field voltage.

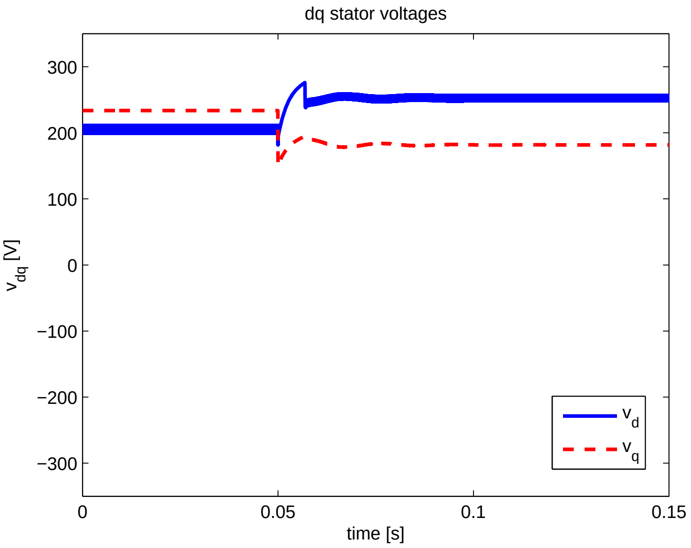

Figure 6.7: Simulation results, ESMC: dq stator voltages.

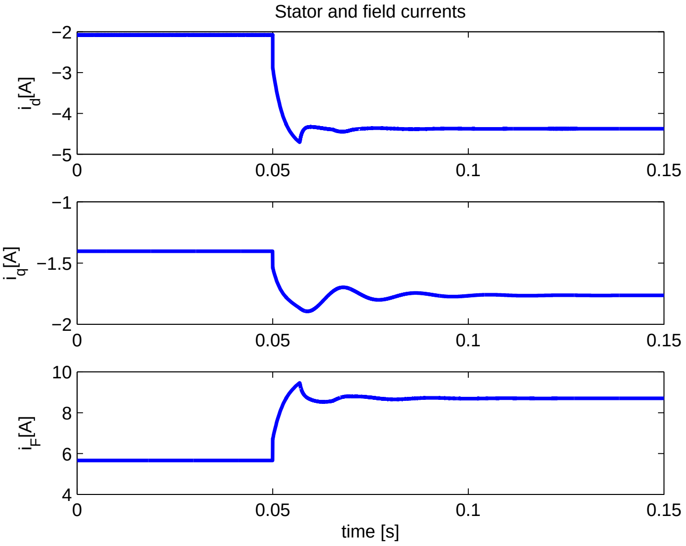

Figure 6.8: Simulation results, ESMC: Stator and field currents.

Chapter 7

Simulation and experimental results

Resume

In this Chapter the simulation and the experimental results of the designed controllers for the stand-alone wound rotor synchronous generator are presented. Firstly, a complete description of the bench is provided. It also includes details of the data acquisition stage and the used DSP card. Secondly, the description of the simulation procedure is commented. Then, the simulations and experiments which contain several scenarios, including the performance of each controller to changes in the reference and load variations are presented.

7.1 Hardware description

The experimental setup hardware scheme is shown in Figure 7.1. The WRSG is dragged by a DC motor (which acts as a primary mover). Using two differential sensors the WRSG stator voltages are measured. The rotor position is obtained with a resolver coupled to the DC motor in order to compute the voltage dq-transformation. This transformation is required because the controllers designed previously works in this reference frame. These measures are acquired by the DSP which is programmed from a personal computer. The grid voltage is rectified in order to provide the DC bus voltage to the DC/DC power converter which applies the control defined by the DSP card to the WRSG.

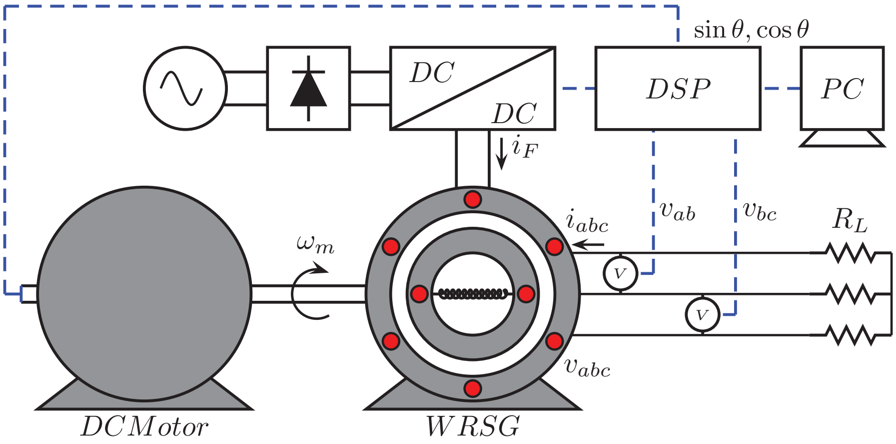

Figure 7.1: Interconnection scheme of the experimental setup.

The actual experimental setup used to validate the proposed controllers is shown in Figures 7.2 and 7.3. The system (Figure 7.2) is composed of a wound rotor synchronous generator dragged by a DC Motor and a resistive bank as local load. The power converters, voltage sensors and control cards are depicted in Figure 7.3.

7.1.1 The DC motor and its control hardware

The DC motor used to provide constant speed for the WRSG which is shown in Figure 7.4. The machine is connected to an independent excitation and, the nameplate data are shown in table 7.1.

$V_{exc} = 220$V	$I_{exc} = 15.5$A	$P = 3$kW
$V_F = 200$V	$I_F = 1.4$A	$n = 1500$rpm

Table 7.1: Nameplate data of the DC motor.

In Figure 7.5 the 4Q2 commercial speed controller from Control Techniques Drives Ltd is shown. This equipment is used to control the DC motor. For more detailed information see [47].

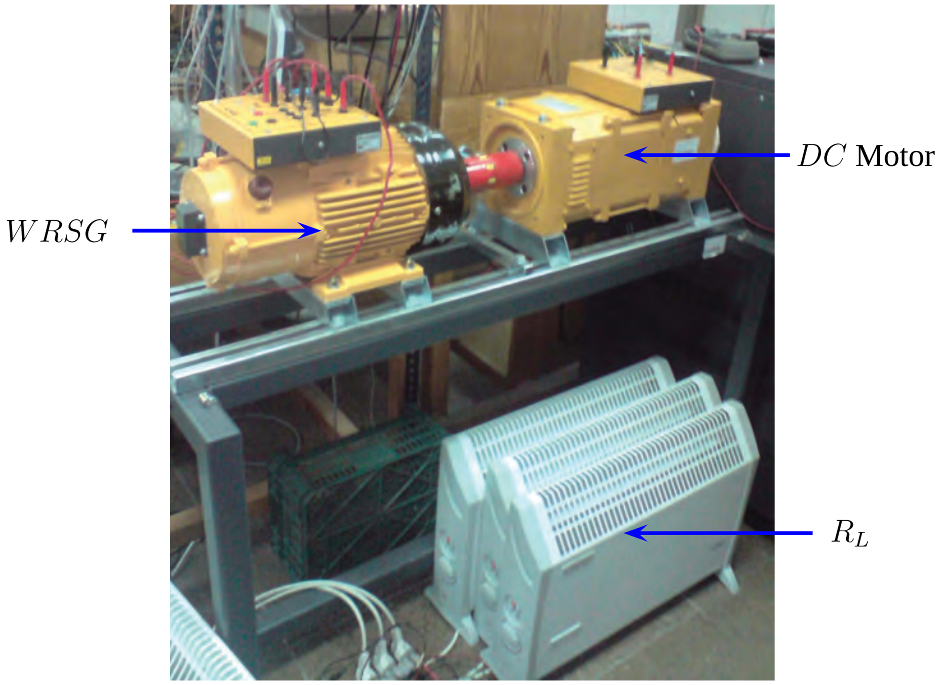

Figure 7.2: Experimental setup: Wound Rotor Synchronous Generator, Direct Current Motor and Resistive Load Bank.

7.1.2 The wound rotor synchronous machine and its control hardware

The WRSG is a 2.4kVA, 4 poles three-phase machine, that can be connected in Y or Δ. The machine is depicted in Figure 7.6 and its nameplate data is shown in table 7.2. Note that the DC motor and the WRSG have similar rated power.

$f = 50\text{Hz}$	$n = 1500\text{rpm}$	$P = 2.4\text{kVA}$
3ph	Δ/Y	$V_F = 100\text{V}$
$I_F = 2.4\text{A}$	$V_s = 220/380\text{V}$	$I_s = 6.3/3.65\text{A}$

Table 7.2: Nameplate data of the WRSG.

The WRSG parameters obtained using IEEE Std. 115-1995 [35], are shown in Table 7.3[1].

---

[1] The apostrophe signal indicates that the parameters are referred from the rotor to the stator, and n is the transformation relationship

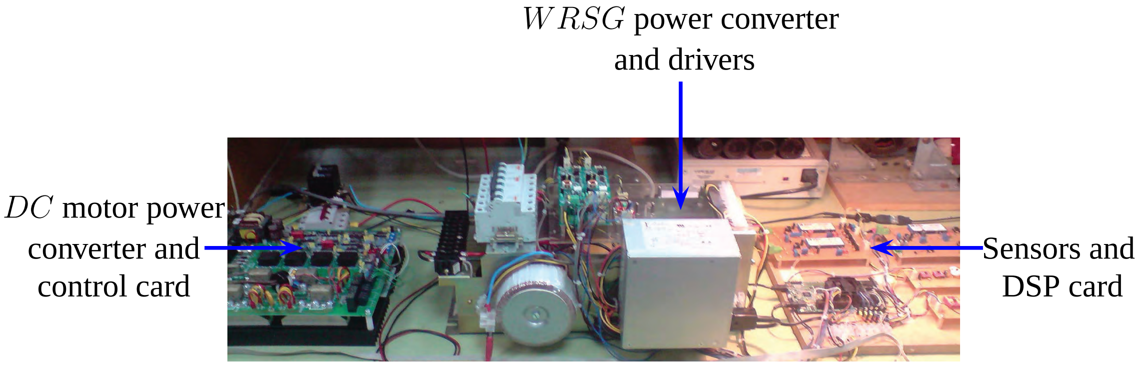

Figure 7.3: Experimental Setup: Control Cards and power converters for the Wound Rotor Synchronous Generator and the DC Motor.

Figure 7.4: DC motor.

The voltage sensors, its power supply, the DSP control card, and the digital to analog converter implemented to measure internal states of the DSP (For example the switching function or the equivalent control) are depicted in Figure 7.7.

The power converter (Figure 7.8), is a full bridge DC/DC converter, which can provide $\pm V_{DC}$ voltages. The V_{DC} voltage is obtained from the power grid with a diode rectifier, a L filter and a capacitor for the DC bus. In the experimental tests the bus voltage is set to $V_{DC} \approx 137.5\text{V}$.

$R_s = 3.06\Omega$	$L_s = 0.48\text{H}$	$R_F = 39.65\Omega$
$L_m = 0.31\text{H}$	$L_F = 3.87\text{H}$	$n = 4$
$R'_F = 2.48\Omega$	$L'_F = 0.24\text{H}$	

Table 7.3: WRSG parameters.

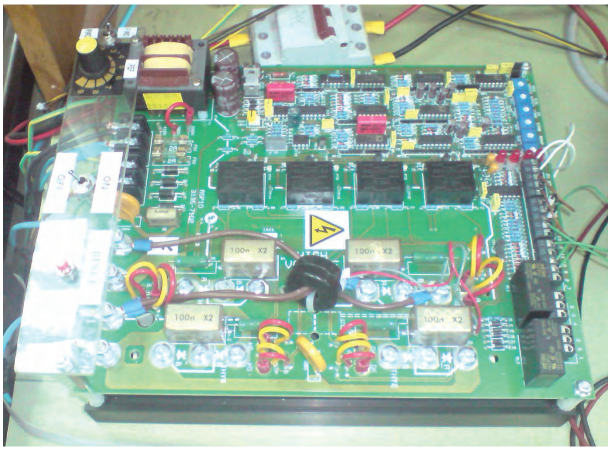

Figure 7.5: DC motor control card

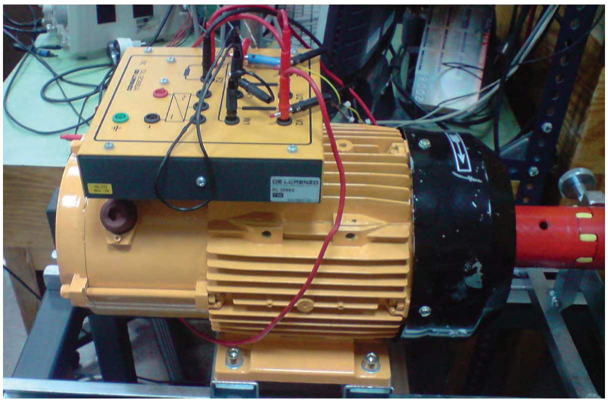

Figure 7.6: Wound rotor synchronous machine.

7.1.3 Local loads

The load is composed by two interconnected resistive banks, with a half or full load values (equivalent to $R_L = 128\Omega$ and $R_L = 64\Omega$ for the nominal voltage) and a 736W squirrel cage induction machine as inductive load ($R_{eq} \approx 64\Omega$ $L_{eq} \approx 1.36$H).

7.1.4 Control implementation

The control algorithm is programmed into a Texas Instruments floating point 150Mhz Digital Signal Processor (DSP TMS 320F28335). The DSP has 16 ADC channels with 12-bit resolution, with a maximum conversion speed of 12.5 MSPS, 6 PWM and 6 HRPWM outputs and 88 GPIO pins which can be used for communication purposes [36].

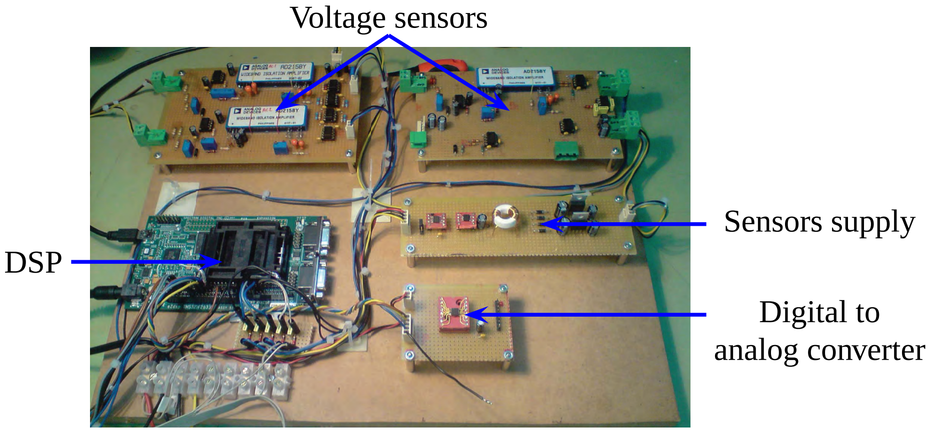

Figure 7.7: Sensors and DSP.

Real Time Workshop C code generation from Matlab/Simulink is used in order to simplify the code implementation to the DSP without using directly a C code editor. Texas Target support package is used to configure the ADC, PWM, SPI, GPIO ports and interruptions.

PI and ESMC controllers are implemented through a PWM. The switching frequency of the PWM used in our experiments is 10kHz. As for CSMC, NSMC and DSMC controllers, the output is a discontinuous signal that has been implemented so that a maximum 10kHz switching frequency is allowed.

7.2 Simulation description

The simulations were performed using a co-simulation procedure with Matlab/Simulink and Psim softwares. There are some advantages using this simulation technique. It allows to use the same block controller, coded in Matlab/Simulink, for simulations and also for experimental tests. Then, permits to obtain previous results of the real controllers before programming it in the actual system (DSP controller) and provides simulation results that are very close to the actual system performance, which is really helpful for implementation purposes.

Practically all hardware of the real plant, DC/DC power converter, acquisition stages, etc, are build in the Psim for simulations purposes. The reason for doing that is the

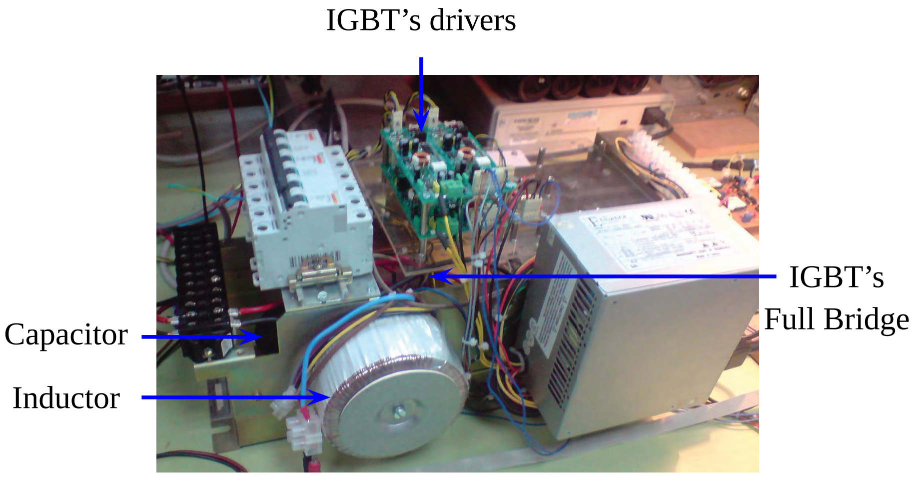

Figure 7.8: WRSG DC/DC power converter.

computation time, the switching action in Psim is calculated faster than Matlab. The WRSG was build using the Matlab's Power System Blockset which have robust machine and load models.

According to the sample time programmed into the DSP, a simulation time step of $1e^{-4}$s is used in Matlab while a time step of $1e^{-6}$s is used in Psim. Due to co-simulation procedure, the Newton integration method (ode14x) is used in Matlab and the trapezoidal rule integration algorithm is used in Psim.

7.3 Simulation and experimental results

A group of simulations and experiments are carried out in this Section. There are several scenarios to validate: a load change, a load connection and a reference change, each one with a resistive and an inductive load. In this sense, for each controller have been done six tests. All of the controllers designed in this Thesis were tested for the same scenarios. The following acronyms are used. Chapter 3 PI, Chapter 4 CSMC, Chapter 5 NSMC and DSMC and, Chapter 6 ESMC. The mechanical speed is fixed at 1500rpm (which corresponds to 50Hz stator frequency).

The first and second experiment consist in validating the controller performance with a resistive load. The reference line voltage is set to 380Vrms (which corresponds to

$V_s = 220\sqrt{2}$V), and the load is suddenly changed from no load to the half load value and from the half to the full load value, respectively.

The third and fourth experiments are similar to the previous ones, but in this case the closed-loop system performance is analyzed for an inductive load with a reference line voltage set to 380Vrms. In the third experiment the generator is without load and suddenly an induction machine is connected. Finally, in the fourth experiment the initial load corresponds to the half load value, and after that, the induction machine is connected.

Second group of experiments consists in a stator voltage amplitude reference change. From an initial value of 250Vrms the reference is set to 380Vrms. In the first case the load keeps to its half value and in the second case the load is the induction machine.

Simulation results are shown in Figures from 7.9(a) to 7.14(c) for the PI, in Figures from 7.15(a) to 7.20(c) for the CSMC, in Figures from 7.21(a) to 7.26(c) for the NSMC, in Figures from 7.27(a) to 7.31(c) for the DSMC, and in Figures from 7.32(a) to 7.37(c) for the ESMC. While the experimental results are shown in Figures from 7.38(a) to 7.43(b) for the PI, in Figures from 7.44(a) to 7.49(b) for the CSMC, in Figures from 7.50(a) to 7.55(b) for the NSMC, in Figures from 7.56(a) to 7.61(b) for the DSMC, and in Figures from 7.62(a) to 7.67(b) for the ESMC.

For each group of experiments the three-phase stator voltages, the error or the switching function (in subfigures (a)), the stator voltage amplitude, its reference value (in subfigures (b)), the field voltage v_F and its filtered value or equivalent control, u_{eq} (in the (c) subfigures) have been shown. At each experiment, the load or reference change takes place at $t = 0.5$ s and the picture at top were zoomed around this time in the bottom. In the ESMC experiments the fictitious control is also depicted. Rotor field voltage and fictitious control are quite similar because u_1 and u_2 takes high values to guarantee a bounded equivalent control and a fast response.

In general, the stator voltage amplitude is perfectly regulated, with a fast time response. In the resistive load change, the controller needs less that one stator voltage cycle to recover the reference, while in the inductive load needs between two and eight stator voltage cycles. In the reference change, the system reaches the new desired value in about two cycles. We also noticed that the time to reach the reference depend on the V_{DC} voltage value.

The actual control which lie between -1 and 1 or 0 and 1, is the DC-DC switch signal values and is equivalent to the applied field voltage (± 137.5V). Note that the control law is saturated while the reference is not achieved. It shows that the recovery time does not depend on the control algorithm. It depends on the actual V_{DC} voltage value. The filtered value or equivalent control achieves a new average value at the steady state. As it can be seen, the commutation (sliding mode) is lost for a small period when the reference voltage or the load changes. However it recovers fastly, and the equivalent control returns into the operation strip ($-V_{DC} < u_{eq} < V_{DC}$).

The CSMC and NSMC behavior are very similar. The main difference is presented in the switching function which in the NSMC oscillates more than in the CSMC. The DSMC does not work appropriately in some cases where the three-phase stator voltages are distorted which is not desirable (Figure 7.60(a)) or definitively cannot regulate the stator voltage amplitude (Figures 7.59(a) and 7.56(a)). Then, the stability of the DSMC can be guarantee in a limited space. The ESMC regulates the stator voltage amplitude but is slow compared to the other controllers, it also results in a bit distorted waves when the generator is without load (Figures 7.62(a) and 7.64(a)).

The switching function oscillates around zero and the consequent chattering phenomenon is just a little bit appreciated in simulations due to the high value of the switching frequency. When the load is inductive, the consequent chattering phenomenon diminishes because the inductive load acts as a filter. The chattering phenomenon affects more the DSMC and the ESMC algorithms. In the DSMC scheme, the switching surface remains near to zero by the absence of a proportional action. In the experimental test, the switching function oscillates around zero but, the consequent chattering phenomenon is nearly not reflected due to the minimum sampling time of the digital to analog converter.

The table 7.4 shows a comparison of the different controllers, assigning from the worst to the best, from zero to ten points. In this table ten points is given to the controller if it accomplished the desired behavior, and if the punctuation is lower it means that its behavior is not as desirable as we expect. For this comparison some design, performance and implementation aspects were taken into account.

The stability of the CSMC algorithm is theoretical guaranteed with a deeper analysis respect to each other, then we pointed it with eight points. In the PI, NSMC and ESMC a local stability was guaranteed, then their have seven points. The DSMC theoretical has local stability but the experimental results show that the system cannot be stabilized in some scenarios if so it is pointed with four points.

The convergence speed of the PI, CSMC and NSMC is quite similar. As an example, Figures 7.40(a), 7.47(a) and 7.53(a) show that each controller reaches the desired operation point in about six cycles. It is a well closed loop time constant, because it depends on the DC voltage, then we marked them with ten points in the convergence speed aspect. The ESMC stabilization in the same scenario can be observed in Figure 7.65(a). It takes about eight cycles, two more than the previous one, which is no desirable, and we assigned it with seven. The DSMC does not reach the references (Figure 7.59(a)), then it receive three.

The computation time that needs each algorithm in the DSP is 6.42μs, 4.08μs, 5.88μs, 5.16μs,5.56μs for the PI, CSMC, NSMC, DSMC and ESMC, respectively. Then, given ten points to the fastest, and let down the punctuation proportional as the computation time increments, we assigned each controller with six, ten, six, nine and eight points, respectively. The computation time is directly related to the number of operations needed for calculate each control law. For this reason, the same points are assigned to each controller for the required computation.

The directness implementation depends on the number of equations that must be programmed into the DSP. The CSMC just require the switching surface sign, and some additions and products, becoming the easiest for implementing and it is marked with ten. The DSMC and ESMC also need some additions and an integration which in discrete time implementation is an addition, and are also pointed with ten. The PI and NSMC need additionally a square root computation in order to obtain the stator voltage, then they take eight points.

The CSMC, DSMC and ESMC do not need any gain tuning, then each one received the maximum mark, while the PI and NSMC need to tune the proportional and integral terms, then are good qualified.

Theoretically, the CSMC, DSMC and ESMC must be robust to any load and parameter variation, but the experimental results show that actually the CSMC presents the expected behavior and takes ten points. The DSMC does not work as we expected, because some times it does not reach the desired output or becomes unstable (see Figures 7.59(a) and 7.56(a)), then it is discarded and pointed with one. The ESMC is robust in some situations, but in some others its slower response gives distorted waves as it can be observed in Figures 7.62(a) and 7.64(a), then, it is pointed with seven points. The PI and NSMC present a robust performance, but it is known that the proportional-integral tuning depends on the parameters, which we assigned eight points.

The resulting average of table 7.4, shows that the CSMC is the best algorithm, but the NSMC, ESMC and PI algorithms can also be used for losing just a little of performance. The DSMC is the worst as the simulation and experimental results shown.

	PI	CSMC	NSMC	DSMC	ESMC
Stability guaranteed	7	8	7	4	7
Convergence speed	10	10	10	3	7
Robustness	8	10	8	1	7
Easy tunning	8	10	8	10	10
Direct implementation	7	10	7	10	10
Required computation	6	10	6	9	8
Computation time	6	10	6	9	8
Average	7.42	9.71	7.42	6.57	8.14

Table 7.4: Comparison between the designed controllers presented in this Thesis.

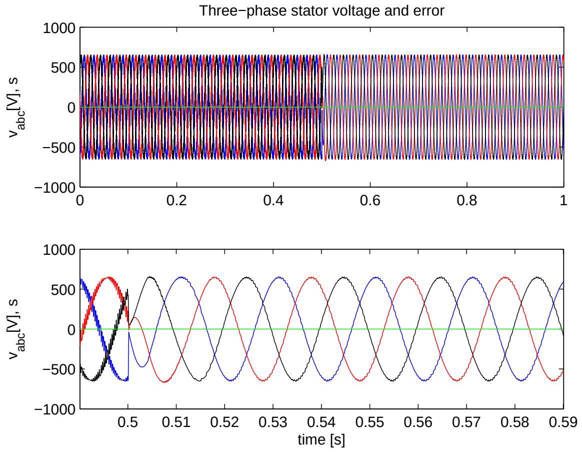

(a) three-phase stator voltages, v_s, and error, e.

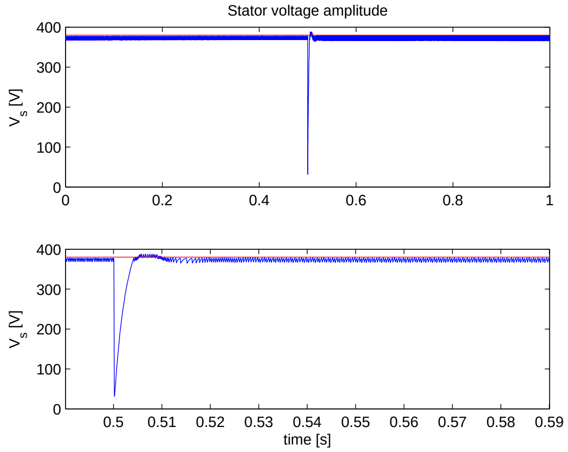

(b) stator voltage amplitude, V, and its reference V_{ref}.

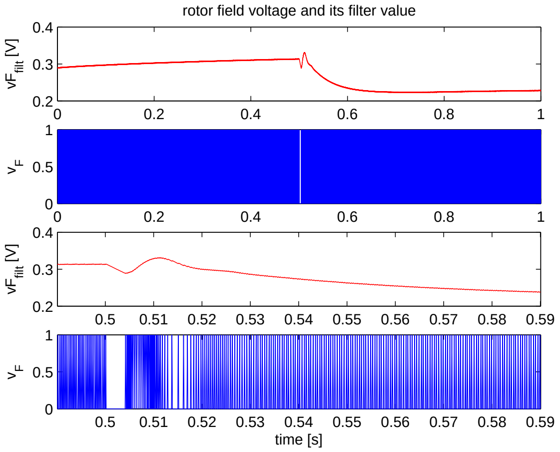

(c) switching control policy, v_F, and its filtered value.

Figure 7.9: Simulation results, PI: Load change from no load to half load.

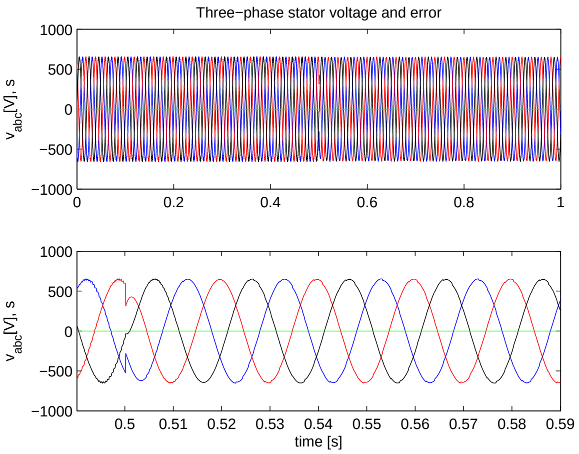

(a) three-phase stator voltages, v_s, and error, e.

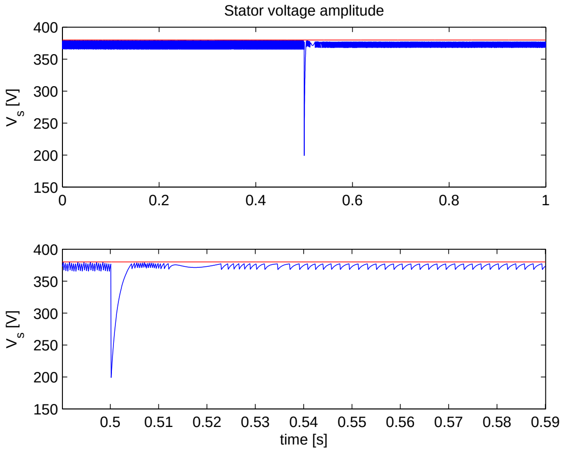

(b) stator voltage amplitude, V, and its reference V_{ref}.

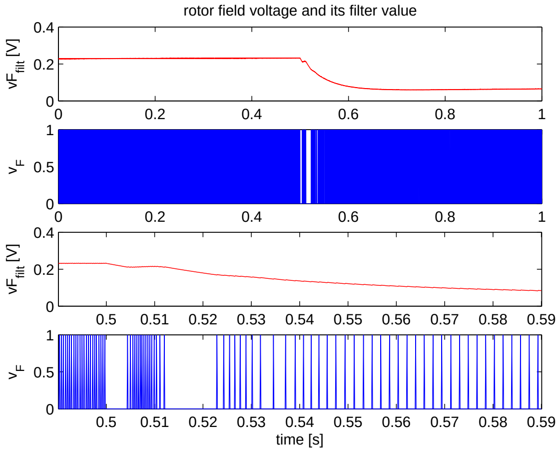

(c) switching control policy, v_F, and its filtered value

Figure 7.10: Simulation results, PI: Load change from half load to full load.

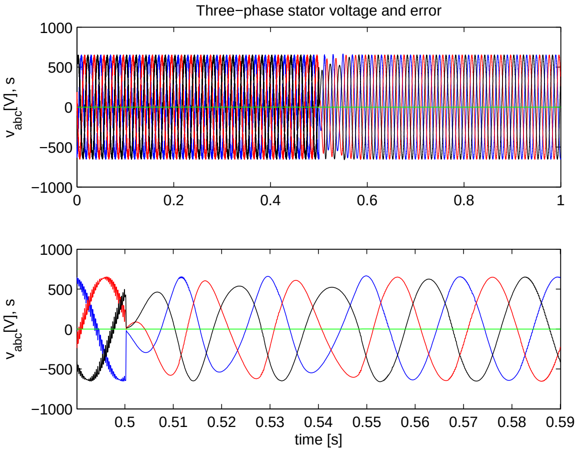

(a) three-phase stator voltages, v_s, and error, e.

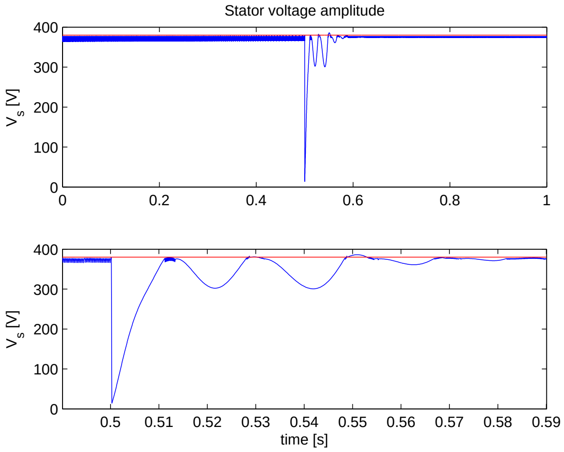

(b) stator voltage amplitude, V, and its reference V_{ref}.

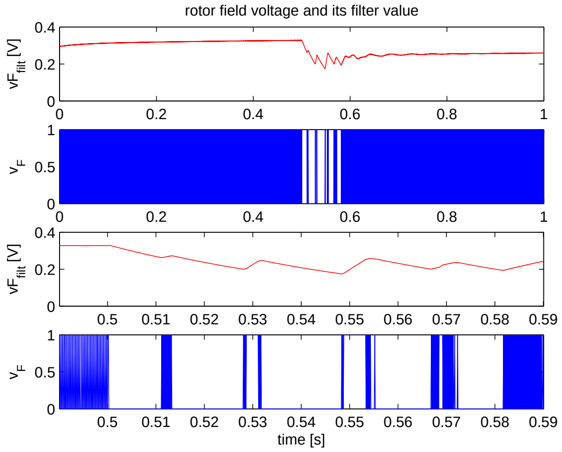

(c) switching control policy, v_F, and its filtered value.

Figure 7.11: Simulation results, PI: Load change from no load to IM connection.

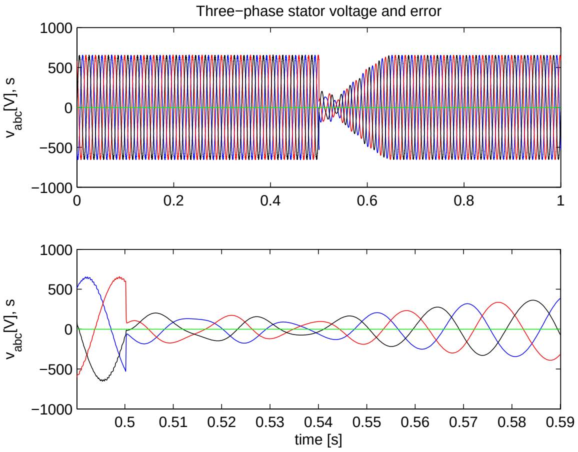

(a) three-phase stator voltages, v_s, and error, e.

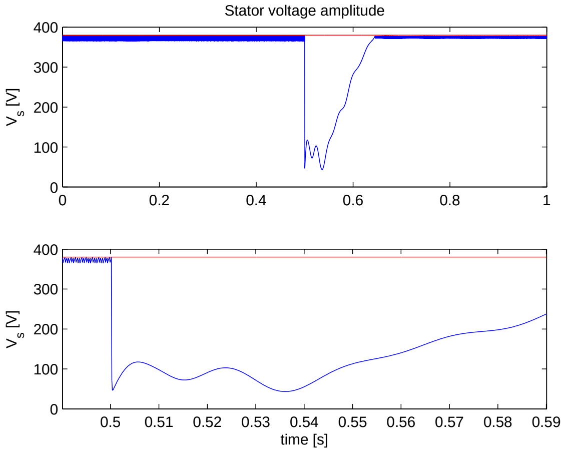

(b) stator voltage amplitude, V, and its reference V_{ref}.

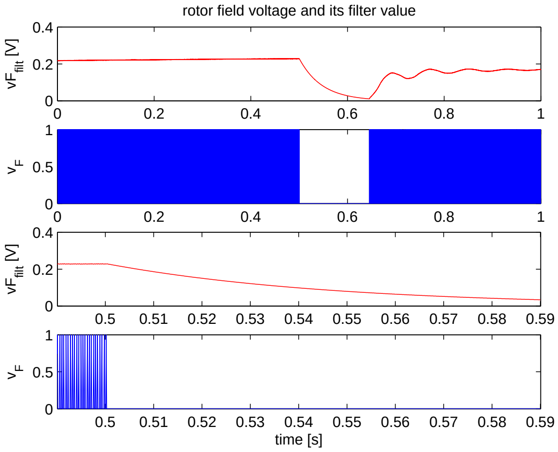

(c) switching control policy, v_F, and its filtered value.

Figure 7.12: Simulation results, PI: Load change from half load to half load and IM connection.

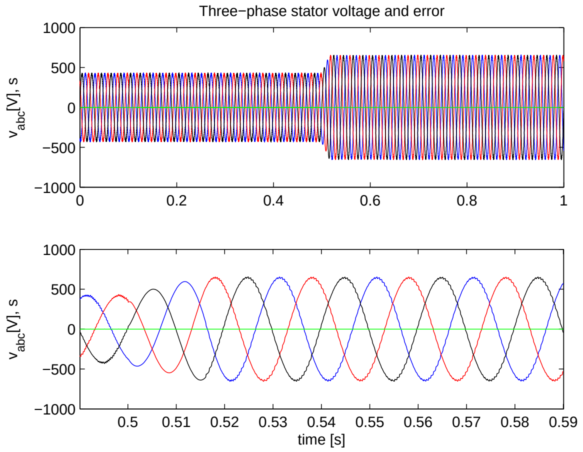

(a) three-phase stator voltages, v_s, and error, e.

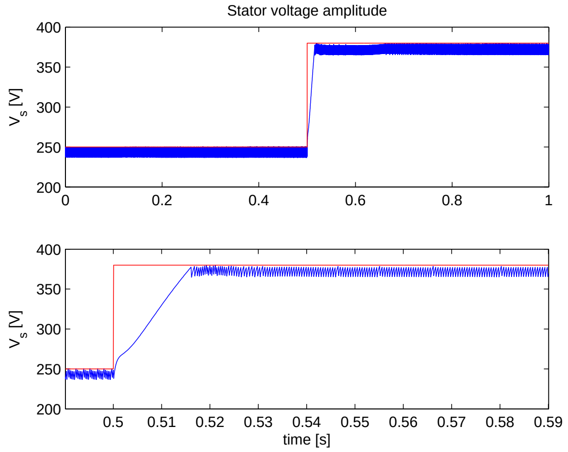

(b) stator voltage amplitude, V, and its reference V_{ref}.

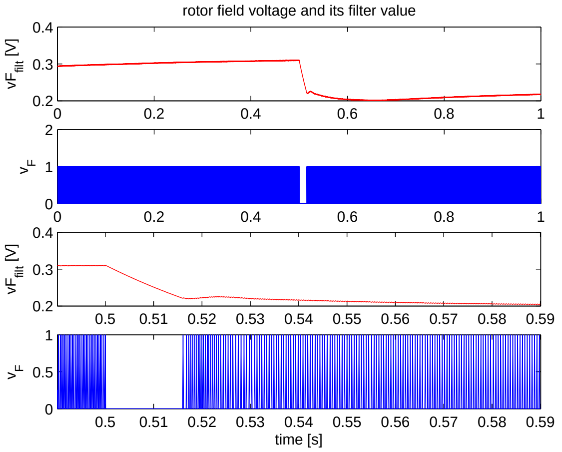

(c) switching control policy, v_F, and its filtered value.

Figure 7.13: Simulation results, PI: Voltage reference change from 250Vrms to 380Vrms with half load.

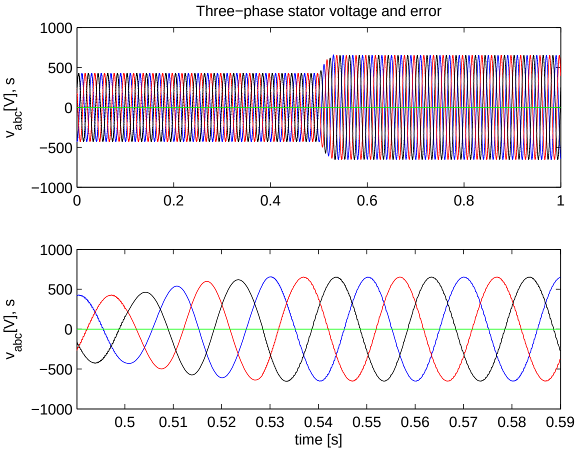

(a) three-phase stator voltages, v_s, and error, e.

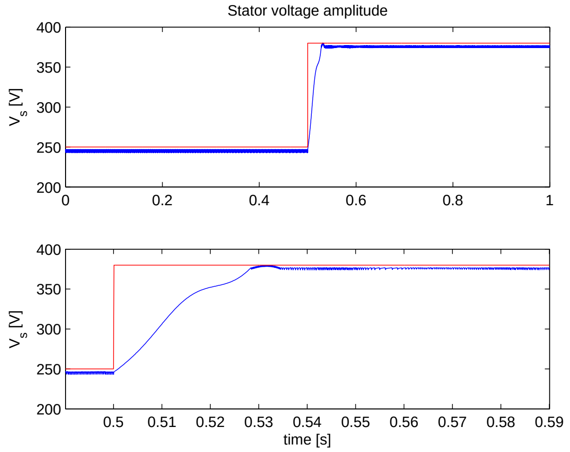

(b) stator voltage amplitude, V, and its reference V_{ref}.

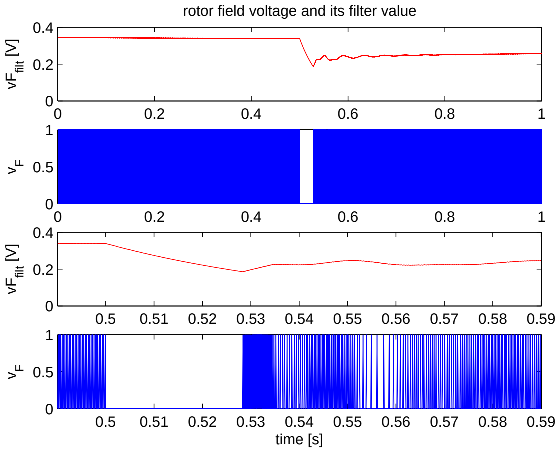

(c) switching control policy, v_F, and its filtered value.

Figure 7.14: Simulation results, PI: Voltage reference change from 250Vrms to 380Vrms with inductive load.

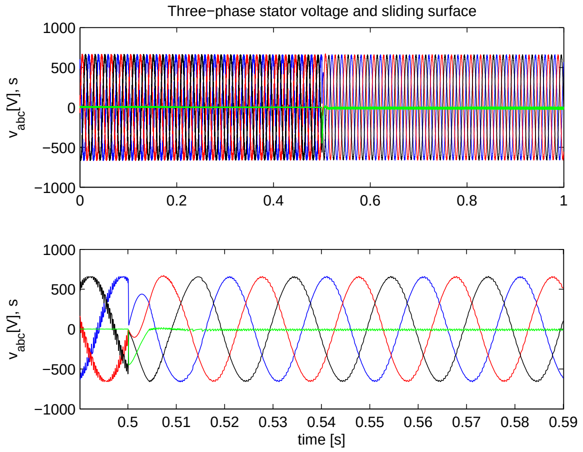

(a) three-phase stator voltages, v_s, and switching function, s.

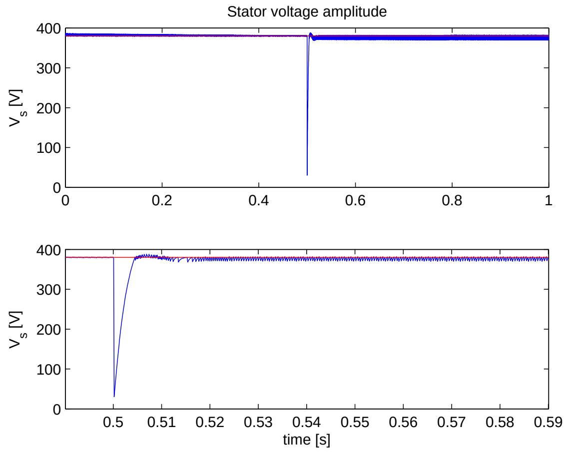

(b) stator voltage amplitude, V, and its reference V_{ref}.

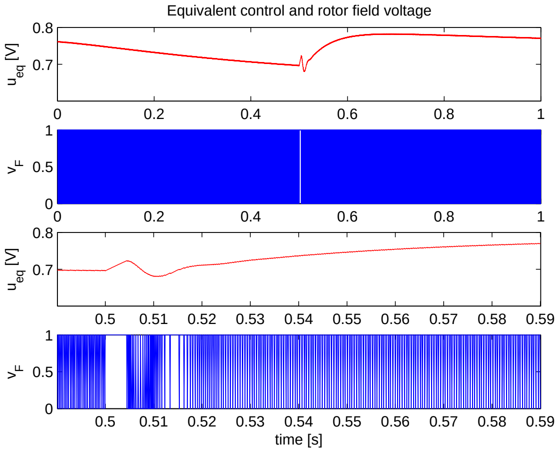

(c) switching control policy, v_F, and equivalent control, u_{eq}.

Figure 7.15: Simulation results, CSMC: Load change from no load to half load.

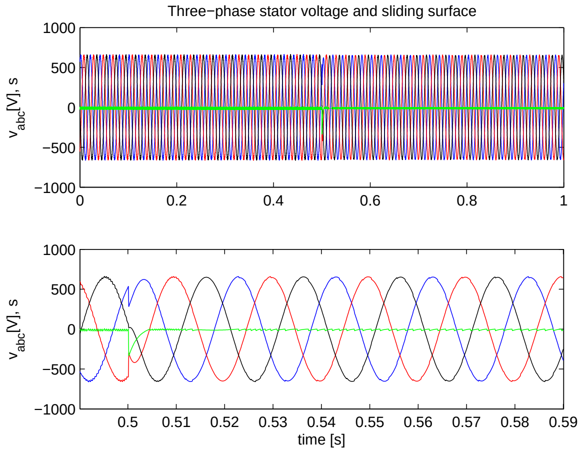

(a) three-phase stator voltages, v_s, and switching function, s.

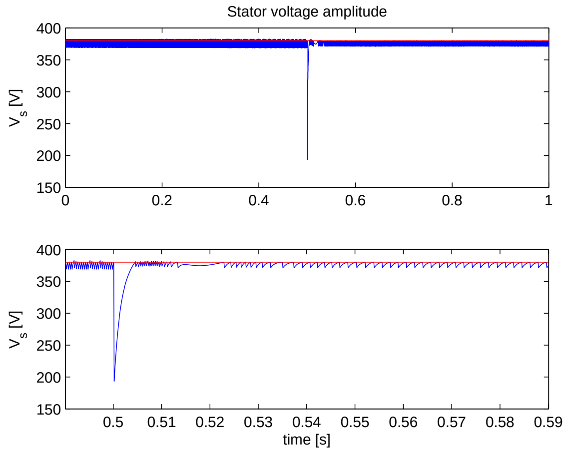

(b) stator voltage amplitude, V, and its reference V_{ref}.

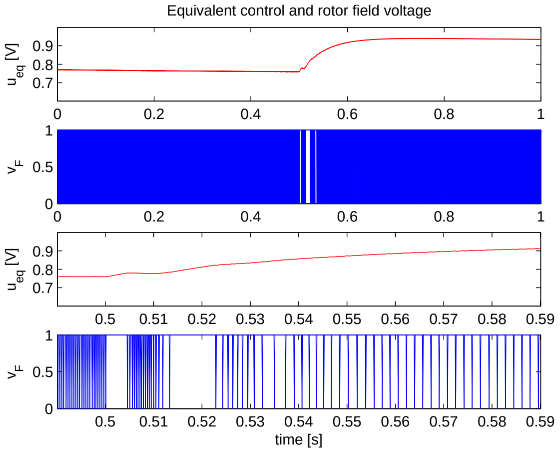

(c) switching control policy, v_F, and equivalent control, u_{eq}.

Figure 7.16: Simulation results, CSMC: Load change from half load to full load.

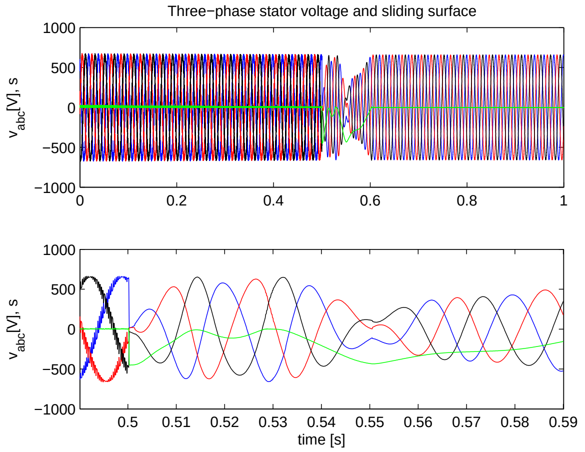

(a) three-phase stator voltages, v_s, and switching function, s.

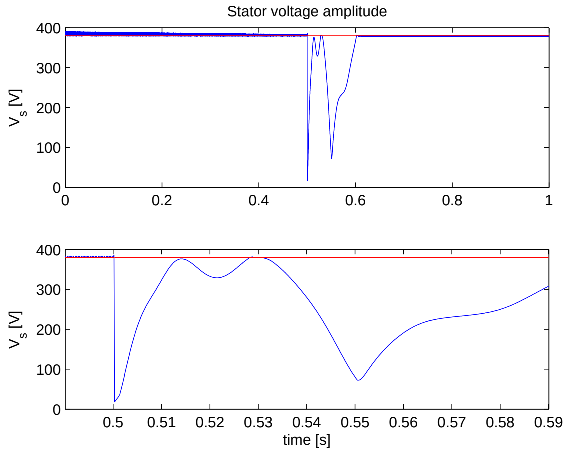

(b) stator voltage amplitude, V, and its reference V_{ref}.

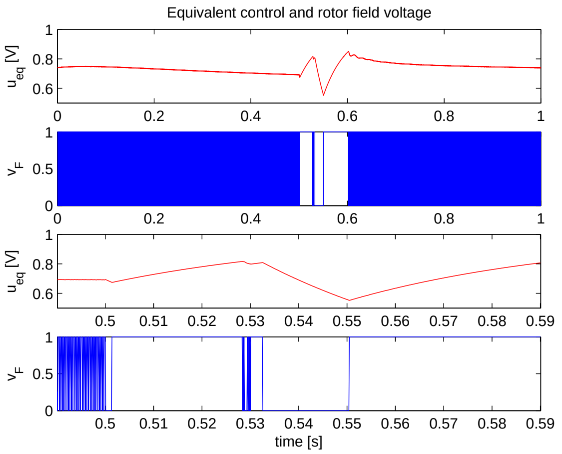

(c) switching control policy, v_F, and equivalent control, u_{eq}.

Figure 7.17: Simulation results, CSMC: Load change from no load to IM connection.

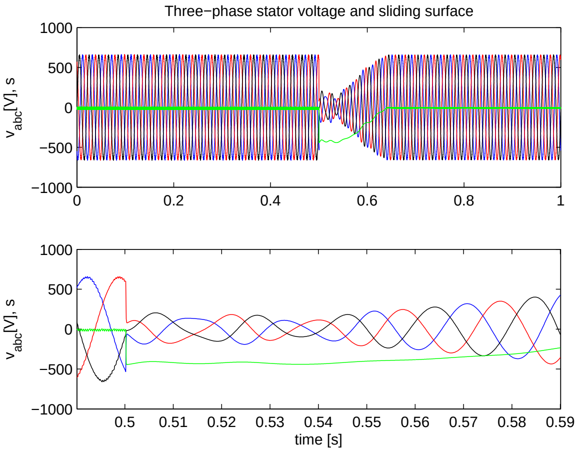

(a) three-phase stator voltages, v_s, and switching function, s.

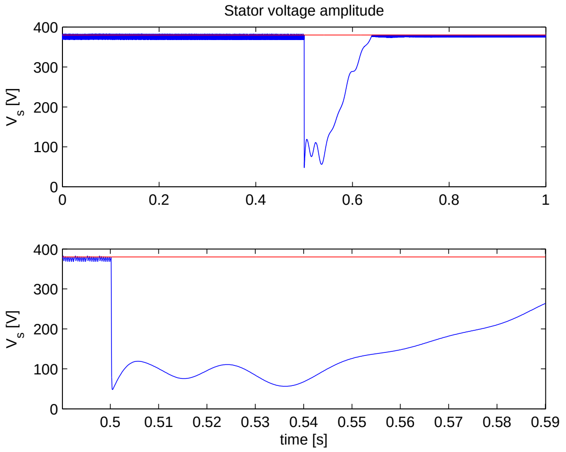

(b) stator voltage amplitude, V, and its reference V_{ref}.

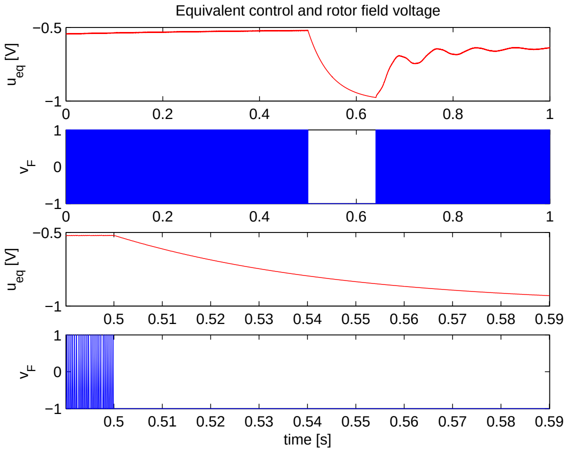

(c) switching control policy, v_F, and equivalent control, u_{eq}.

Figure 7.18: Simulation results, CSMC: Load change from half load to half load and IM connection.

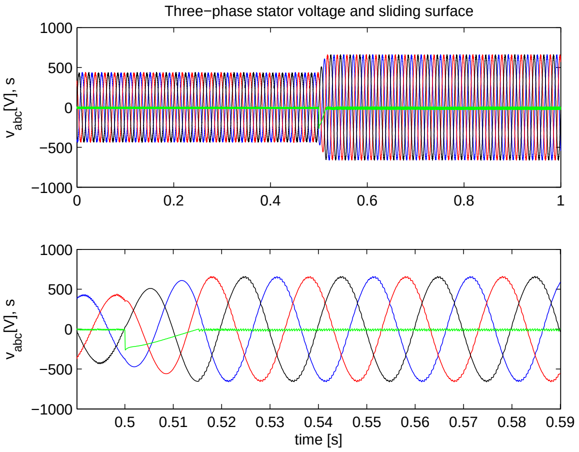

(a) three-phase stator voltages, v_s, and switching function, s.

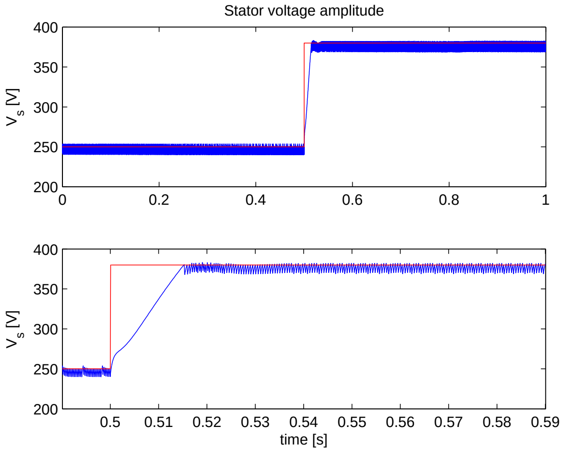

(b) stator voltage amplitude, V, and its reference V_{ref}.

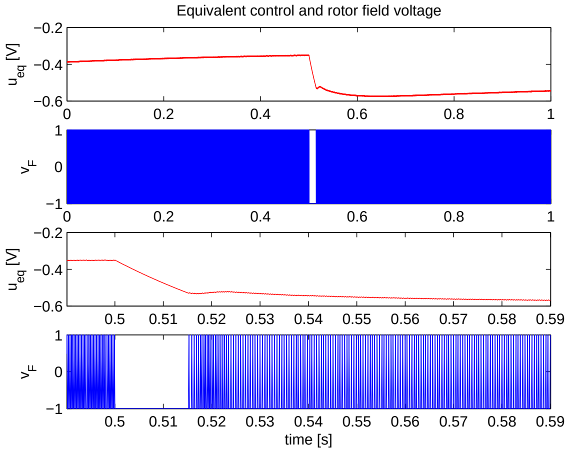

(c) switching control policy, v_F, and equivalent control, u_{eq}.

Figure 7.19: Simulation results, CSMC: Voltage reference change from 250Vrms to 380Vrms with half load.

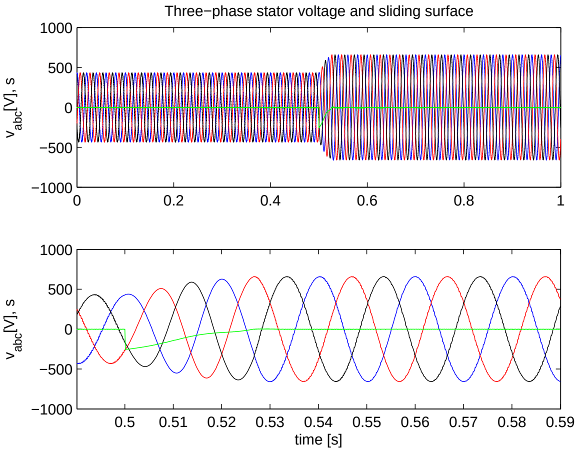

(a) three-phase stator voltages, v_s, and switching function, s.

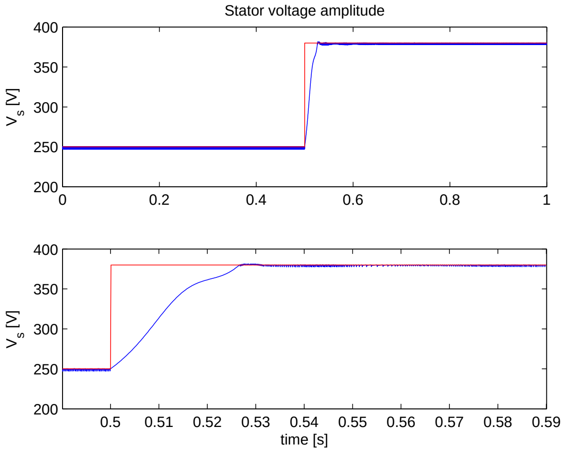

(b) stator voltage amplitude, V, and its reference V_{ref}.

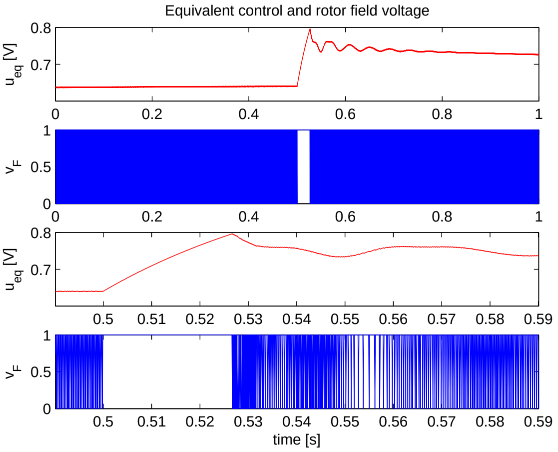

(c) switching control policy, v_F, and equivalent control, u_{eq}.

Figure 7.20: Simulation results, CSMC: Voltage reference change from 250Vrms to 380Vrms with inductive load.

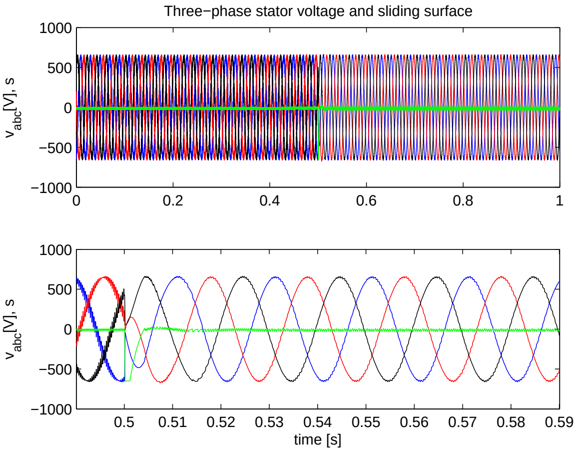

(a) three-phase stator voltages, v_s, and switching function, s.

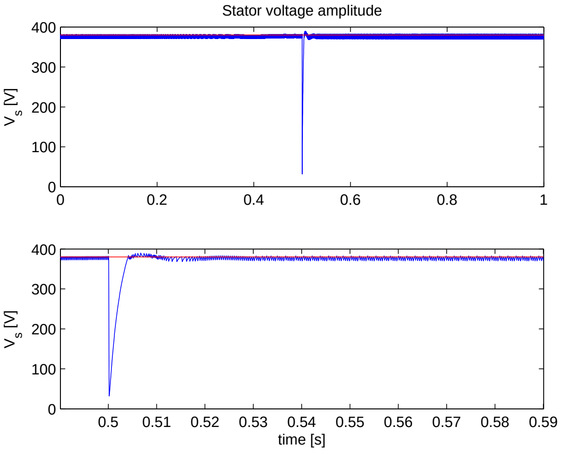

(b) stator voltage amplitude, V, and its reference V_{ref}.

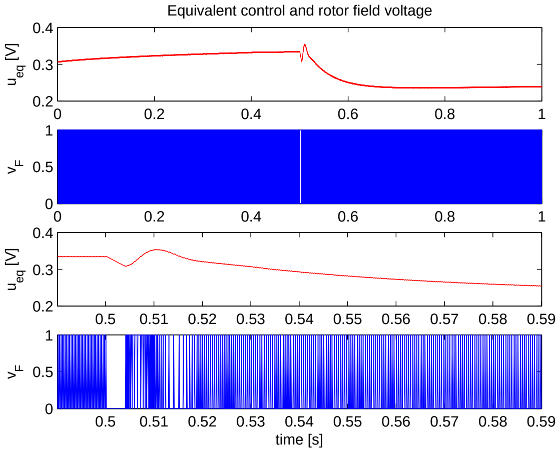

(c) switching control policy, v_F, and equivalent control, u_{eq}.

Figure 7.21: Simulation results, NSMC: Load change from no load to half load.

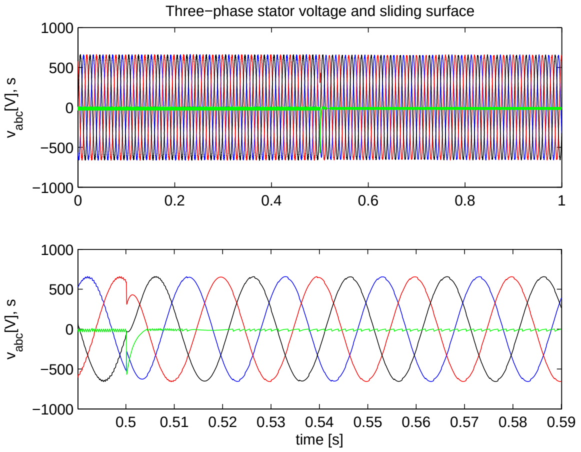

(a) three-phase stator voltages, v_s, and switching function, s.

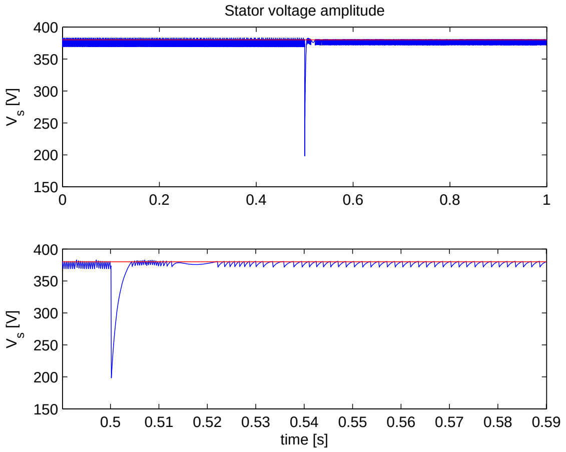

(b) stator voltage amplitude, V, and its reference V_{ref}.

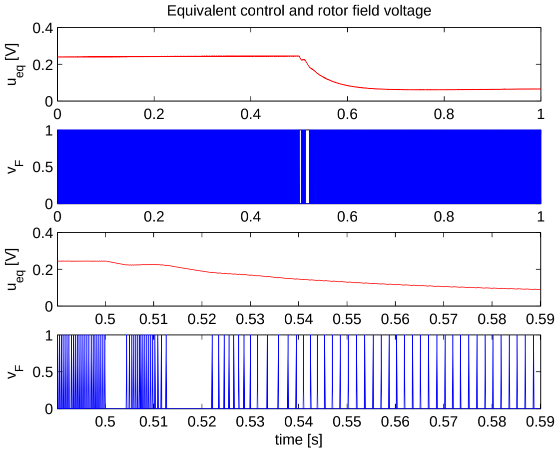

(c) switching control policy, v_F, and equivalent control, u_{eq}.

Figure 7.22: Simulation results, NSMC: Load change from half load to full load.

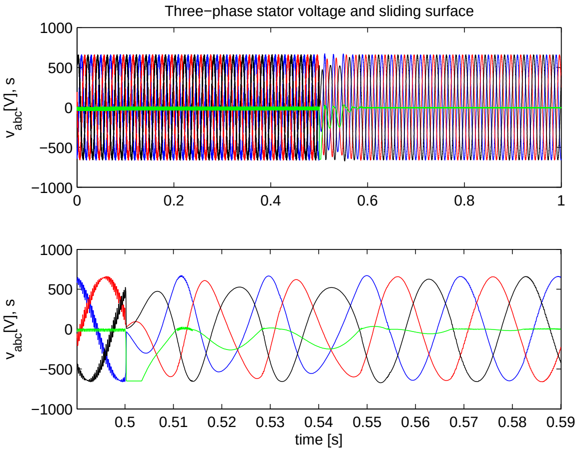

(a) three-phase stator voltages, v_s, and switching function, s.

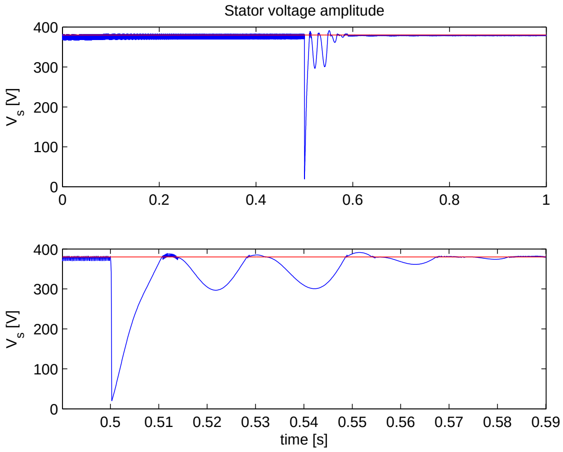

(b) stator voltage amplitude, V, and its reference V_{ref}.

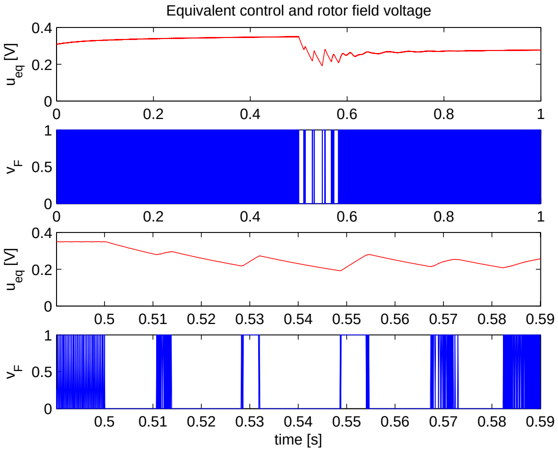

(c) switching control policy, v_F, and equivalent control, u_{eq}.

Figure 7.23: Simulation results, NSMC: Load change from no load to IM connection.

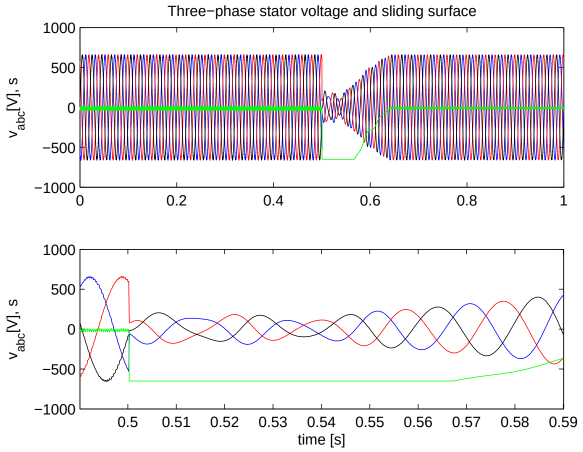

(a) three-phase stator voltages, v_s, and switching function, s.

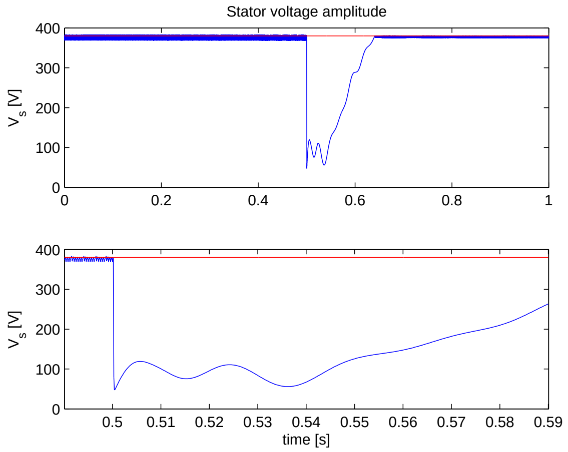

(b) stator voltage amplitude, V, and its reference V_{ref}.

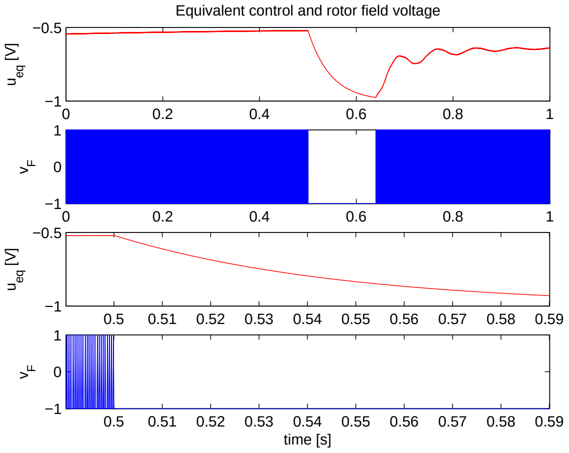

(c) switching control policy, v_F, and equivalent control, u_{eq}.

Figure 7.24: Simulation results, NSMC: Load change from half load to half load and IM connection.

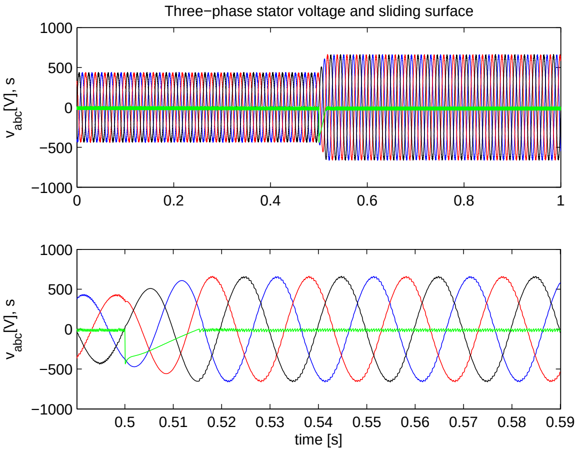

(a) three-phase stator voltages, v_s, and switching function, s.

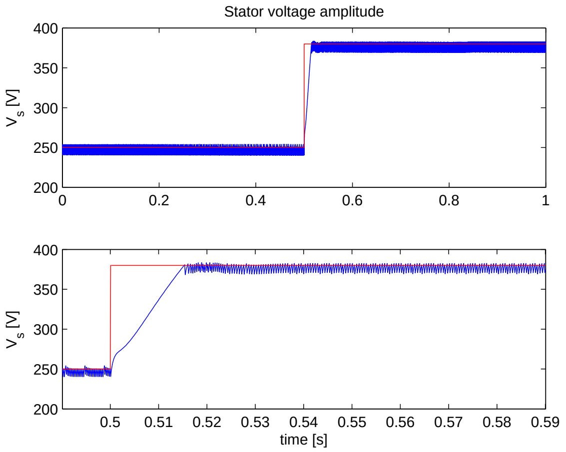

(b) stator voltage amplitude, V, and its reference V_{ref}.

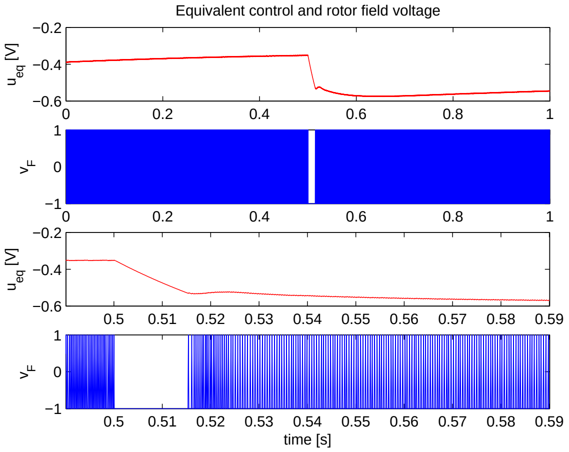

(c) switching control policy, v_F, and equivalent control, u_{eq}.

Figure 7.25: Simulation results, NSMC: Voltage reference change from 250Vrms to 380Vrms with half load.

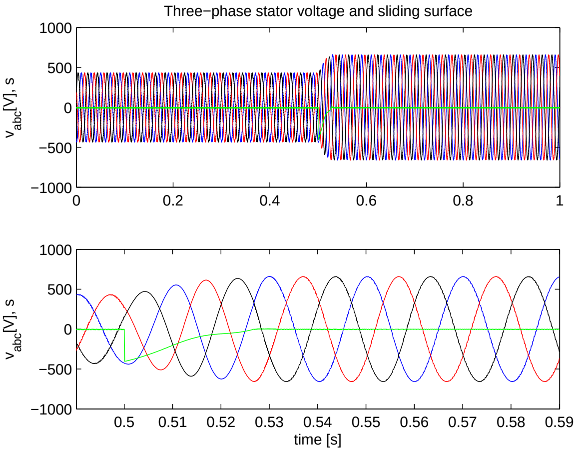

(a) three-phase stator voltages, v_s, and switching function, s.

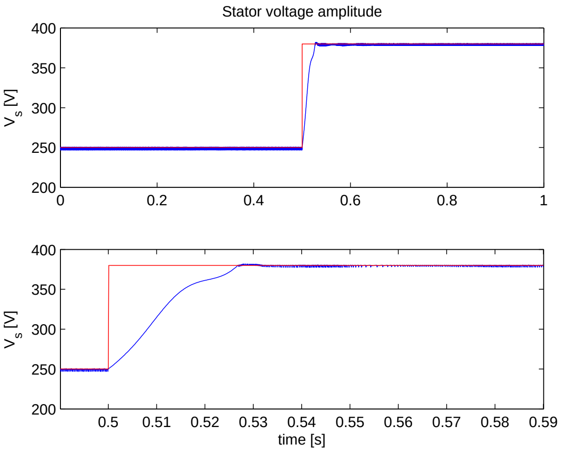

(b) stator voltage amplitude, V, and its reference V_{ref}.

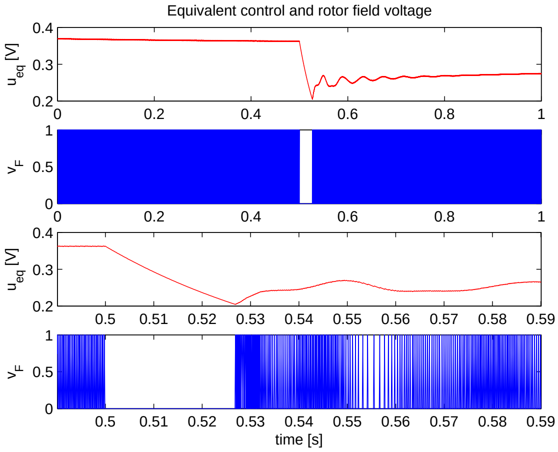

(c) switching control policy, v_F, and equivalent control, u_{eq}.

Figure 7.26: Simulation results, NSMC: Voltage reference change from 250Vrms to 380Vrms with inductive load.

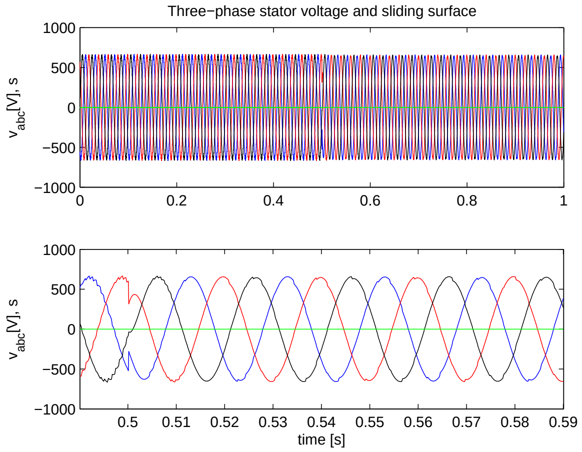

(a) three-phase stator voltages, v_s, and switching function, s.

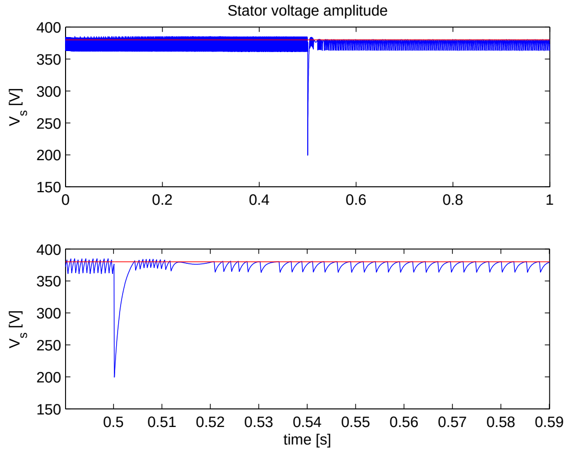

(b) stator voltage amplitude, V, and its reference V_{ref}.

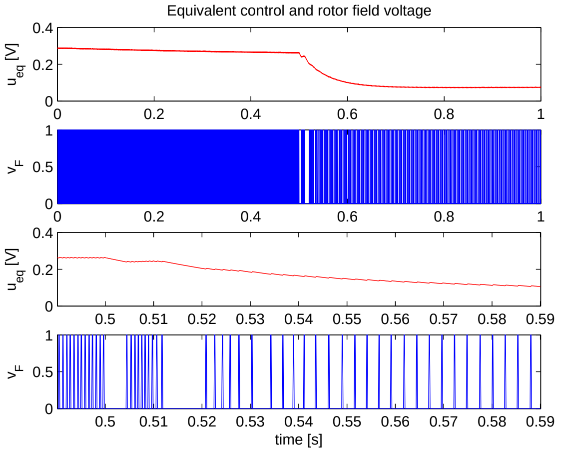

(c) switching control policy, v_F, and equivalent control, u_{eq}.

Figure 7.27: Simulation results, DSMC: Load change from half load to full load.

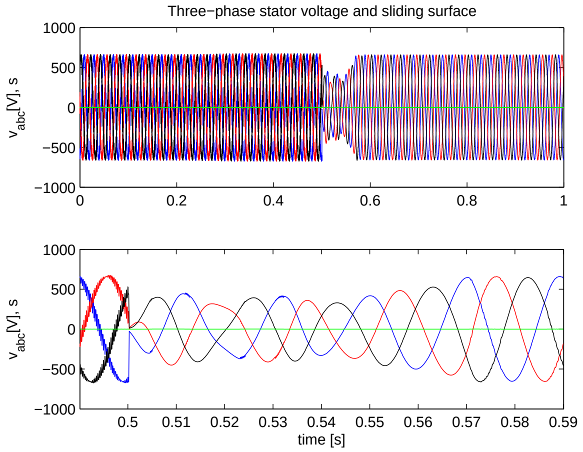

(a) three-phase stator voltages, v_s, and switching function, s.

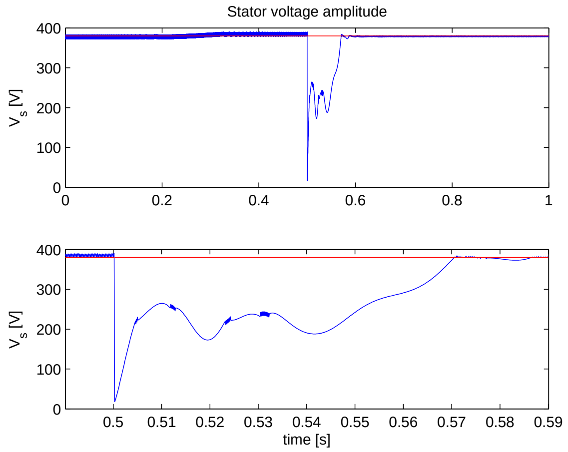

(b) stator voltage amplitude, V, and its reference V_{ref}.

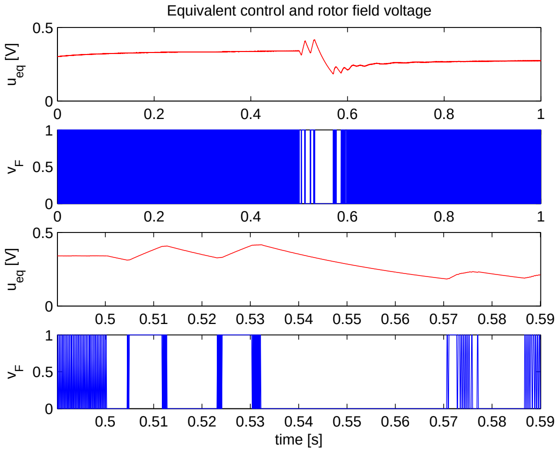

(c) switching control policy, v_F, and equivalent control, u_{eq}.

Figure 7.28: Simulation results, DSMC: Load change from no load to IM connection.

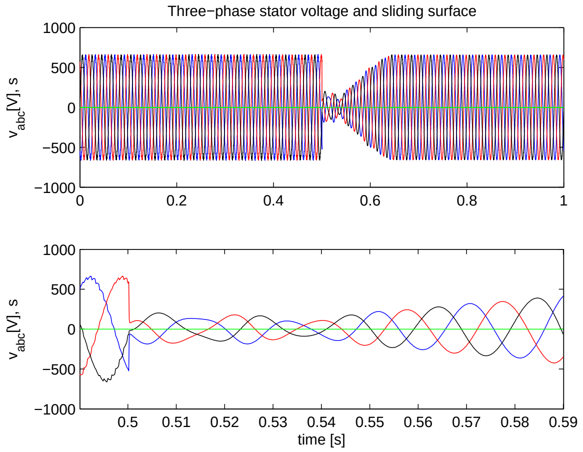

(a) three-phase stator voltages, v_s, and switching function, s.

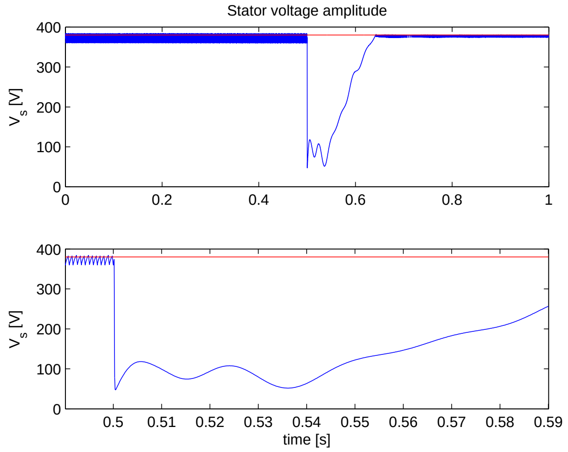

(b) stator voltage amplitude, V, and its reference V_{ref}.

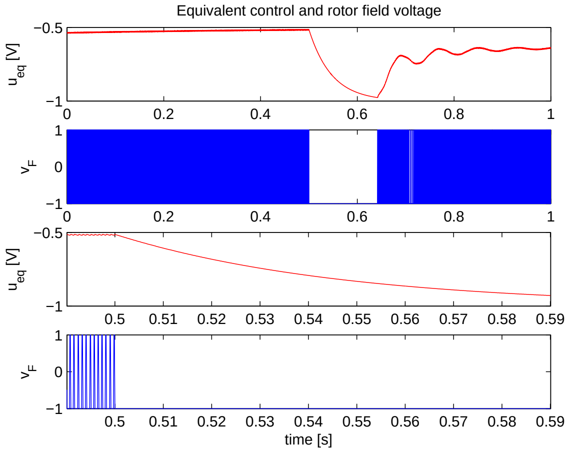

(c) switching control policy, v_F, and equivalent control, u_{eq}.

Figure 7.29: Simulation results, DSMC: Load change from half load to half load and IM connection.

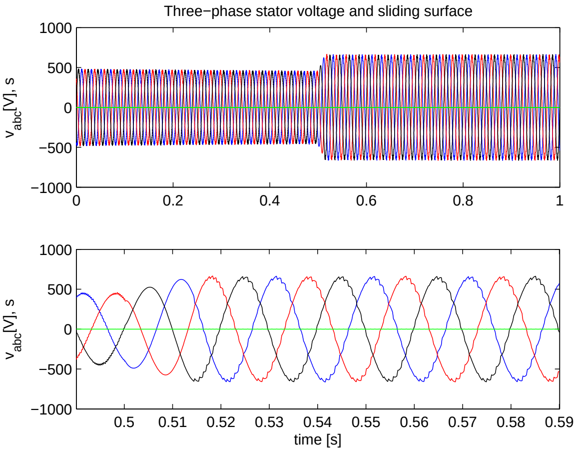

(a) three-phase stator voltages, v_s, and switching function, s.

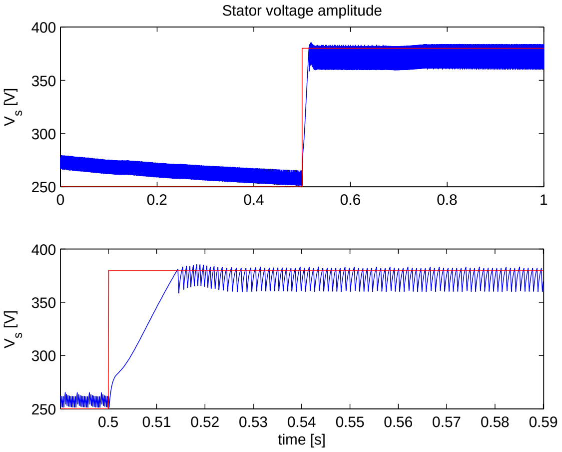

(b) stator voltage amplitude, V, and its reference V_{ref}.

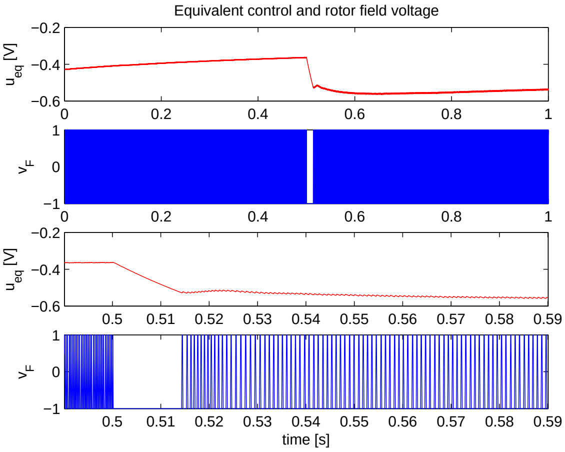

(c) switching control policy, v_F, and equivalent control, u_{eq}.

Figure 7.30: Simulation results, DSMC: Voltage reference change from 250Vrms to 380Vrms with half load.

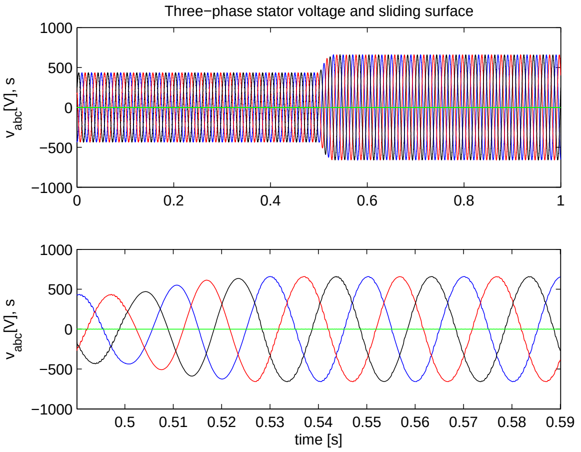

(a) three-phase stator voltages, v_s, and switching function, s.

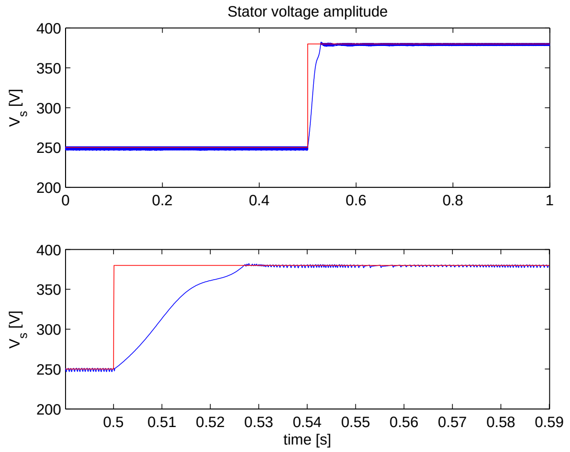

(b) stator voltage amplitude, V, and its reference V_{ref}.

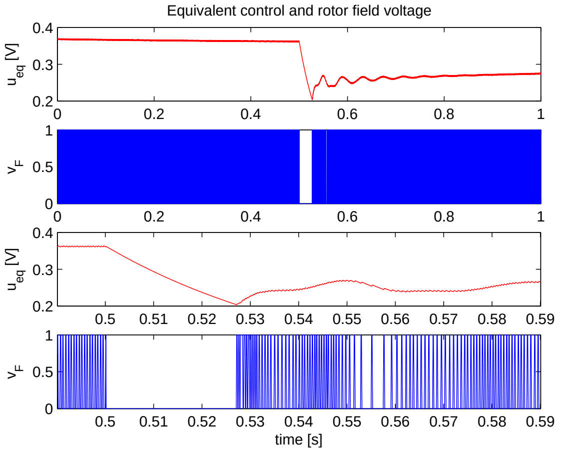

(c) switching control policy, v_F, and equivalent control, u_{eq}.

Figure 7.31: Simulation results, DSMC: Voltage reference change from 250Vrms to 380Vrms with inductive load.

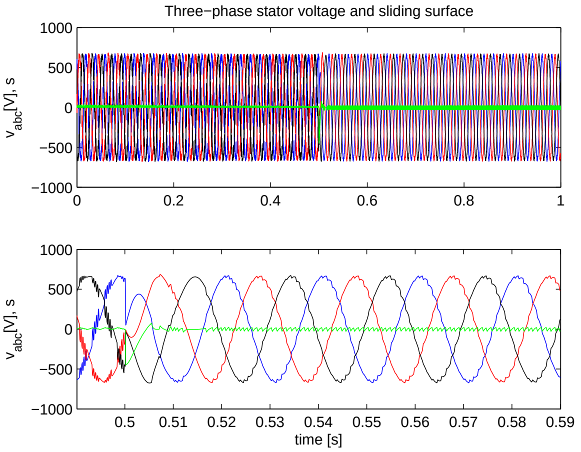

(a) three-phase stator voltages, v_s, and switching function, s.

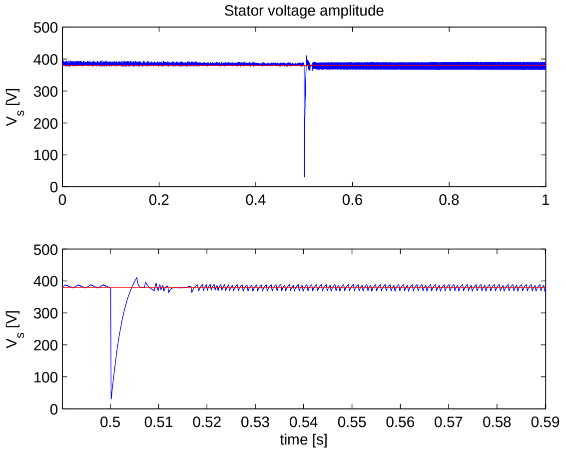

(b) stator voltage amplitude, V, and its reference V_{ref}.

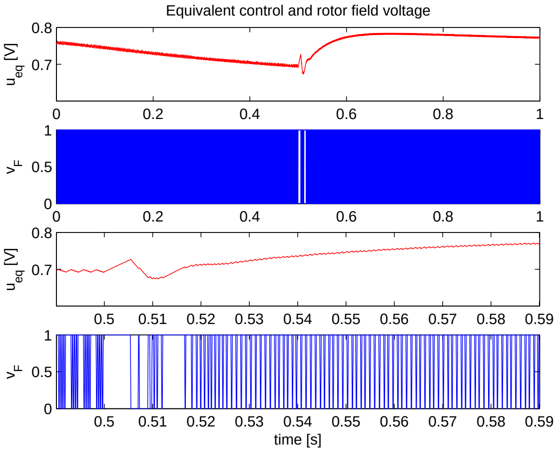

(c) switching control policy, v_F, and equivalent control, u_{eq}.

Figure 7.32: Simulation results, ESMC: Load change from no load to half load.

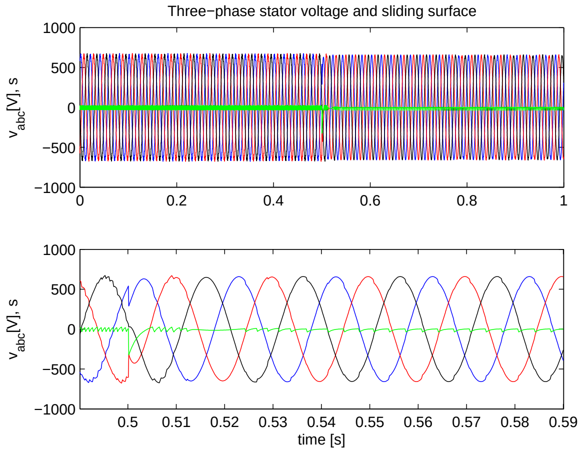

(a) three-phase stator voltages, v_s, and switching function, s.

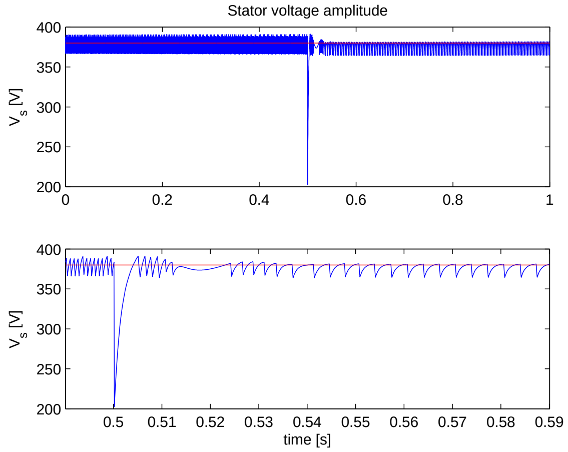

(b) stator voltage amplitude, V, and its reference V_{ref}.

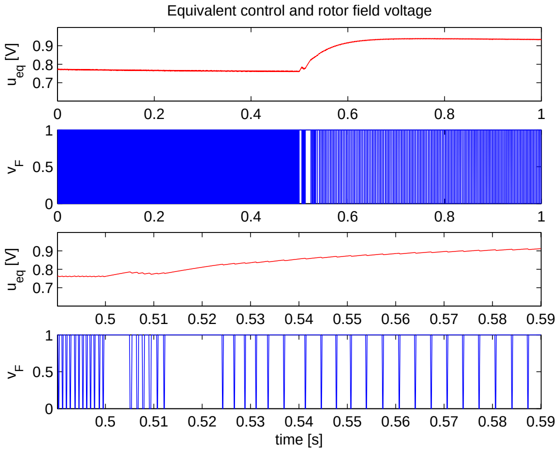

(c) switching control policy, v_F, and equivalent control, u_{eq}.

Figure 7.33: Simulation results, ESMC: Load change from half load to full load.

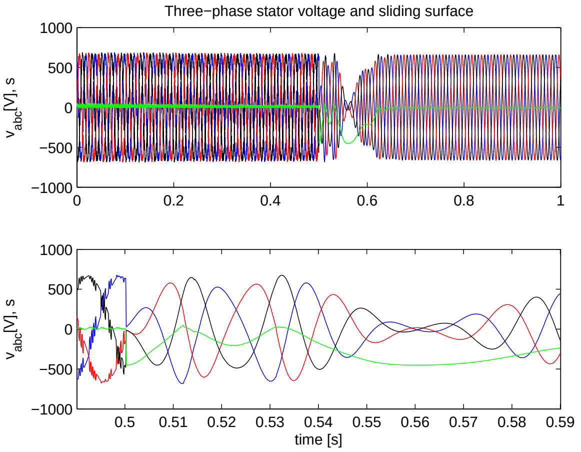

(a) three-phase stator voltages, v_s, and switching function, s.

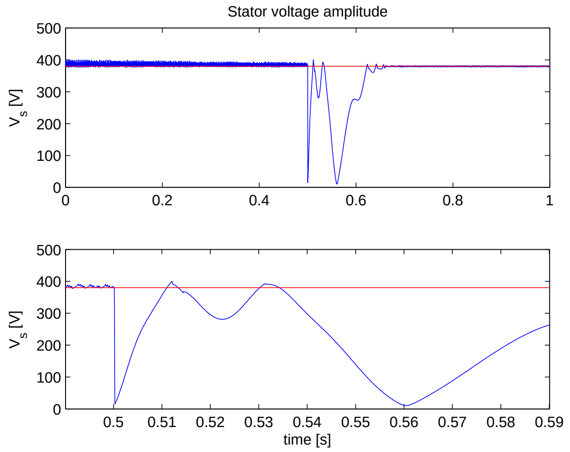

(b) stator voltage amplitude, V, and its reference V_{ref}.

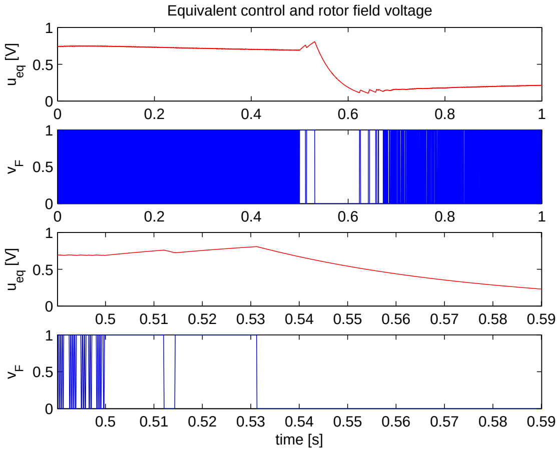

(c) switching control policy, v_F, and equivalent control, u_{eq}.

Figure 7.34: Simulation results, ESMC: Load change from no load to IM connection.

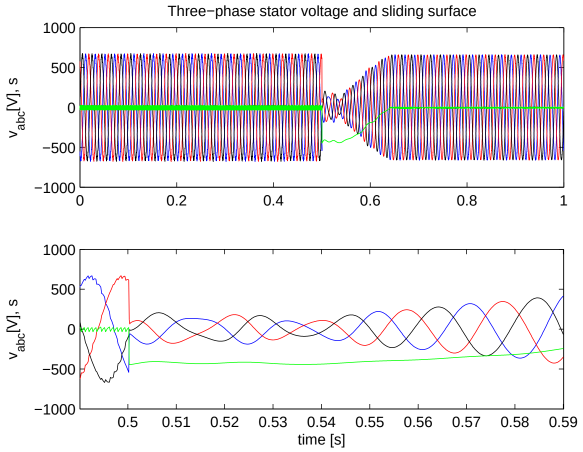

(a) three-phase stator voltages, v_s, and switching function, s.

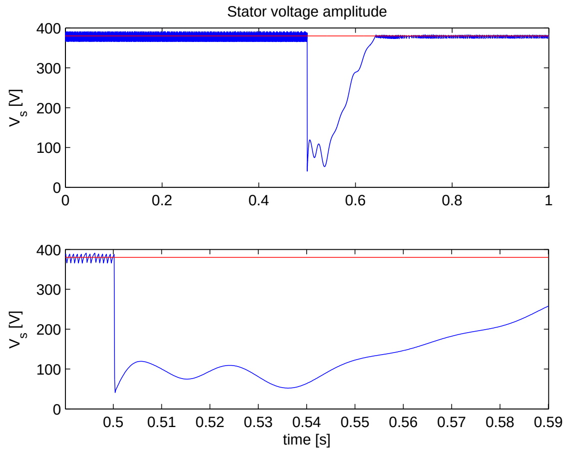

(b) stator voltage amplitude, V, and its reference V_{ref}.

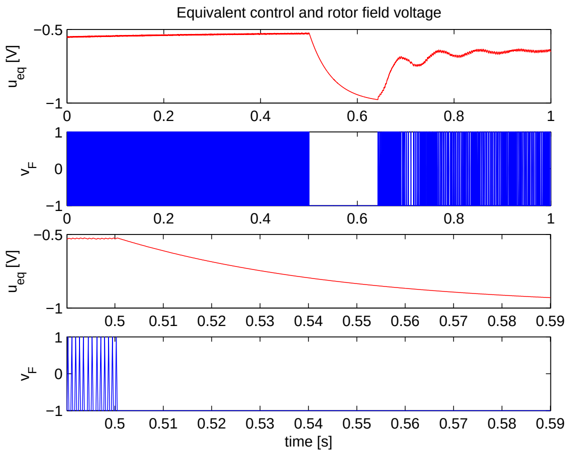

(c) switching control policy, v_F, and equivalent control, u_{eq}.

Figure 7.35: Simulation results, ESMC: Load change from half load to half load and IM connection.

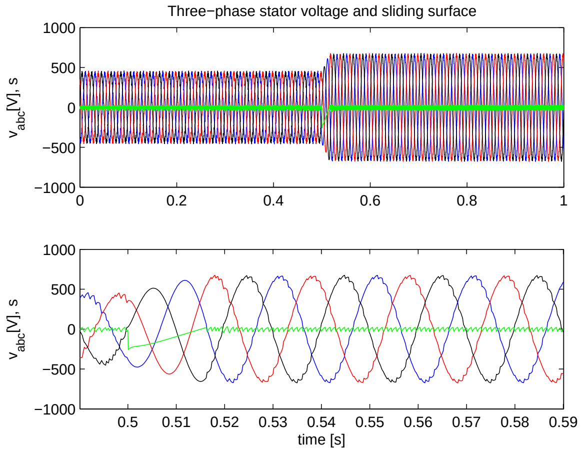

(a) three-phase stator voltages, v_s, and switching function, s.

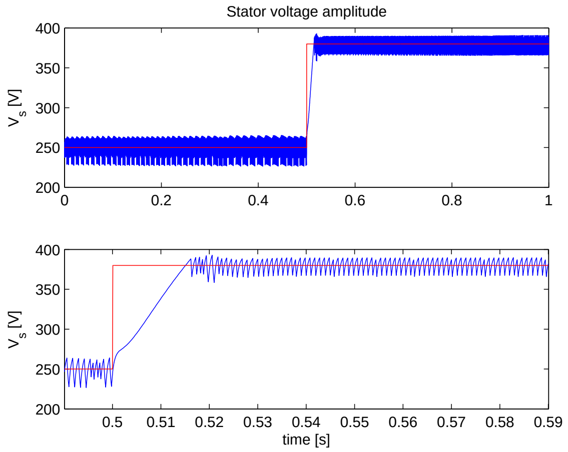

(b) stator voltage amplitude, V, and its reference V_{ref}.

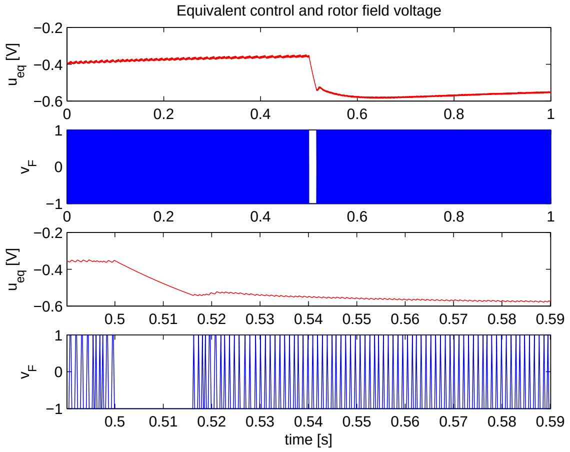

(c) switching control policy, v_F, and equivalent control, u_{eq}.

Figure 7.36: Simulation results, ESMC: Voltage reference change from 250Vrms to 380Vrms with half load.

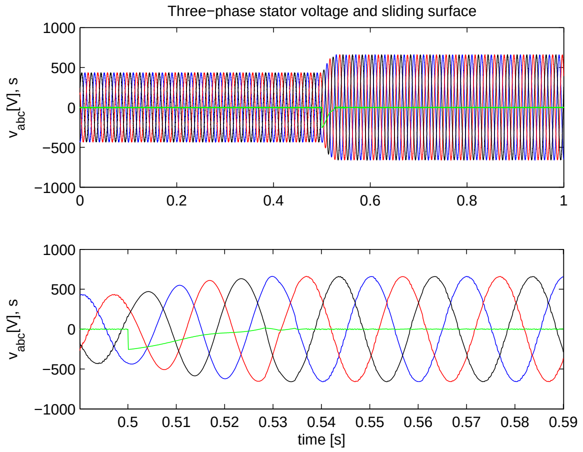

(a) three-phase stator voltages, v_s, and switching function, s.

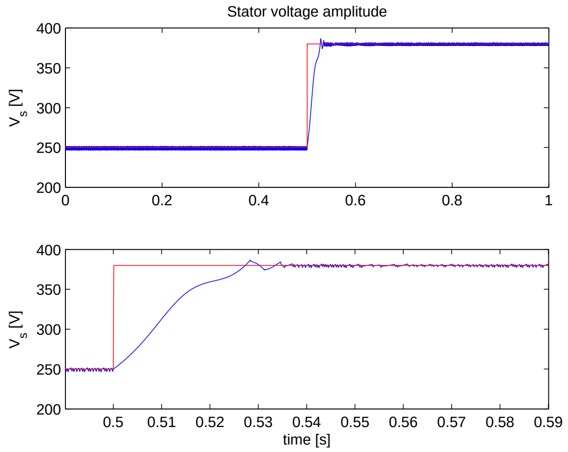

(b) stator voltage amplitude, V, and its reference V_{ref}.

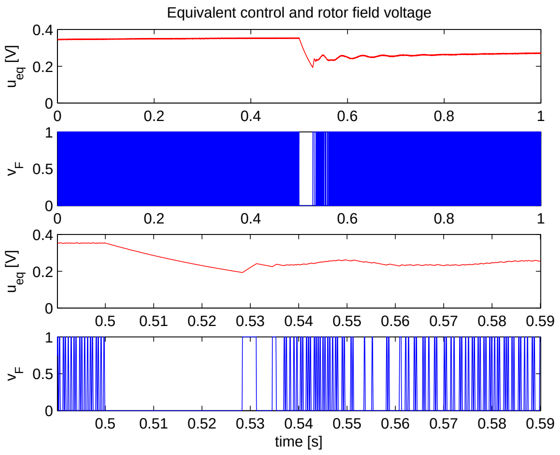

(c) switching control policy, v_F, and equivalent control, u_{eq}.

Figure 7.37: Simulation results, ESMC: Voltage reference change from 250Vrms to 380Vrms with inductive load.

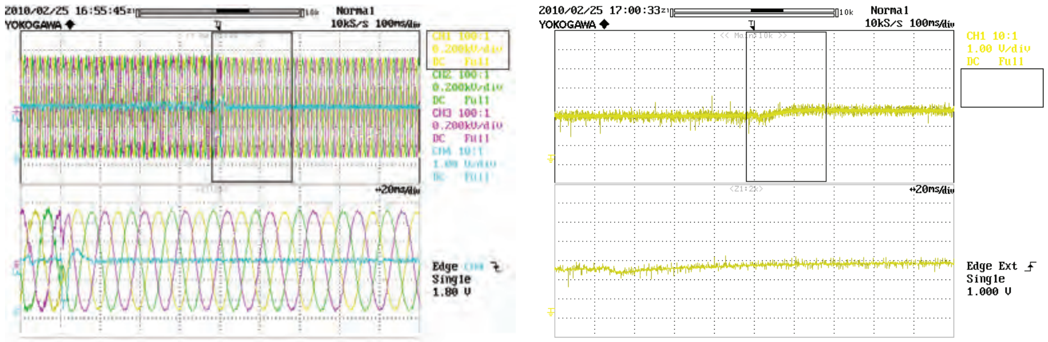

(a) three-phase stator voltages, v_s, and error, e.

(b) control policy, v_F

Figure 7.38: Experimental results, PI: Load change from no load to half load.

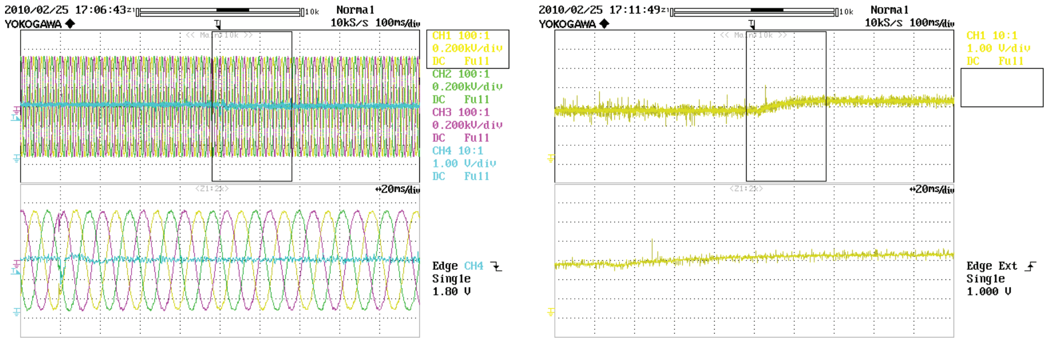

(a) three-phase stator voltages, v_s, and error, e.

(b) control policy, v_F

Figure 7.39: Experimental results, PI: Load change from half load to full load.

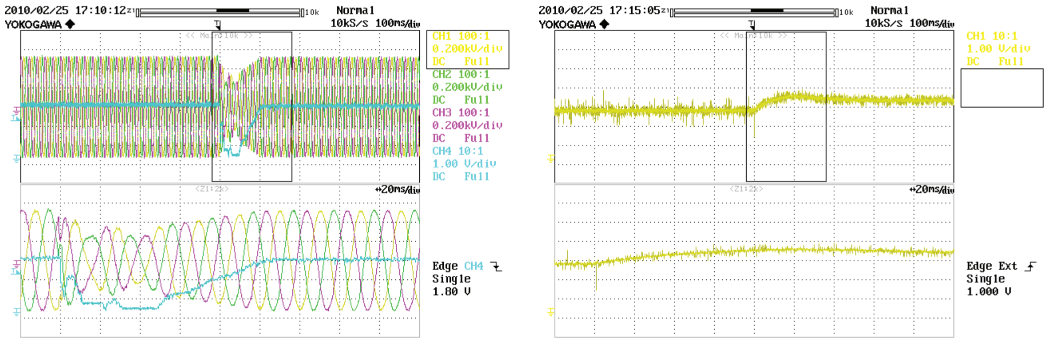

(a) three-phase stator voltages, v_s, and error, e.

(b) control policy, v_F

Figure 7.40: Experimental results, PI: Load change from half load to IM connection.

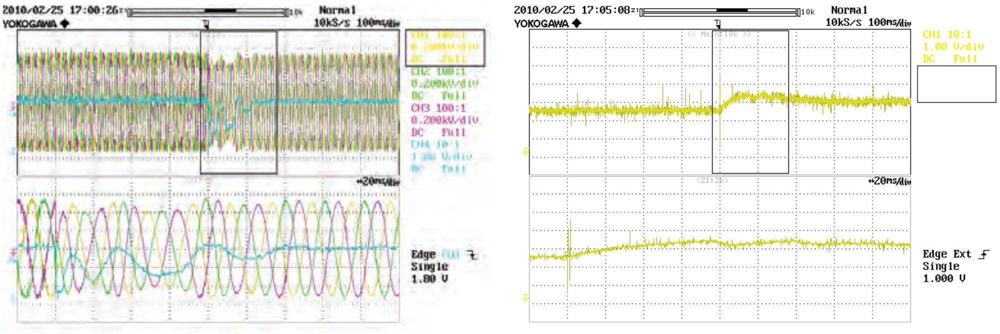

(a) three-phase stator voltages, v_s, and error, e.

(b) control policy, v_F

Figure 7.41: Experimental results, PI: Load change from no load to IM connection.

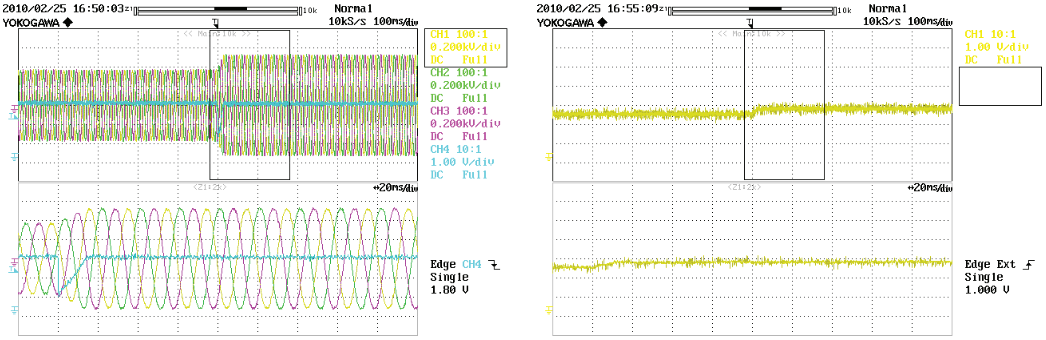

(a) three-phase stator voltages, v_s, and error, e.

(b) control policy, v_F

Figure 7.42: Experimental results, PI: Voltage reference change from 250Vrms to 380Vrms with half load.

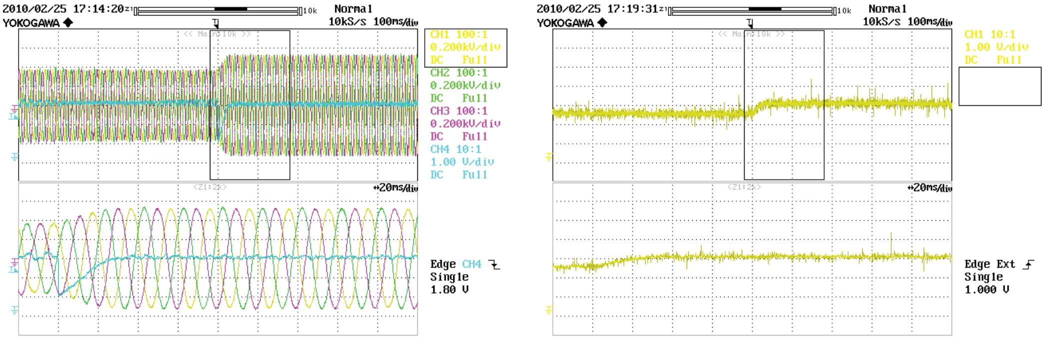

(a) three-phase stator voltages, v_s, and error, e.

(b) control policy, v_F

Figure 7.43: Experimental results, PI: Voltage reference change from 250Vrms to 380Vrms with inductive load.

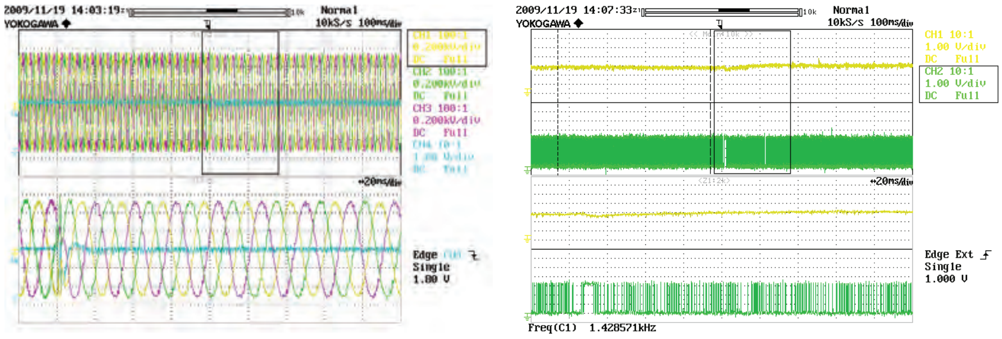

(a) three-phase stator voltages, v_s, and switching function, s.

(b) switching control policy, v_F, and equivalent control, u_{eq}

Figure 7.44: Experimental results, CSMC: Load change from no load to half load.

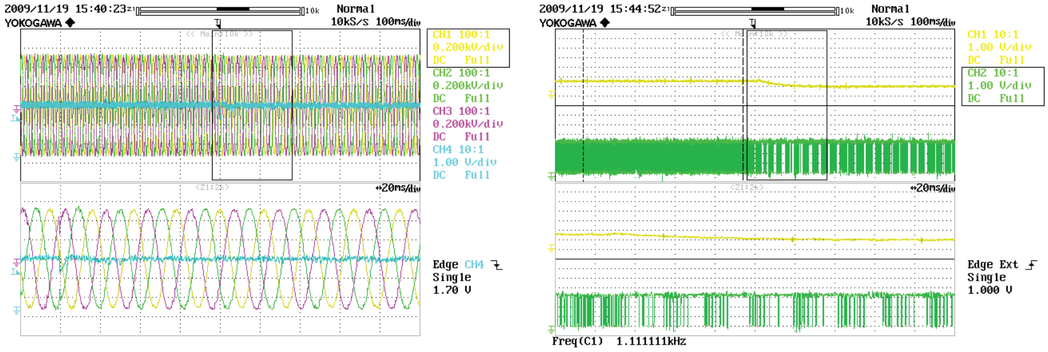

(a) three-phase stator voltages, v_s, and switching function, s.

(b) switching control policy, v_F, and equivalent control, u_{eq}

Figure 7.45: Experimental results, CSMC: Load change from half load to full load.

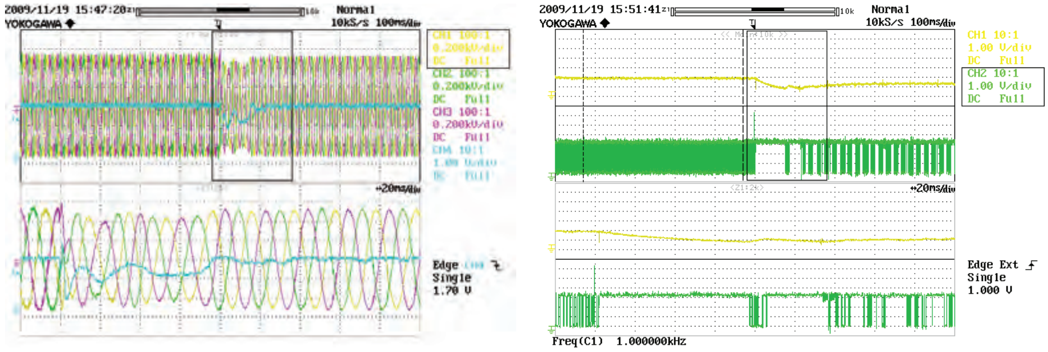

(a) three-phase stator voltages, v_s, and switching function, s.

(b) switching control policy, v_F, and equivalent control, u_{eq}

Figure 7.46: Experimental results, CSMC: Load change from no load to IM connection.

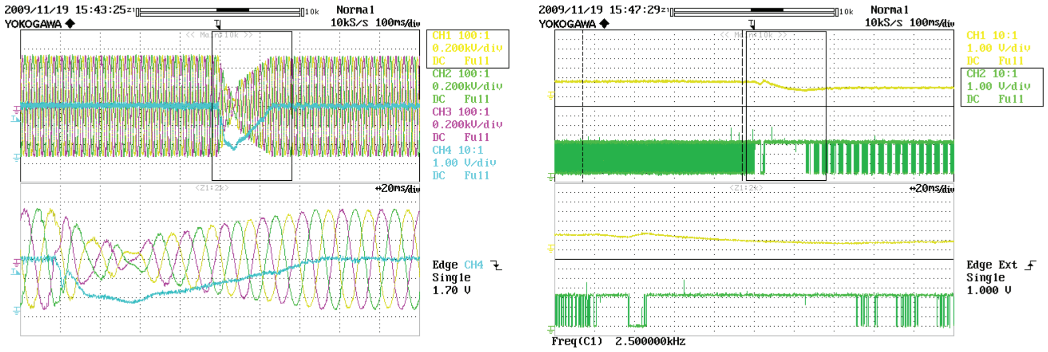

(a) three-phase stator voltages, v_s, and switching function, s. (b) switching control policy, v_F, and equivalent control, u_{eq}

Figure 7.47: Experimental results, CSMC: Load change from half load to half load and IM connection.

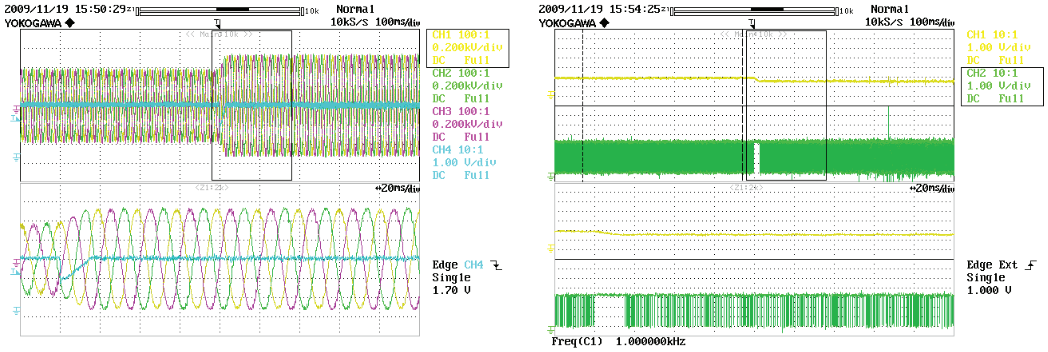

(a) three-phase stator voltages, v_s, and switching function, s. (b) switching control policy, v_F, and equivalent control, u_{eq}

Figure 7.48: Experimental results, CSMC: Voltage reference change from 250Vrms to 380Vrms with half load.

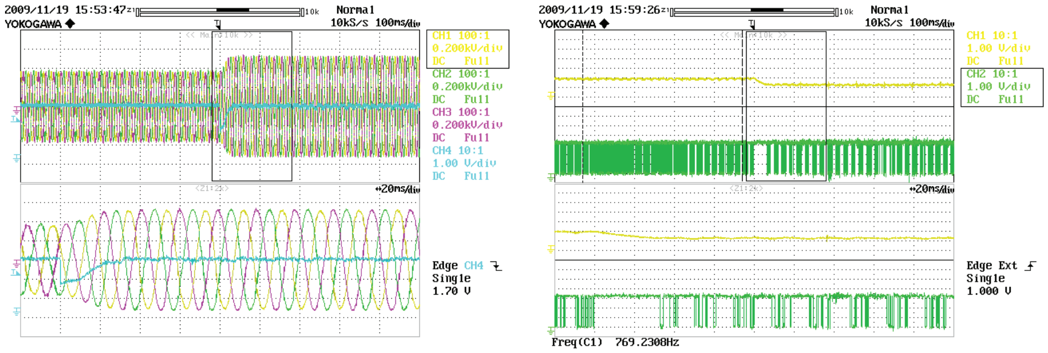

(a) three-phase stator voltages, v_s, and switching function, s. (b) switching control policy, v_F, and equivalent control, u_{eq}

Figure 7.49: Experimental results, CSMC: Voltage reference change from 250Vrms to 380Vrms with inductive load.

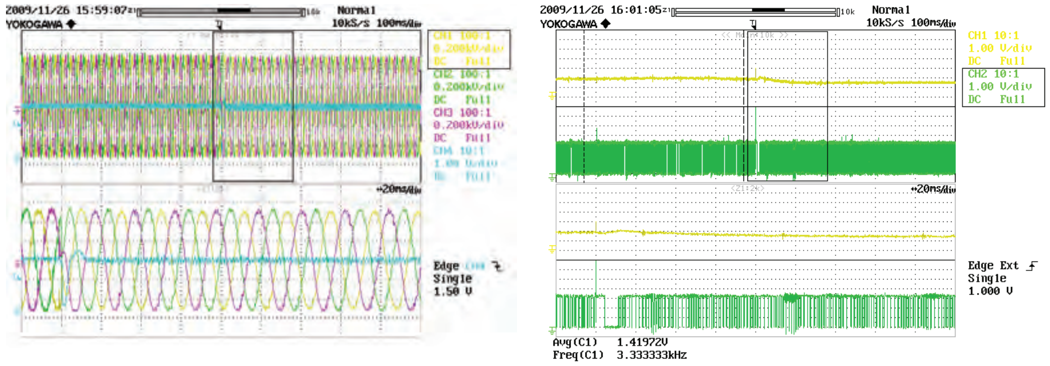

(a) three-phase stator voltages, v_s, and switching function, s.

(b) switching control policy, v_F, and equivalent control, u_{eq}

Figure 7.50: Experimental results, NSMC: Load change from no load to half load.

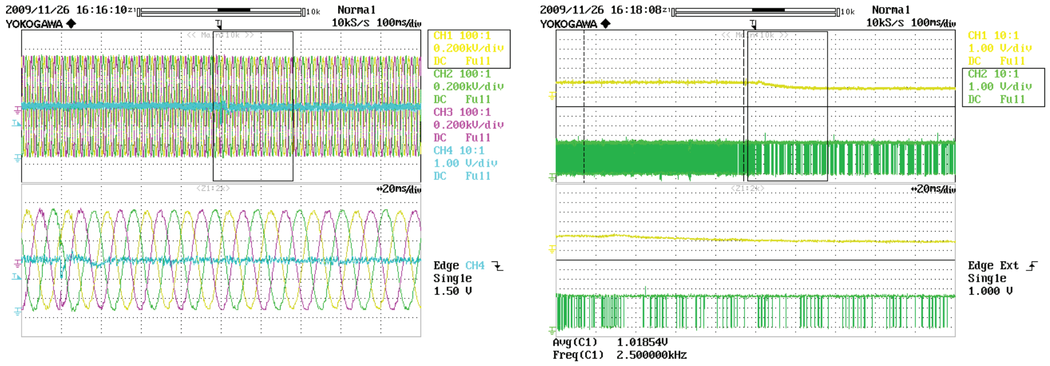

(a) three-phase stator voltages, v_s, and switching function, s.

(b) switching control policy, v_F, and equivalent control, u_{eq}

Figure 7.51: Experimental results, NSMC: Load change from half load to full load.

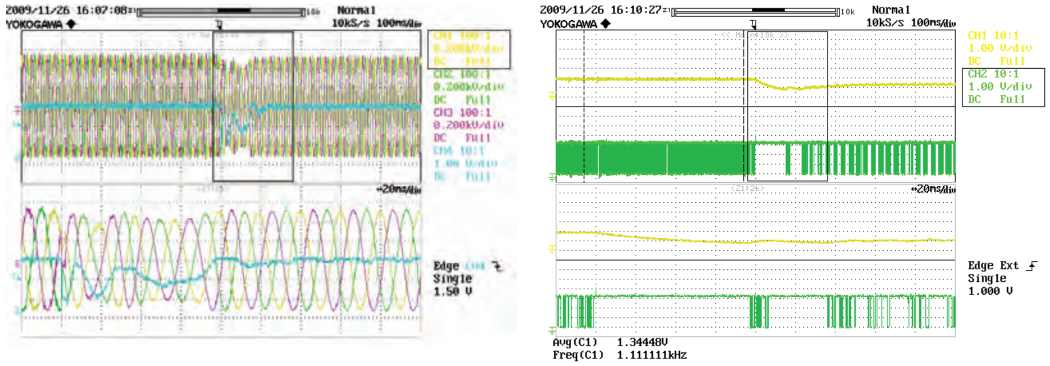

(a) three-phase stator voltages, v_s, and switching function, s.

(b) switching control policy, v_F, and equivalent control, u_{eq}

Figure 7.52: Experimental results, NSMC: Load change from no load to IM connection.

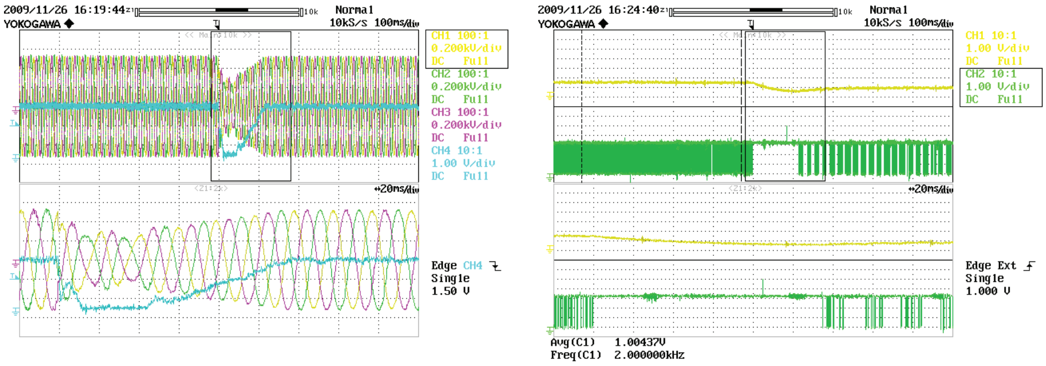

(a) three-phase stator voltages, v_s, and switching function, s.

(b) switching control policy, v_F, and equivalent control, u_{eq}

Figure 7.53: Experimental results, NSMC: Load change from half load to half load and IM connection.

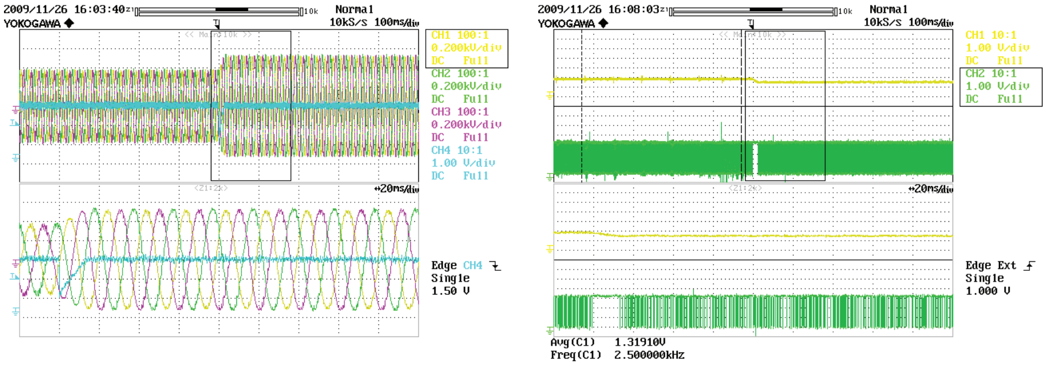

(a) three-phase stator voltages, v_s, and switching function, s.

(b) switching control policy, v_F, and equivalent control, u_{eq}

Figure 7.54: Experimental results, NSMC: Voltage reference change from 250Vrms to 380Vrms with half load.

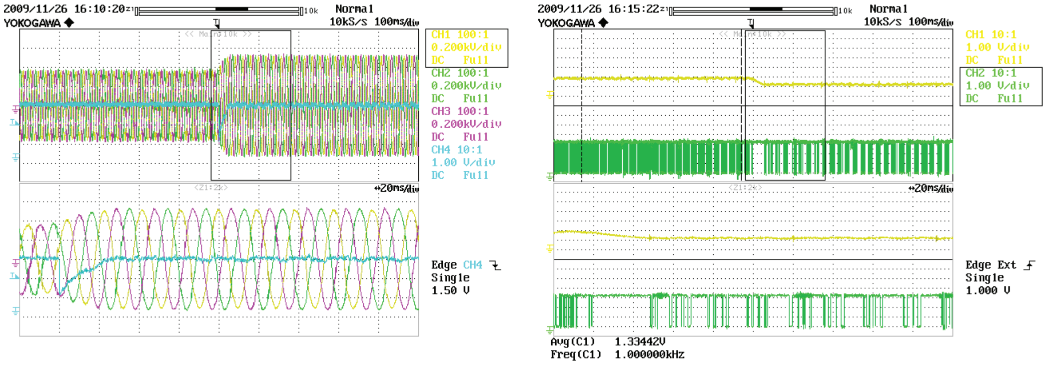

(a) three-phase stator voltages, v_s, and switching function, s.

(b) switching control policy, v_F, and equivalent control, u_{eq}

Figure 7.55: Experimental results, NSMC: Voltage reference change from 250Vrms to 380Vrms with inductive load.

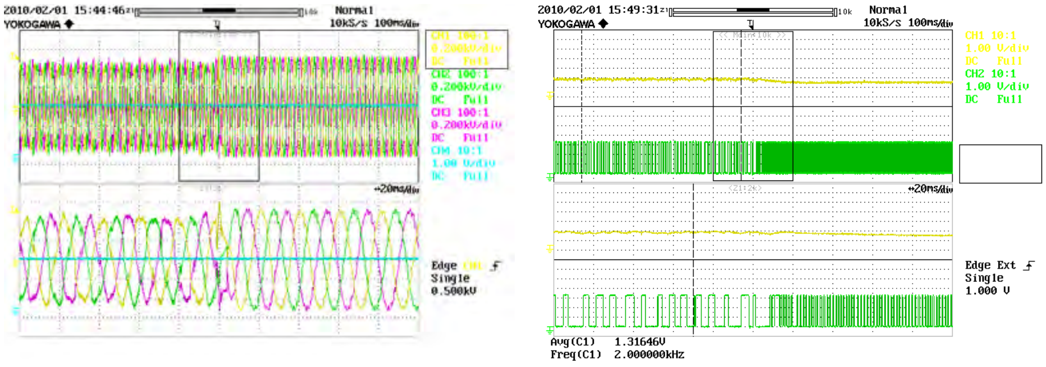

(a) three-phase stator voltages, v_s, and switching function, s.

(b) switching control policy, v_F, and equivalent control, u_{eq}

Figure 7.56: Experimental results, DSMC: Load change from no load to half load.

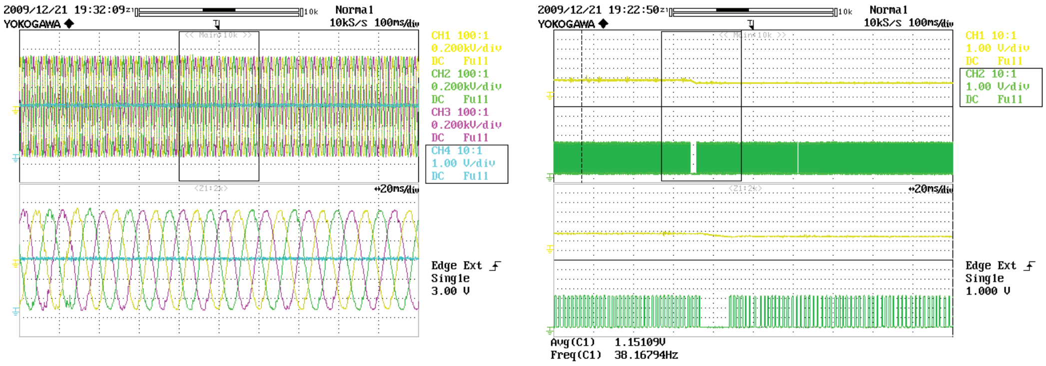

(a) three-phase stator voltages, v_s, and switching function, s.

(b) switching control policy, v_F, and equivalent control, u_{eq}

Figure 7.57: Experimental results, DSMC: Load change from half load to full load.

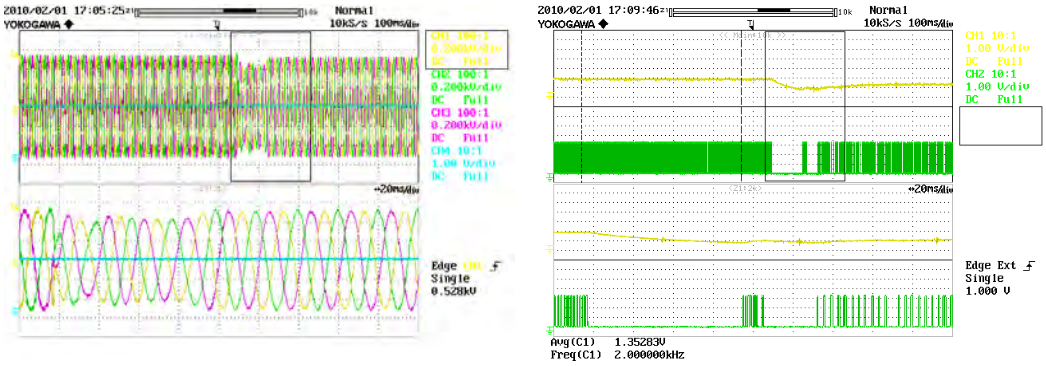

(a) three-phase stator voltages, v_s, and switching function, s.

(b) switching control policy, v_F, and equivalent control, u_{eq}

Figure 7.58: Experimental results, DSMC: Load change from no load to IM connection.

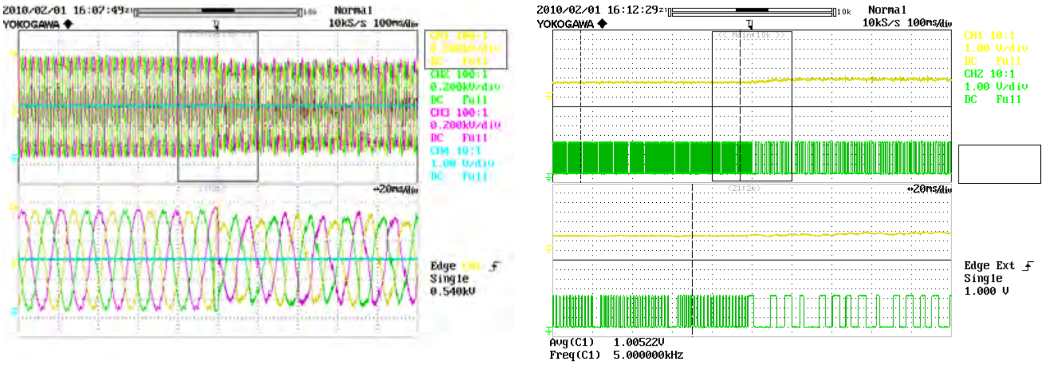

(a) three-phase stator voltages, v_s, and switching function, s.

(b) switching control policy, v_F, and equivalent control, u_{eq}

Figure 7.59: Experimental results, DSMC: Load change from half load to half load and IM connection.

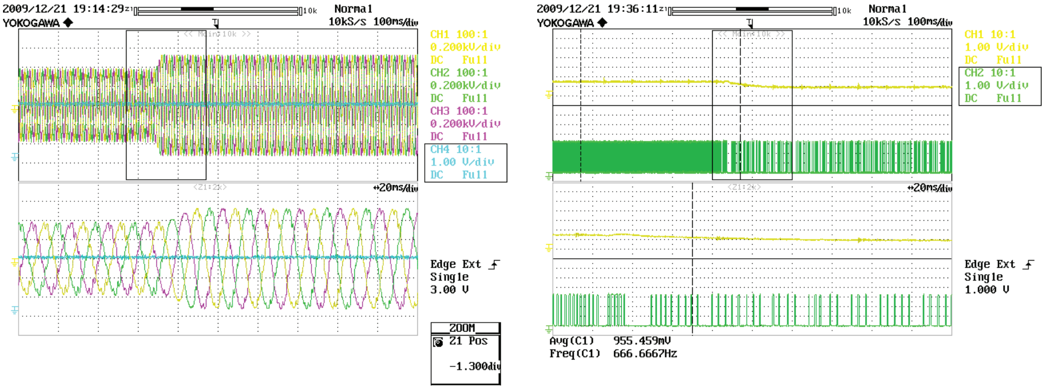

(a) three-phase stator voltages, v_s, and switching function, s.

(b) switching control policy, v_F, and equivalent control, u_{eq}

Figure 7.60: Experimental results, DSMC: Voltage reference change from 250Vrms to 380Vrms with half load.

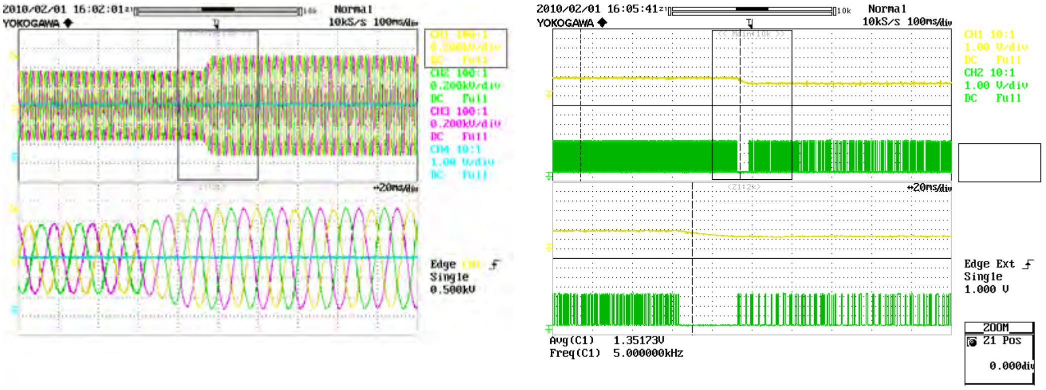

(a) three-phase stator voltages, v_s, and switching function, s.

(b) switching control policy, v_F, and equivalent control, u_{eq}

Figure 7.61: Experimental results, DSMC: Voltage reference change from 250Vrms to 380Vrms with inductive load.

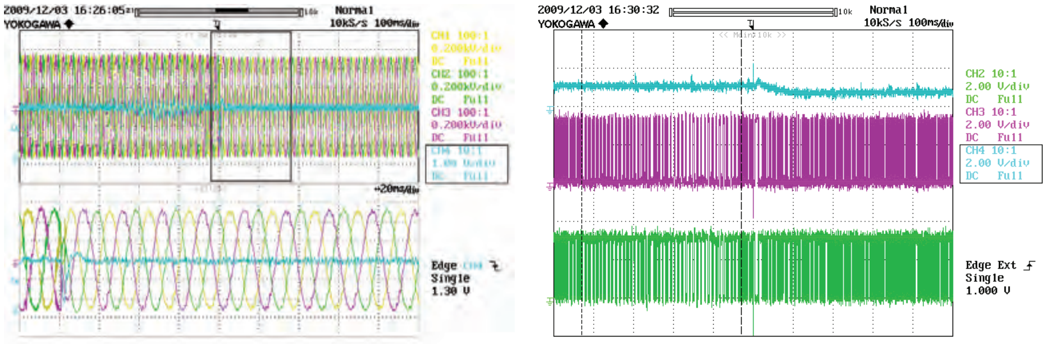

(a) three-phase stator voltages, v_s, and switching function, s.

(b) switching control policy, v_F, equivalent control, u_{eq}, and, fictitious control action, u

Figure 7.62: Experimental results, ESMC: Load change from no load to half load.

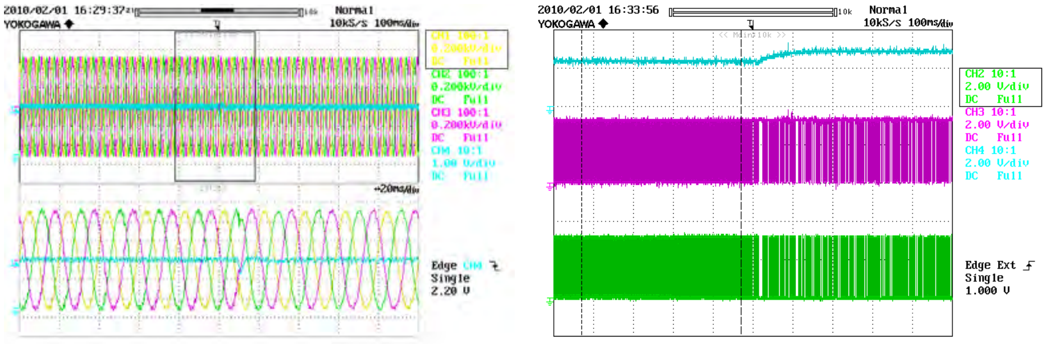

(a) three-phase stator voltages, v_s, and switching function, s.

(b) switching control policy, v_F, equivalent control, u_{eq}, and, fictitious control action, u

Figure 7.63: Experimental results, ESMC: Load change from half load to full load.

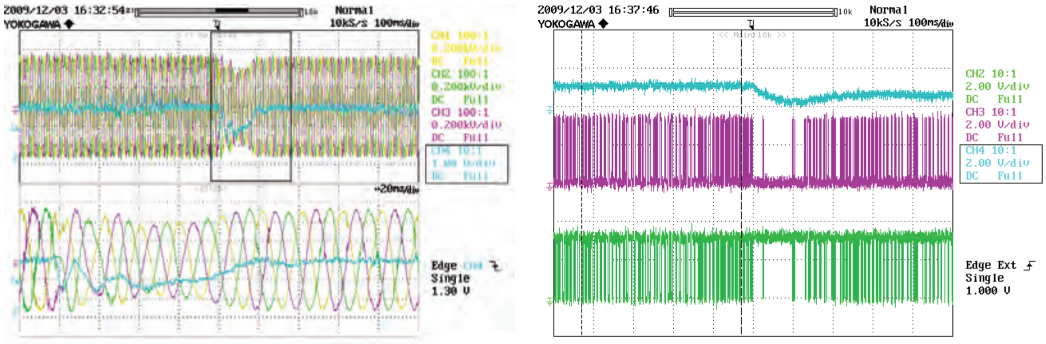

(a) three-phase stator voltages, v_s, and switching function, s.

(b) switching control policy, v_F, equivalent control, u_{eq}, and, fictitious control action, u

Figure 7.64: Experimental results, ESMC: Load change from no load to IM connection.

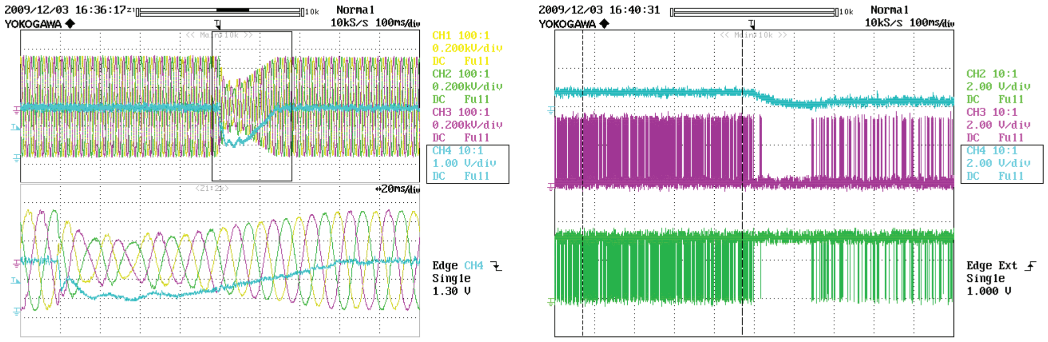

(a) three-phase stator voltages, v_s, and switching function, s.

(b) switching control policy, v_F, equivalent control, u_{eq}, and, fictitious control action, u

Figure 7.65: Experimental results, ESMC: Load change from half load to half load and IM connection.

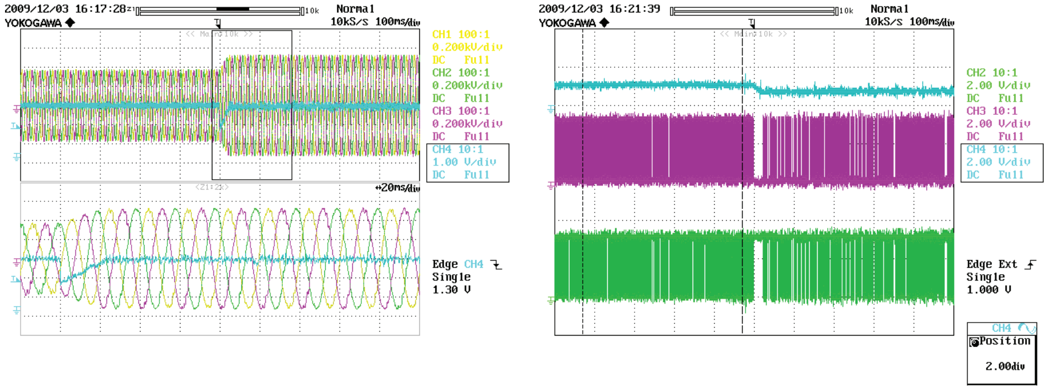

(a) three-phase stator voltages, v_s, and switching function, s.

(b) switching control policy, v_F, equivalent control, u_{eq}, and, fictitious control action, u

Figure 7.66: Experimental results, ESMC: Voltage reference change from 250Vrms to 380Vrms with half load.

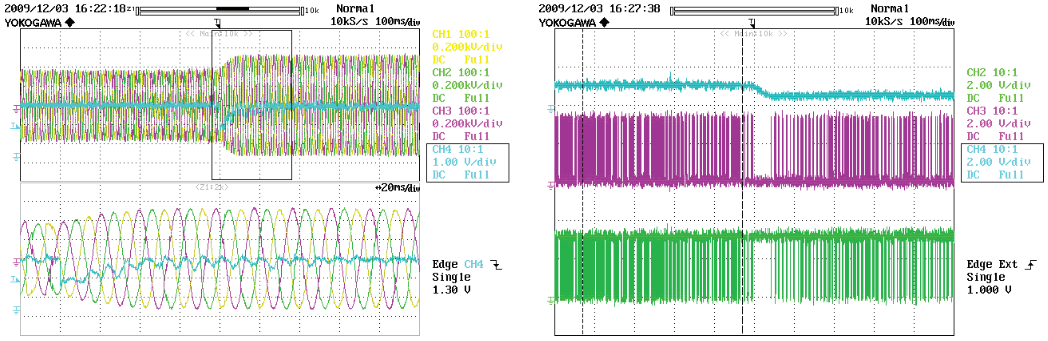

(a) three-phase stator voltages, v_s, and switching function, s.

(b) switching control policy, v_F, equivalent control, u_{eq}, and, fictitious control action, u

Figure 7.67: Experimental results, ESMC: Voltage reference change from 250Vrms to 380Vrms with inductive load.

Chapter 8

Conclusions and future work

8.1 Conclusions

In this dissertation the WRSG has been analyzed in the stand-alone case where neither frequency nor stator voltage amplitude are fixed externally. Since the mechanical speed is normally regulated by an external prime-mover, and the electrical time constant is so fast compared with the mechanical time constants, the mechanical speed was considered externally regulated and the research was focused on the stator voltage amplitude regulation. Usually, in the literature the main research results are pointed on the grid connected generation which simplifies the problem from the machine side because its dynamical equations are reduced. The dynamical equations of the stand-alone wound rotor synchronous machine in dq-coordinates feeding both a resistive and an inductive load were obtained. As well as linear approximated models and their transfer functions.

Four different controllers based on sliding mode control techniques were designed in the dq reference frame. The obtained control laws regulate the stator voltage amplitude irrespectively of the load value. Furthermore, only voltage and rotor position measures (to compute the dq transformation), were required. The first three controllers were designed for resistive loads, and the fourth for an inductive load. However, simulation and experimental results of each controller were done with both kind of loads.

The error of the square voltage amplitude ($V_{ref}^2 - V_s^2$) against the voltage amplitude difference discussed along the text shows the advantage of avoid the root computation at the voltage calculus which is a hard task for digital control implementations and uses a lot of hardware resources. This selection introduces the use of the d-voltage component sign in the control switching policy, which allows to stabilize the system in the two possible equilibrium points. This, cannot be achieved with a simple PI controller where one of the two equilibrium points becomes unstable. When a quadratic function is used as a switching function, an undesirable sliding motion may arise. This phenomenon occurs when the cylinder is selected as switching surface, then sliding modes in the plane $i_d = 0$ can be found. A simpler alternative consists in a nested control with an inner SMC loop regulating the d-component of the stator voltage and a PI outer loop regulating its reference.

The problem of a zero relative degree output when dynamical loads are used was overcome introducing a dynamic extension of the system. This implies a fictitious control action which is integrated to obtain the real field voltage to be applied to the generator.

The stability of the closed-loop system were proved at least using a small-signal analysis. In some cases a local asymptotic stability was discussed. The closed loop dynamics of the CSMC were described. It results in a complex dynamics which introduces sliding modes on a surface not considered in the control design. Assuming higher enough V_{DC}, system trajectories may slide on two surfaces (the cylinder defined by the desired output and a plane where transversality condition fails). Poincaré-Bendixon and Bendixon theorems allow to prove that the ideal sliding dynamics on the cylinder consists in two locally asymptotically stable equilibrium points. The ISD on the plane is linear with a virtual equilibrium point inside of the cylinder. A generic trajectory can slide on the cylinder and reach one of the equilibrium points or alternatively slide on the cylinder and the plane till it achieves the basin of attraction of one of the two equilibrium points.

The case of saturated values of V_{DC} in the CSMC was also studied. This realistic case reveals that the complete cylinder is not an sliding surface and the sliding condition holds in some narrow strips only. However, these strips are wide enough to guarantee local asymptotic stability of the equilibrium points as has been shown by numeric simulations.

Simulation and experimental validation of each controller was carried out. The obtained results validate the designs and show the main advantages and disadvantages of each one. The designed control schemes implementation are quite simple, and some of them do not require any gain tunning. Experimental tests disadvise the so-called DSMC for a real application. It does not works properly in some cases where the three-phase stator voltages are distorted which is not desirable or definitively cannot regulate the stator voltage amplitude. The main lack of this approach is the absence of a proportional gain on the output error which implies a *soft* performance of the controller and makes the switching function remain close to zero. It can be also noticed that, the DSMC can be seen as a particular case of NSMC, by taking the error of the square ($V_{ref}^2 - V_s^2$) and setting $k_p = 0$ in the PI loop.

The CSMC and NSMC behavior are very similar. The main difference is presented in the switching function which in the NSMC oscillates more than in the CSMC. The main advantage of the CSMC is that it does not need any tuning. The ESMC regulates the stator voltage amplitude but it is slow compared with the other controllers, it also results in a bit distorted waves when the generator is without load.

8.2 Future works

Though three of the proposed controllers reveal a good behavior under resistive and inductive loads and this kind of load is present in some applications, it is true that actual loads are mostly nonlinear. Then, a future research line is a deep analysis for nonlinear loads. Actually, the harmonics cannot be controlled by the machine due to its limited bandwidth (see Figure 3.1), but its behavior under this kind of loads must be analyzed.

In three-phase systems, another trend is the study of unbalanced loads and faulty conditions. The main problem in this situations is the voltage measurement, because it is formed by positive, negative and homopolar terms. A reasonable solution is to split the voltage in this terms and only control the positive sequence voltage [65], [66], [67]. Methods for avoiding the chattering phenomena must be included in future controller designs.

The experimental and simulation results were obtained with a switching frequency up to 10 kHz, which in high power systems is not allowed. The restriction to low switching frequency, for example 1 kHz, in the controller implementation can be an interesting research line.

The stability of the designed controllers were proved at least using small-signal. In this case, a deeper closed loop analysis should be done in order to find the basin of attraction of each equilibrium point. The CSMC analysis was done deeper in relation to each controller, but some results have been found numerically, at the future, analytical results must be found.

Stand alone WRSG are not only present in the stand-alone generation emulating the power grid for emergency and security reasons. They can be found in other applications related to recent trends in electric vehicles and renewable energies.

To motivate the use of the presented controllers, two possible applications are presented: a particular topology for a Hybrid Electric Vehicle and a variable speed Wind Turbine configuration. In both systems the WRSG is not directly connected to the grid, and its goal can be the stator voltage regulation. Furthermore, in general, for these applications, the electrical time constant is sufficiently small compared with the mechanical one, and a fixed mechanical speed can be still assumed.

8.2.1 Hybrid Electric Vehicles

Hybrid electrical vehicles (HEV) are the focus of many research interests because they provide good performance and long operating time [20]. Basically, the HEV is composed of an internal combustion engine, an electrical machine and a battery pack. The main goal of the HEV is to reduce the CO_2 emissions by means of the regenerative braking, using the electrical machine both as a motor drive or as a generator, which charges or discharges the batteries. It is also desired to keep the drivability performance of the vehicle [49].

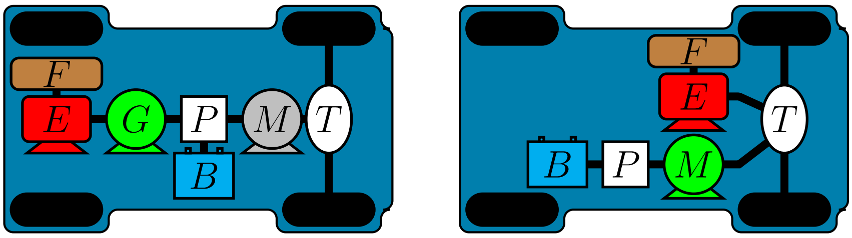

(a) series hybrid (b) parallel hybrid

Figure 8.1: HEV topologies.

Figure 8.1 shows some HEV topologies. B represents the battery, E the internal combustion engine (ICE), F the fuel tank, G the electrical generator, M the electrical motor, P the power converter and T the vehicle transmission.

Depending on the interconnection between the different parts of the HEV, this classification can be summarized in two basic configurations:

- **Series Hybrid Electric Vehicle (SHEV):** In a SHEV the ICE mechanical output drives an electric machine, which generates electrical energy. This energy supplies another electric machine, which acts as a motor coupled to the transmission line [8]. The main advantages of this configuration are: on the one hand, the ICE can work at an optimal configuration point finding a compromise between fuel economy and exhaust emissions reduction and, on the other hand, the gear shifting is not necessary. The SHEV is suitable for city cars [21][1][24].

- **Parallel Hybrid Electric Vehicle (PHEV):** The mechanical power is provided simultaneously by the ICE and the electric motor. In this way the ICE can be used for driving while the electric motor for acceleration [8]. There are less energy conversion stages compared to the SHEV, and therefore, the system is more efficient than SHEV, which is the main advantage[21].

An especial case of SHEV called DiSAC (Direct Synchronous-Asynchronous Conversion) system, where the stators of the electrical generator and the electrical motor are directly connected is shown in Figure 8.2. In this scheme the generator is a WRSG which fixes the stator voltage amplitude to a Doubly-Fed Induction Machine (DFIM) that acts as a motor. Notice that the DFIM acts either in generator or motor mode. Both machines (WRSG and DFIM) are rotor connected to the batteries by means of DC/DC and AC/DC converters, respectively [52].

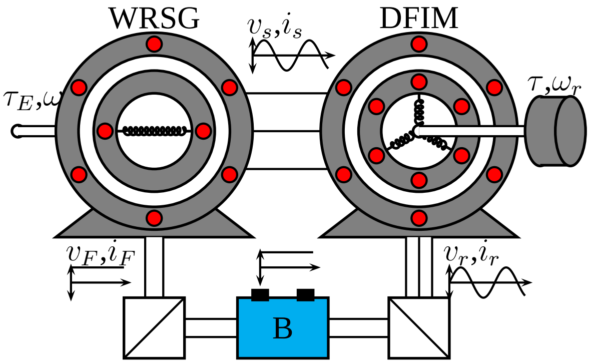

Figure 8.2: Electrical scheme of the DiSAC scheme.

This scheme defines four control inputs: the field (or rotor) voltage of the WRSG, v_F, the two rotor dq-voltage components of the DFIM, $v_r \in \mathbb{R}^2$, and the mechanical torque produced by the ICE, τ_W. These four control variables are able to control the electrical torque produced by the DFIM, to manage the power flow and to keep a stator voltage to its nominal value together with a stator power factor close to one.

The presented controllers for the WRSG are suitable for this application, because the DFIM can be seen as an inductive load. Specially, the ESMC guarantees the stability for a large range of inductive loads. However, when the control implementation in the DiSAC system, the effect of the varying speed must be studied.

8.2.2 Wind Turbines

Wind turbine (WT) production has grown in size from some kW to the multi MW power range in last three decades. Since 1990's some manufacturers have replaced in the wind turbine design the asynchronous generator by the synchronous one, while others have introduced the doubly-fed induction machine (DFIM). In this development the pitch control concept, advanced power electronics equipment and control under variable speed have been introduced [28].

Multi MW wind turbines rotates at 10-15 rpm. Hence, a gear-box and a standard fixed speed generator or a multi-pole generator are the possible solutions [37]. A technological roadmap of possible technical solutions for wind turbines is depicted in Figure 8.3.

Taking into account this roadmap, the most common turbine designs can be summarized in four wind turbine schemes:

- **Fixed speed wind turbines:** This scheme is based on a squirrel cage induction machine which is directly connected to the grid. Then, it needs a capacitor bank for reactive power compensation [37], [6]. This scheme is manufactured by NEG Micon, Bonus and Nordex [28].
- **Partial variable speed wind turbine with variable rotor resistance:** This configuration manufactured by Vestas and known as OptiSlip uses a DFIM connected directly to the grid. External resistors are connected to the rotor to control the slip an the power output [37].
- **Variable speed WT with partial-scale frequency converter:** This concept, corresponds to a variable speed DFIM which stator is directly connected to the grid,

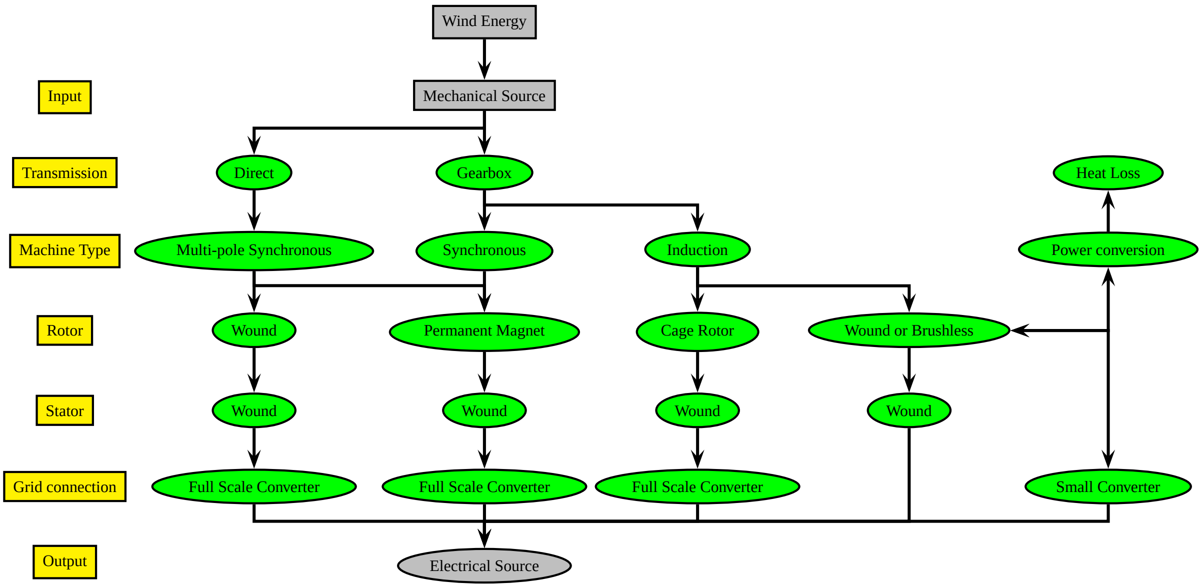

Figure 8.3: Technological roadmap for wind turbine's technology [28]

while a partial-scale power converter (approx. 30% of nominal power) controls the rotor frequency and mechanical speed [37]. The motivation of this concept is a variable speed in a wide range compared with OptiSlip and less expensive compared with full power converter. It is manufactured by Vestas, Gamesa, Enron Wind, Nordex and Dewind [28].

- **Variable speed WT with full-scale power converter:** It corresponds to a full variable speed controlled WT, the generator is connected to the grid trough a full-scale frequency converter. Then, additional technical performances of the WT can be achieved. The generator can be a DFIM, a PMSM or a WRSG. Some schemes are gearless using a multi-pole machine. Examples of manufacturers are Siemens Wind Power, Made, Lagerway and Enercon. In particular Lagerway and Enercon uses a WRSG [37], [28].

As pointed out above, the WRSG can play and important role for variable speed WT with power converter connected to the stator side, see Figure 8.4. In this configuration the WRSG is "isolated" from the grid by the power converter. Consequently, the presented control algorithms can help to regulate the stator voltage amplitude and keep the system in the desired operation point.

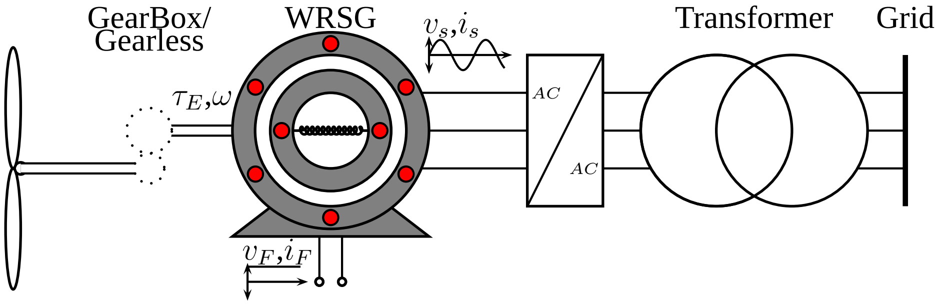

Figure 8.4: Variable speed WT with full-scale power converter using a WRSG.

Bibliography

[1] M. Al-Atabi and T. Yusaf. Experimental investigation of a single cylinder diesel engine as a hybrid power unit for a series hybrid electric vehicle. In *Proc. of the IEEE Student Conference on Research and Development*, pages 261–264, 2002. 139

[2] P.M. Anderson and A.A. Fouad. *Power System Control and Stability*. The Iowa State University Press, 1977. 1

[3] E.C. Anene, U.O. Aliyu, J. Lévine, and G. K. Venayagamoorthy. Flatness-based feedback linearization of a synchronous machine model with static excitation and fast turbine valving. In *Proc. of the IEEE Power System Society General Meeting*. 2

[4] C. Batlle, A. Dòria-Cerezo, and G. Espinosa. Simultaneous ida-passivity-based control of a wound rotor synchronous motor. In *Proc. of the IEEE Conference on Decision and Control*, 2008. 1

[5] D. Biel and E. Fossas. *SMC application in power electronics*, volume 66, pages 265–284. IEE Control Series, London, 2004. 2

[6] F. Blaajberg, R. Teodorescu, M. Liserre, and A. Timbus. Overview of control and grid synchronization for distributed power generation systems. *IEEE Trans. on Industrial Electronics*, 53(3):1398–1409, 2006. 140

[7] J. Cabrera-Vázquez, A. G. Loukianov, J. M. Cañedo, and V. I. Utkin. Robust controller for synchronous generator with local load via vsc. *Electrical Power and Energy Systems*, 29:348–359, 2007. 1, 3

[8] C. Chan. The state of the art of electric and hybrid electric vehicles. In *Proc. of the IEEE*, volume 90, 2002. 139

[9] J. Chiasson. *Modeling and High Performance Control of Electric Machines*. John Wiley & Sons Inc., 2005. 1

[10] J. Dai, D. Xu, and B. Wu. A novel control scheme for current-source-converter-based pmsg wind energy conversion systems. *IEEE Trans. on Power Electronics*, 24(4):963–972, 2009. 2

[11] R.A. DeCarlo, S.H. Zak, and G.P. Matthews. Variable structure control of nonlinear multivariable systems: A tutorial. *Proc. of the IEEE*, 76(3):212–232, 1988. 4, 5

[12] M. Dehghani. Linear h_∞ control of a synchronous generator. In *Proc. of the IEEE Electrical Power & Energy Conference*, 2008. 2

[13] A. Dòria-Cerezo, E. Fossas, and R.S. Muñoz-Aguilar. Analysis of the closed loop dynamics of a sliding mode controlled stand alone synchronous generator. *Submitted to Conference on Decision and Control, 2010.* 9

[14] A. Dòria-Cerezo, E. Fossas, and R.S. Muñoz-Aguilar. Stability analysis of the closed loop dynamics of a sliding mode controlled stand-alone wound rotor synchronous generator. *Submitted to International Journal of Control.* 9

[15] A. Dòria-Cerezo, E. Fossas, R.S. Muñoz-Aguilar, and V.I. Utkin. Sliding mode control of an isolated wound rotor synchronous generator. In *Proc. of the European Control Conference*, 2009. 9

[16] A. Dòria-Cerezo, V.I. Utkin, R.S. Muñoz-Aguilar, and E. Fossas. Control of a stand-alone wound rotor synchronous generator: sliding mode control via regulation the d-voltage component. *Submitted to IEEE Trans. on Control Systems Technology*. 9, 10

[17] A. Dòria-Cerezo, V.I. Utkin, R.S. Muñoz-Aguilar, and E. Fossas. Two sliding mode control approaches of the stator voltage amplitude regulation of a stand-alone wrsm. In *Proc. of the International Workshop on Variable Structure Systems*, 2010. 9

[18] J. Driesen and K. Visscher. Virtual synchronous generators. In *Proc. of the Power and Energy Society General Meeting - Conversion and Delivery of Electrical Energy in the 21st Century*, 2008. 1

[19] C. Edwards and S. Spurgeon. *Sliding Mode Control: Theory and Applications*. Taylor and Francis, 1998. 4

[20] M. Ehsani, Y. Gao, S.E. Gay, and A. Emadi. *Modern Electric, Hybrid Electric, and Fuel Cell Vehicles: Fundamentals, Theory, and Design*. CRC, Boca Raton, FL, 2004. 138

[21] A. Emadi, K. Rajashekara, S. Williamson, and S. Lukic. Topological overview of hybrid electric and fuel cell vehicular power system architectures and configurations. *IEEE Trans. on Vehicular Technology*, 54(3):763–770, May 2005. 139

[22] M. Fernandes, A. D. Lima, , and A. D. Araújo. Variable structure model reference adaptive controller applied to a synchronous generator control. In *Proc. of the Mediterranean Conference on Control and Automation*, 2008. 2

[23] A. Girardin and G. Friedrich. Optimal control for a wound rotor synchronous starter generator. In *Proc. of the IAS Annual Meeting. Industry Applications Conference*, 2006. 2

[24] M. Gokasan, S. Bogosyan, and D. Goering. Sliding mode based powertrain control for efficiency improvement in series hybrid-electric vehicles. *IEEE Trans. on Power Electronics*, 21:779–790, May 2006. 139

[25] M. Gokasan, S. Bogosyan, and D.J. Goering. Sliding mode based powertrain control for efficiency improvement in series hybrid-electric vehicles. *IEEE Trans. on Power Electronics*, 21(3):779–790, 2006. 2

[26] J. Gong, R. Xie, W. Liu, and S. Xie. H_∞ controller design of the synchronous generator. In *Proc. of the International Conference on Intelligent Computation Technology and Automation.*, 2008. 2

[27] S. Grabic, N. Celanovic, and V. A. Katic. Permanent magnet synchronous generator cascade for wind turbine application. *IEEE Trans. on Power Electronics*, 23(3):1136–1142, 2008. 2

[28] L.H. Hansen, L. Helle, F. Blaabjerg, E. Ritchie, S. Munk-Nielsen, H. Bindner, P. Sorensen, and B. Bak-Jensen. Conceptual survey of generators and power electronics for wind turbines. Technical report, Riso National Laboratory, 2001. XV, 140, 141

[29] B. He and M. Yang. Robust lpv control of diesel auxiliary power unit for series hybrid electric vehicles. *IEEE Trans. on Power Electronics*, 21(3):791–798, 2006. 2

[30] R. Hesse, D. Turschner, and H.-P. Beck. Micro grid stabilization using the virtual synchronous machine. In *Proc. of the International Conference on Renewable Energies and Power Quality*, 2009. 1

[31] E. Ho and P.C. Sen. High-performance decoupling control techniques for various rotating field machines. *IEEE Trans. on Industrial Electronics*, 42(1):40–49, 1995. 1

[32] H. Huerta, A. G. Loukianov, and J. Manuel Cañedo. Multimachine power-system control: Integral-sm approach. *IEEE Trans. on Industrial Electronics*, 56(6):2229–2236, 2009. 3

[33] J. Y. Hung, W. Gao, and J. C. Hung. Variable structure control: A survey. *IEEE Trans. on Industrial Electronics*, 40(1):2–22, 1993. 2

[34] L. Idkhajine, E. Monmasson, M-W. Naouar, A. Prata, and K. Bouallaga. Fully integrated fpga-based controller for synchronous motor drive. *IEEE Trans. on Industrial Electronics*, 56(10):4006–4017, 2009. 1, 2

[35] IEEE. Ieee guide: Test procedures for synchronous machines. std.115-1995. Technical report, IEEE, 1995. 87

[36] Texas Instruments. Sprs439c-tms320f28335, tms320f28334, tms320f28332 tms320f28235, tms320f28234, tms320f28232 digital signal controllers (dscs) data manual. 89

[37] F. Iov, M. Ciobotaru, D. Sera, R. Teodorescu, and F. Blaabjerg. Power electronics and control of renewable energy systems. In *Proc. of the Power Electronics and Drive Systems*, 2007. 140, 141

[38] I. Jadrić, D. Borojević, and M. Jadrić. Modeling and control of a synchronous generator with an active dc load. *IEEE Trans. on Power Electronics*, 15(2):303–311, 2000. 2

[39] P.C. Krause, F. Nozari, T.L. Skvarenina, and D.W. Olive. The theory of neglecting stator transients. *IEEE Trans. on Power Apparatus and Systems*, pages 141–148, 1979. 1

[40] P.C. Krause, O. Wasynczuk, and S.D. Sudhoff. *Analysis of Electric Machinery and Drive Systems*. John Wiley & Sons Inc., 2002. 11, 13, 14

[41] Y.-S. Kung, C.-C. Huang, and M.-H. Tsai. Fpga realization of an adaptive fuzzy controller for pmlsm drive. *IEEE Trans. on Industrial Electronics*, 56(8):2923–2932, 2009. 2

[42] Y.-S. Kung and M.-H. Tsai. Fpga-based speed control ic for pmsm drive with adaptive fuzzy control. *IEEE Trans. on Power Electronics*, 22(6):2476–2486, 2007. 1

[43] C.-K. Lai and K.-K. Shyu. A novel motor drive design for incremental motion system via sliding-mode control method. *IEEE Trans. on Industrial Electronics*, 52(2):499–507, 2005. 2, 3

[44] K. T. Law, D.J. Hill, and N.R. Godfrey. Robust controller structure for coordinated power system voltage regulator and stabilizer design. *IEEE Trans. on Control Systems Technology*, 2(3):220–232, 1994. 2

[45] W. Leonhard. *Control of electric drives*. Springer, 1995. 1

[46] A. G. Loukianov, J. M. Cañedo, V.I. Utkin, and J. Cabrera-Vázquez. Discontinuous controller for power systems: Sliding-mode block control approach. *IEEE Trans. on Industrial Electronics*, 51(2):340–353, 2004. 3

[47] Control Techniques Drives Ltd. 4q2 user guide: 0.55 - 7.5kw d.c.motor regenerative speed controller, 2007. 86

[48] A.E. Magri, F. Giri, A. Abouloifa, and M. Haloua. Nonlinear control of wound-rotor synchronous-motor. In *Proc. of the IEEE International Conference Control Applications*, pages 3110–3115, 2006. 2

[49] J.M. Miller. *Propulsion systems for hybrid vehicles*. IEE, Power and Energy series, 2004. 138

[50] E. Mouni, O. Bachelier, S. Tnani, and G. Champenois. H_∞ feedback control of synchronous generator output voltage: Solution by riccati equations. In *Proc. of the International Conference on Computer as a Tool*, 2007. 2

[51] E. Mouni, S. Tnani, and G. Champenois. Synchronous generator output voltage real-time feedback control via h_∞ strategy. *IEEE Trans. on Energy Conversion*, 24(2), 2009. 2

[52] R. S. Muñoz-Aguilar, A. Dòria-Cerezo, and P. F. Puleston. Energy-based modelling and simulation of a series hybrid electric vehicle propulsion system. In *Proc. of the European Control Conference*, 2009. 139

[53] R.S. Muñoz-Aguilar, A. Dòria-Cerezo, and E. Fossas. Stator voltage regulation of a stand-alone wound-rotor synchronous generator using sliding mode control techniques. *Submitted to IEEE Trans. on Power Electronics*. 9, 10

[54] R.S. Muñoz-Aguilar, A. Dòria-Cerezo, and E. Fossas. A sliding mode control for a wound rotor synchronous generator with an isolated rl load. In *Proc. of the American Control Conference*, 2010. 9

[55] R.S. Muñoz-Aguilar, A. Dòria-Cerezo, E. Fossas, and R. Cardoner. Sliding mode control for a stand alone wound rotor synchronous generator. *Submitted to IEEE Trans. on Industrial Electronics*. 9, 10

[56] M. Naouar, A. Naassani, E. Monmasson, and I. Slama-Belkhodja. Fpga-based predictive current controller for synchronous machine speed drive. *IEEE Trans. on Power Electronics*, 3(4):2115–2126, 2008. 1

[57] M-W. Naouar, E.Monmasson, and I. Slama-Belkhodja. Fpga-based torque controller of a synchronous machine. In *Proc. of the IEEE International Conference on Industrial Technology*, 2004. 2

[58] M-W. Naouar, A. Naassani, E. Monmasson, and I. Slama-Belkhodja. Fpga-based speed control of synchronous machine using a p-pi controller. In *Proc. of the International Symposium on Industrial Electronics*, 2006. 2

[59] M-W. Naouar, A. Naassani, E. Monmasson, and I. Slama-Belkhodja. Fpga design for direct sliding mode current control of a synchronous machine. In *Proc. of the IEEE Applied Power Electronics Conference and Exposition*, 2009. 2, 3

[60] M-W. Naouara, E. Monmasson, A. Naassani, I. Slama-Belkhodja, and N. Patin. Fpga-based current controllers for ac machine drives-a review. *IEEE Trans. on Industrial Electronics*, 54(4):1907–1925, 2007. 1, 2

[61] K. Ogata. *Modern Control Engineering*. Prentice Hall, 3 edition, 1998. 33

[62] R. Ortega, M. Galaz, A. Astolfi, Y. Sun, and T. Shen. Transient stabilization of multimachine power systems with nontrivial transfer conductances. *IEEE Trans. on Automatic Control*, 50(1):60–75, 2005. 2

[63] N. Patin, L. Vido, E. Monmasson, J.-P. Louis, M. Gabsi, and M. Lécrivain. Control of a hybrid excitation synchronous generator for aircraft applications. *IEEE Trans. on Industrial Electronics*, 55(10):3772–3783, 2008. 2

[64] L. Perko. *Differential Equations and Dynamical Systems*. Springer-Verlag, 2007. 48

[65] P. Rodríguez, J. Pou, J. Bergas, J.I. Candela, R. Burgos, and D. Boroyevich. Decoupled double synchronous reference frame pll for power converters control. *IEEE Trans. on Power Electronics*. 137

[66] P. Rodriguez, A. Luna, M. Ciobotaru, R. Teodorescu, and F. Blaabjerg. Advanced grid synchronization system for power converters under unbalanced and distorted operating conditions. In *Proc. of the IEEE Conference on Industrial Electronics*, 2006. 137

[67] P. Rodriguez, R. Teodorescu, I. Candela, A.V. Timbus, M. Liserre, and F. Blaabjerg. New positive-sequence voltage detector for grid synchronization of power converters under faulty grid conditions. In *Proc. of the Power Electronics Specialists Conference*, 2006. 137

[68] C. Rossi, D. Casadei, A. Pilati, and M. Marano. Wound rotor salient pole synchronous machine drive for electric traction. In *Proc. of the IEEE Industry Applications Conference*, 2006. 2

[69] A. E. Sanchez-Orta, J. De León-Morales, and E. Lopez-Toledo. Discrete-time nonlinear control scheme for small synchronous generator. *Electric Power and Energy Systems*, 24:751–764, 2002. 3

[70] M.K. Senesky, P. Tsao, and S.R. Sanders. Simplified modelling and control of a synchronous machine with variable-speed six-step drive. In *Proc. of the IEEE Applied Power Electronics Conference and Exposition*, 2004. 1

[71] A. Soto-Cota, A. G. Loukianov L. M. Fridman, and J. M. Cañedo. Variable structure control of synchronous generator: Singularly perturbed analysis. In *Proc. of the IEEE Conference on Decision and Control*, 2003. 3

[72] A. Soto-Cota, A. G. Loukianov L. M. Fridman, and J. M. Cañedo. Power system singularly perturbed discontinuos control. In *Proc. of the American Control Conference*, 2004. 3

[73] T. Suksri, S. Srilad, and S. Tunyasrirut. Reactive power and voltage of a synchronous generator control by using t-dof controller. In *Proc. of the SICE Annual Conference*, 2008. 1

[74] L. Tang and G.-J. Su. High-performance control of two three-phase permanent-magnet synchronous machines in an integrated drive for automotive applications. *IEEE Trans. on Power Electronics*, 23(6):3047–3055, 2008. 2

[75] V. Utkin, J. Guldner, and J. Shi. *Sliding Mode Control in Electromechanical Systems*. Taylor and Francis, 1999. 2, 34

[76] V.I. Utkin. Sliding mode control design principles and applications to electric drives. *IEEE Trans. on Industrial Electronics*, 40(1):23–36, 1993. 2

[77] V.I. Utkin. *VSS Premise in XX century: evidences of a witness*, pages 1–32. World Scientific, 2000. 3, 4

[78] Peter Vas. *Vector Control of AC Machines*. Oxford Clarendon Press, 1990. 14

[79] W. Yan, J. Hu, V. Utkin, and L. Xu. Sliding mode pulsewidth modulation. *IEEE Trans. on Power Electronics*, 23(2):619–626, 2008. 2, 3